INFORMATION TO USERS

This manuscript has been reproduced from the microfilm master. UMI films the text directly from the original or copy submitted. Thus, some thesis and dissertation copies are in typewriter face, while others may be from any type of computer printer.

The quality of this reproduction is dependent upon the quality of the copy submitted. Broken or indistinct print, colored or poor quality illustrations and photographs, print bleedthrough, substandard margins, and improper alignment can adversely affect reproduction.

In the unlikely event that the author did not send UMI a complete manuscript and there are missing pages, these will be noted. Also, if unauthorized copyright material had to be removed, a note will indicate the deletion.

Oversize materials (e.g., maps, drawings, charts) are reproduced by sectioning the original, beginning at the upper left-hand corner and continuing from left to right in equal sections with small overlaps.

Photographs included in the original manuscript have been reproduced xerographically in this copy. Higher quality 6" x 9" black and white photographic prints are available for any photographs or illustrations appearing in this copy for an additional charge. Contact UMI directly to order.

University of Alberta

JUNCTION MIXING SCANNING TUNNELING MICROSCOPY

by

Geoffrey Mark Steeves ©

A thesis submitted to the Faculty of Graduate Studies and Research in partial fulfillment
of the requirements for the degree of **Doctor of Philosophy.**

Department of Physics

Edmonton, Alberta
Fall 2001

The author has granted a non-exclusive licence allowing the National Library of Canada to reproduce, loan, distribute or sell copies of this thesis in microform, paper or electronic formats.

The author retains ownership of the copyright in this thesis. Neither the thesis nor substantial extracts from it may be printed or otherwise reproduced without the author's permission.

L'auteur a accordé une licence non exclusive permettant à la Bibliothèque nationale du Canada de reproduire, prêter, distribuer ou vendre des copies de cette thèse sous la forme de microfiche/film, de reproduction sur papier ou sur format électronique.

L'auteur conserve la propriété du droit d'auteur qui protège cette thèse. Ni la thèse ni des extraits substantiels de celle-ci ne doivent être imprimés ou autrement reproduits sans son autorisation.

0-612-68998-0

Canada

University of Alberta

Library Release Form

**Name of Author:** Geoffrey Mark Steeves

Title of Thesis: Junction Mixing Scanning Tunneling Microscopy

Degree: Doctor of Philosophy

Year this Degree Granted: 2001

Permission is hereby granted to the University of Alberta Library to reproduce single copies of this thesis and to lend or sell such copies for private, scholarly or scientific research purposes only.

The author reserves all other publication and other rights in association with the copyright in the thesis, and except as hereinbefore provided, neither the thesis nor any substantial portion thereof may be printed or otherwise reproduced in any material form whatever without the author's prior written permission.
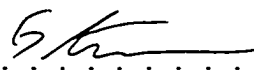
Geoffrey Mark Steeves
Department of Physics
University of Alberta
Edmonton, AB
Canada, T6G 2J1

Date: July 3, 2001

University of Alberta

Faculty of Graduate Studies and Research

The undersigned certify that they have read, and recommend to the Faculty of Graduate Studies and Research for acceptance, a thesis entitled **Junction Mixing Scanning Tunneling Microscopy** submitted by G. M. Steeves in partial fulfillment of the requirements for the degree of **Doctor of Philosophy.**
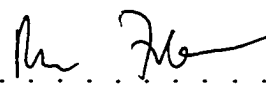
Dr. Mark Freeman (supervisor)
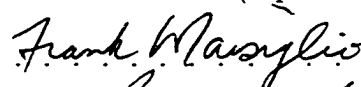
Dr. Frank Marsiglio (chair)
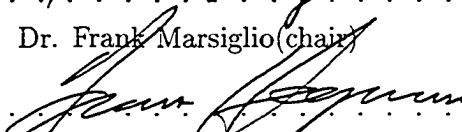
Dr. Frank Hegmann
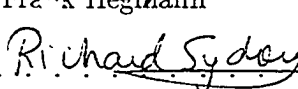
Dr. Richard Sydora

Dr. Arthur Mar

Dr. Geoff Nunes Jr.

Date: 29 June 2001

Abstract

Research in the fields of nanotechnology and nanoelectronics is burgeoning. As nano-devices shrink in size and subsequently electronic operations on these length scales accelerate, new techniques will be required to study and characterize these devices. Techniques with atomic scale spatial resolution and femtosecond time resolution will soon be necessary. Looking to conventional scanning probe microscopy, the scanning tunneling microscope (STM) already possesses sufficient spatial resolution to image any feature current nanotechnologies can produce (STMs are used to build the worlds smallest nano-devices). Similarly ultrafast pump/probe optical techniques exist, which can resolve femtosecond dynamics. The goal of this research is to wed ultrafast optical techniques with the scanning tunneling microscope to produce an aggregate probe with the ability to image nanoscale dynamics. This goal has been achieved using a technique known as junction mixing STM (JM-STM).

Initial work using the junction mixing technique was performed to demonstrate the detection of a time-resolved signal using a home built scanning tunneling micro-scope. This work demonstrated an order of magnitude improvement in time resolution over previous experiments by utilizing ion implanted gallium arsenide substrates to generate fast electrical pulses. This work decisively demonstrated the STM tunnel junction as the origin of the measured time resolved signal, a crucial requirement in maintaining STM spatial resolution.

Following these experiments, new test structures were designed to demonstrate combined STM spatial resolution with picosecond time resolution. Measurements were made on small titanium dots patterned onto a gold transmission line. The titanium provided electronic contrast to the gold, so that our time resolved signal was modulated as we scanned our STM across the titanium/gold interface. Combined 20 ns - 20 ps spatio-temporal resolution was achieved, the first direct confirmation that

time-resolved STM was possible.

These experiments were numerically reproduced using a lumped element circuit model of the non-linear tunnel junction in parallel with STM geometrical capacitance. Results from this model suggest the junction mixing technique should be able to yield time resolution in the hundreds of femtoseconds while maintaining atomic spatial resolution.

To demonstrate the operation of this junction mixing technique efforts were directed to designing and building a low temperature high vacuum STM and a home built Ti/Sapph laser system. These systems are being incorporated into a new low temperature high vacuum time resolved scanning tunneling microscope.

Acknowledgements

I would like to thank my wife Wendy for her love, encouragement and support over the years both together and apart. I would like to thank my parents and my brother Matthew for their interest in, and encouragement of my research. Finally I would like to express deep gratitude to my advisor Mark Freeman. You were a quintessential mentor through my studies and you always made time for advise and discussions of physics and life.

Table of Contents

List of Figures

Chapter 1

Introduction to Time-Resolved Scanning Tunneling Microscopy

1.1 Introduction to Scanning Tunneling Microscopy

1.1.1 Background

The scanning tunneling microscope (STM) was conceived by Binnig and Rohrer in 1978 as a tool to investigate the growth, topography and electronic structure of thin oxide layers [1]. The night of March 16, 1981, the first logarithmic current versus tip height (I/Z) curve was acquired marking the birth of the STM [2]. Early STM investigations of surface topography quickly demonstrated the power of this technique [1, 3, 4, 5]. Since its invention, the scanning tunneling microscope has had a profound impact in the field of microscopy, and in the development of nanotechnology. Atomic force microscopy (AFM) [6], magnetic force microscopy (MFM) and scanning tunneling spectroscopy [2, 7, 8, 9, 10] were all inspired by the STM. Scanning tunneling microscopes have been used to study surface topography [11], chemical bonding [12], conduction through nano-wires [13] and superconductivity [14, 15]. STM studies have been performed at temperatures ranging from milli Kelvin up to hundreds of degrees Celsius; from ultra high vacuum to liquid immersion; and across spatial extents ranging from Angstroms up to tens of micrometers. These feats establish STM as the most significant advance in microscopy since the development of electron microscopy in the 1930's [16, 17]. For this work Binnig and Rohrer were awarded the 1986 Nobel Prize

1

for Physics. Research in scanning tunneling microscopy has been deep and rich, bearing many unexpected rewards. One of the most fantastic has been the work by Don Eigler to develop atom manipulation and atom engineering [18]. Nano-structures, never seen before in nature can now be built atom by atom allowing unprecedented investigations into surface physics, magnetism and superconductivity.

Through all the versatility of this microscopy, one domain has remained elusive, the ultrafast time domain. All STM work in the 1980's was confined to the bandwidth of the STM feedback electronics (typically a few kHz). Bringing time-resolution to an STM would open a new dimension for researchers to explore. Electronic or mechanical dynamics on atomic length scales could be probed. Magnetic dynamics could be investigated, through spin polarized STM. In fact almost any property measurable by an STM could be studied dynamically. One natural question to pose is, what limits the ultimate speed of a time-resolved STM ? With sophisticated electronics, one could attempt real time measurement of current transients measured in the STM tunneling current, but this technique will not work below nano-second time-scales. Tunneling rates at typical tunneling currents of 1 nA correspond to about 6×10^9 electrons tunneling every second. If one were trying to make single shot measurements in less than one nano-second there would be no electrons to detect. An alternate approach would be to use pump/probe techniques to repetitively measure the same event.

Pump/probe optical techniques rely on the repeated stimulation and synchronous measurement of a system. The system under investigation is repeatably pumped(or excited) out of equilibrium at time t_1 and then probed at some different time t_2. If the evolution of the sample is deterministic then repeating the pump/probe investigation over many optical pulse cycles will increase the signal to noise ratio of the measurement. By measuring the pump/probe signal for a fixed delay and then incrementing the relative delay between pump and probe pulses the time evolution of the sample

2
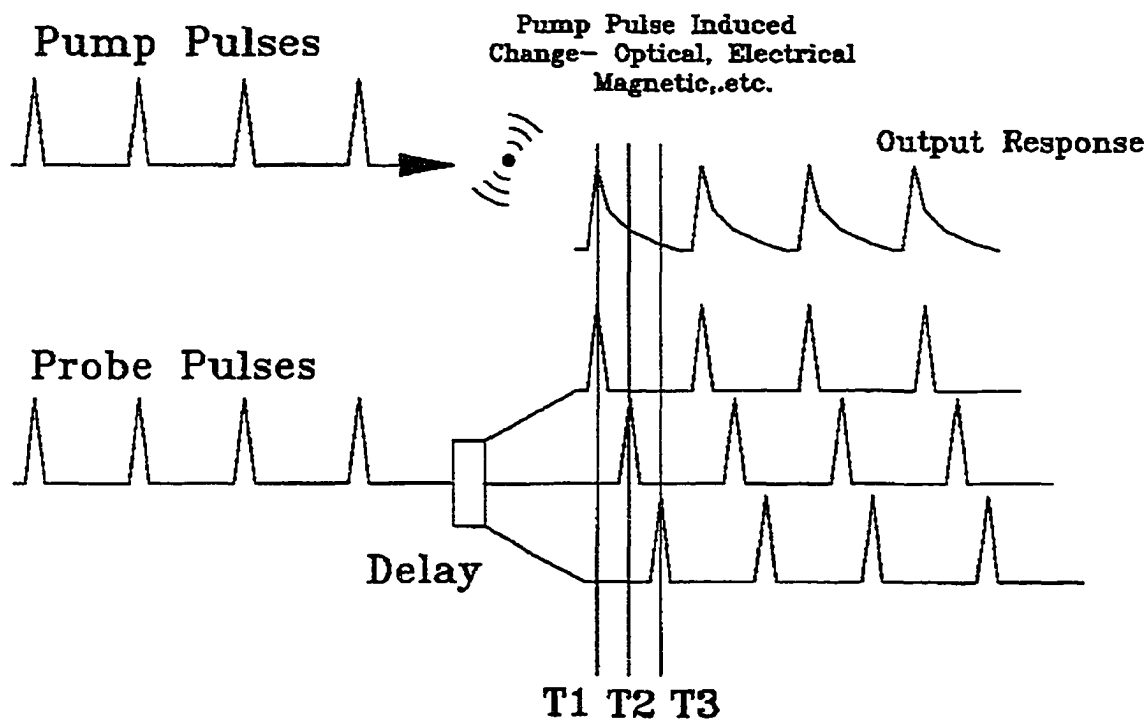
Figure 1.1: Pump pulse train repeatably stimulates the sample, which has a response to the stimulation shown on the top right quadrant of the figure. The probe pulse train is delayed by an amount T1, T2 or T3, and probes the response of the pumped system at these different times. By varying the delay time between pump and probe pulse trains the response of the system can be mapped out.

can be mapped out. This is shown schematically in Figure 1.1.

The body of this thesis will elucidate the incorporation of ultrafast temporal resolution into the domain of the scanning tunneling microscope. To begin with, the basic operation of an STM and some of its common uses will be discussed.

The simplest way to understand the operation of an STM is to focus on its unique characteristic, electron tunneling across a small gap between a sharp metallic tip and the surface of a conducting sample[1]. In tunneling, electrons with (classically) insufficient energy to cross the potential barrier between tip and sample are able to "tunnel" through. The first use of quantum mechanics to describe a tunneling

---

[1]Sharp metallic tips, and metallic samples are not required for tunneling, but are simplifications made for the purpose of illustration

3

phenomena was published by Fowler and Nordheim in 1928[19], as they used the "new mechanics" in their description of field emission. Bringing a tip and sample into close proximity will increase the probability that an electron will tunnel between the two. Tunneling will occur in both directions but by applying a bias voltage between tip and sample a net tunneling current can be established in the volume known as the tunnel junction. This tunneling current has some special characteristics which determine the properties of the scanning tunneling microscope.

- The tunneling current changes exponentially with tip/sample separation

- The current is spatially dependent on the shape of the active (tunneling) wavefunctions of tip and sample

- The rate of change of the tunneling current with respect to applied voltage is correlated with electronic properties of the sample

The first point suggests that an STM will have excellent sensitivity to changes in topography, as the tunneling current will change drastically for small changes in the distance between tip and sample. In addition the exponential decay constant (effective work function) can give information on the quality of the sample surface, since surface impurities such as oxide layers will drastically effect the decay constant. The second point suggests that an STM will have lateral resolution related to a convolution of the tip and surface wavefunction. The third point implies that an STM could be used for determining information about the local electronic properties of a sample being studied. With these "potential" features in mind, the basic design of an STM will be discussed.

1.1.2 A typical STM and its applications

Mechanical design is a fundamental requirement to exploit the first two properties mentioned, and create a microscope capable of measuring topographic features on a surface . The microscope must allow for atomically precise positioning of a sharp tip

4

above a sample of interest. This requires an approach mechanism which can bring the tip from macroscopic separations of millimeters down to the nanometer range separation necessary to attain a measurable tunneling current. Once separation is of this order, there needs to be a fine control actuator capable of moving the STM tip laterally and vertically with sub Å resolution. In the present example a piezo-electric cylindrical tube (PZT tube [2]) will be used for this purpose. Piezo-electric materials were discovered by Pierre and Jacques Curie in 1880 [20]. They are ferroelectric or antiferroelectric and will change their structure when voltages are applied across them. A piezo tube can act as a mechanical actuator with sub Å precision [21]. The system must be stabilized and isolated from environmental interference such as mechanical vibrations and electrical noise. Mechanical vibrations cause relative motion between tip and sample distorting the tunneling current. Similarly electrical noise will obscure the tunneling current. The typical microscope operates with the tunneling current between tip and sample maintained through a feedback system. The current is kept constant by adjusting the height of the STM tip above the sample surface. The tip is scanned over a small area on the sample surface using a computer to initiate the scan and record the relative tip height while the feedback loop maintains constant current. In this manner we form an image of the topography of the surface.

The control and measurement electronics are shown schematically in Figure 1.2. Illustrated is a sample at a potential determined by the applied bias voltage. The STM tip is positioned above the sample and mounted in a cylindrical piezo tube which controls tip position in 3 axes (with a small amount of cross coupling between the x-y and the z axis) as control voltages are applied through the high voltage amplifier. Current signals from the STM tip are amplified in a current pre-amp (typical pre-amp gain is $10^8 \rightarrow 10^9 V/A$) and sent to the feedback controller. Changes in tunneling current are minimized as the feedback controller is connected to the tip height (Z)

---

[2]PZT is an industry name for lead, zirconate titanate, a single phase solid solution of $PbZrO_3$ and $PbTiO_3$

5
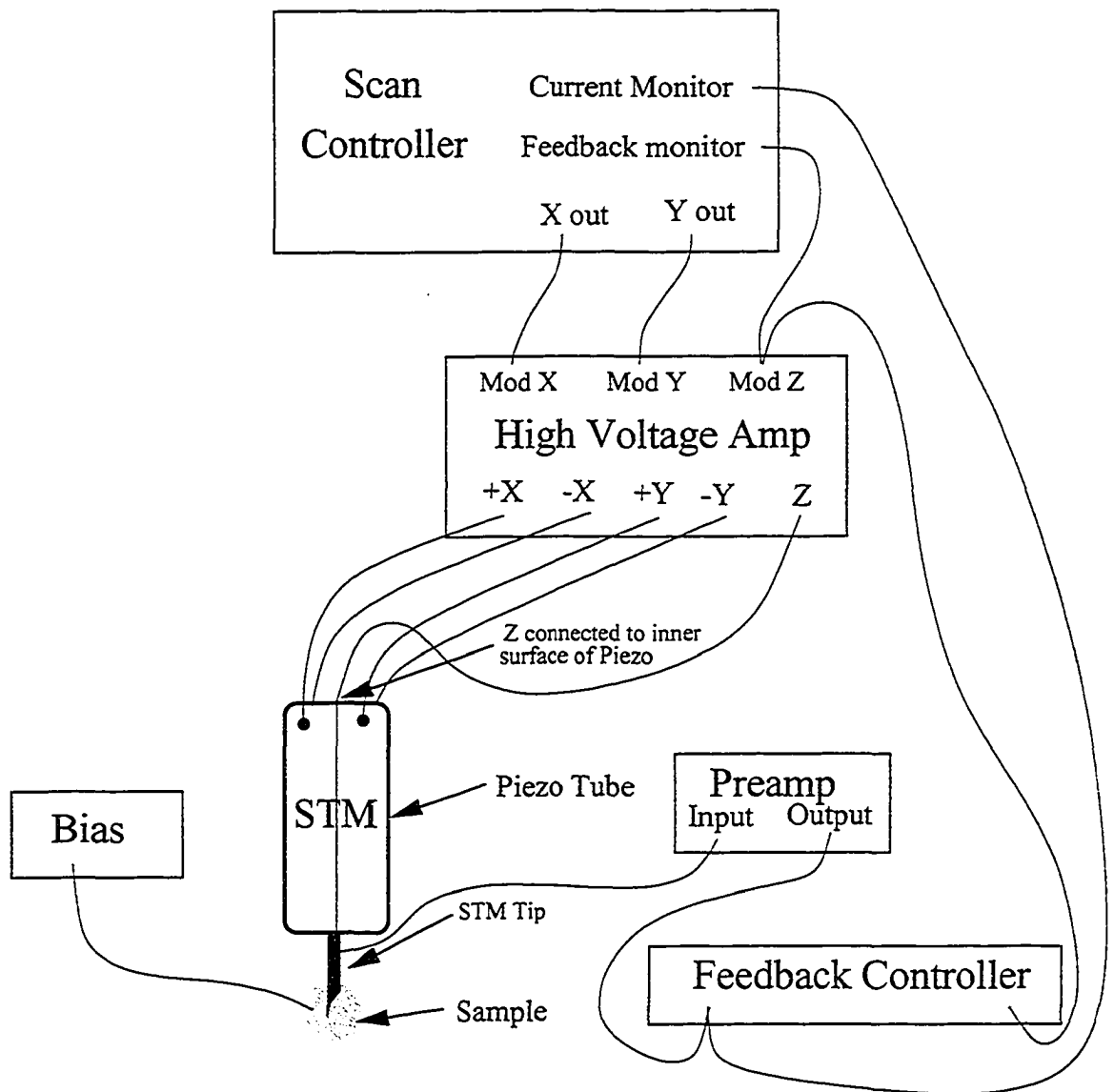
Figure 1.2: Basic elements of a Scanning Tunneling Microscope

6

input of the high voltage amp, allowing the STM tip to approach or withdraw from the sample surface to maintain a constant tunneling current. While efforts to maintain a constant tunneling current are made, the current is monitored and recorded by the scan controller to assess the effectiveness of the feedback system. The scan controller also monitors the output of the feedback controller as it adjusts the tip height above the sample. When a scan is initiated by the scan controller it outputs voltages to the high voltage amplifier directed to the x and y electrode pairs of the piezo. These voltages cause deflection of the piezo tube allowing it to scan the tip across the sample surface.

With a configuration such as that shown in Figure 1.2 all of the unique features of the tunneling current can be exploited to glean information about the sample through tunneling microscopy. The vertical resolution of the scan is related to the effective work function of the tunnel junction. Surface impurities can assist tunneling by lowering the effective work function, while a cleaner junction yields a higher work function and better topographic sensitivity. The lateral resolution also varies with work function and the electronic states of the STM tip. If electrons are tunneling into highly localized orbitals on the STM tip, the lateral resolution will be better than simply tunneling into an electronically uniform tip. The "electronic" shape of the tip is a key characteristic of STM topographic scans, and much work has been done to model and characterize STM tip shapes.

Topographic STM scans were one of the first uses which STM fulfilled, allowing direct imaging of atomic surface structures. The first clear demonstration of the power of the STM was in resolving the geometrical puzzle of the 7×7 surface reconstruction of Si (111) [11, 22]. In 1959 low-energy electron diffraction on the reconstructed Si (111) surface showed that there was a 49 atom unit cell. This cell seemed to have *p6mm* symmetry but the configuration of the 49 atoms within the unit cell was

7
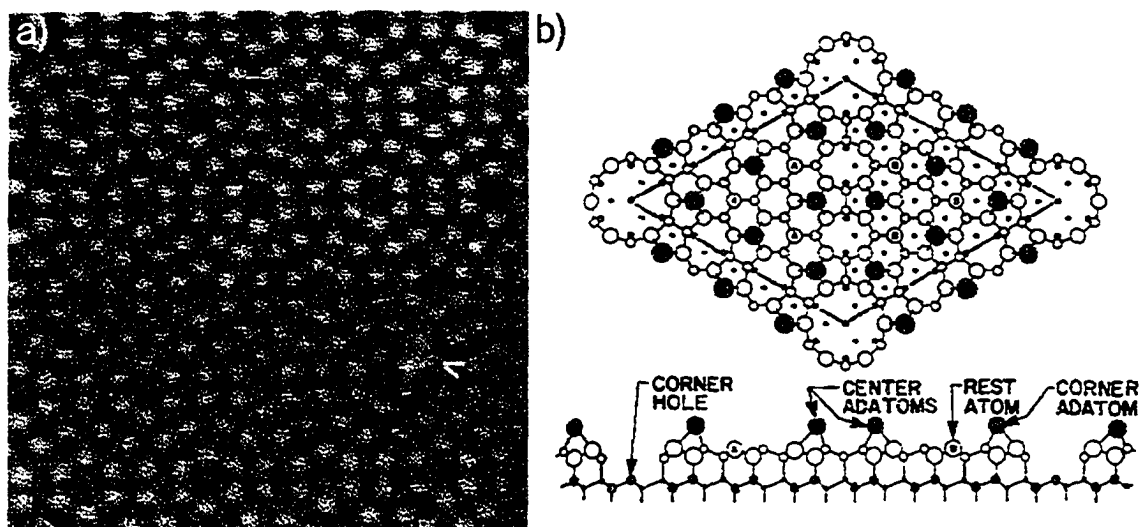
Figure 1.3: 7 × 7 reconstruction on Si (111); panel a) shows STM topographic scan; panel b) shows calculated structure.

unknown. Many models were proposed but the exact structure remained a mystery through 20 years of investigation until an STM directly imaged the surface. Direct imaging revealed that all the proposed models were incorrect and the true symmetry of the unit cell was *p3m1*. The first published STM reconstruction is shown in cell a) of Figure 1.3. The reconstruction is not completely observed as 12 adatoms obscure the full view but from the configuration of adatoms the underlying structure was determined [3]. The full 3 dimensional unit cell published in reference [22] is shown in Figure 1.3 panel b), where the 12 top-layer adatoms form the trapezoid between vacant centers of the surface structure.

Apart from topographic scans in constant current mode, there are other significant modes of operating the STM. Foremost of these is current-voltage or I/V spectroscopy. In typical STM operation, the tip height is maintained using feedback to achieve constant current with a fixed DC bias between tip and sample. Increasing the DC bias will raise the net current and subsequently the feedback system will withdraw the tip reducing the current back to its original value. If however, the feedback system

---

[3] Through reaction with chlorine the adatom layer can be removed and the beautiful underlying structure imaged, see [23]

8

were disabled, the tunneling current would increase to a new equilibrium value. The response of the tunnel junction to variations of the bias voltage can yield insight into the electronic structure of STM tip and sample. By temporarily suspending feedback and monitoring the tunneling current while ramping the bias voltage an I/V curve can be acquired. It turns out (this will be shown in subsequent sections) that $\frac{\partial I}{\partial V}$ is directly proportional to the density of states of the sample at the location of the STM tip. By performing I/V scans at different points on a sample surface, a $\frac{\partial I}{\partial V}$ or density of states map of the sample can be created at a particular energy. This modality of the STM allows the creation of spectacular images such as the imaging of the local density of states (LDOS) of $NbSe_2$ shown in Figure 1.4. In this experiment Harald Hess imaged the Abrikosov flux lattice of $NbSe_2$ at 1.8 Kelvin and in a field of 1 Tesla. The lattice is visible since the density of states for $NbSe_2$ is suppressed within the energy gap of the superconducting $NbSe_2$, but reappears in the normal cores of the vortices. This work is quite interesting in that it could be considered a continuation of work by Binnig and Rohrer, since their original motivation for inventing the instrument that became an STM was to develop a local electronic structure probe for studying superconductivity.

1.1.3 STM Fundamentals

Now that some of the basic features and modalities of STM have been touched upon, we will delve a little deeper into the quantum mechanics which found its operation. Through this we will illustrate how the "features" of the tunnel junction can be derived as well as how more precise calculations of tunnel junction properties can be approached.

To understand the basic operation of a scanning tunneling microscope it is first necessary to outline the underlying quantum mechanics. Beginning with a simple model we will endeavor to illustrate some simple features of the phenomena of quan-
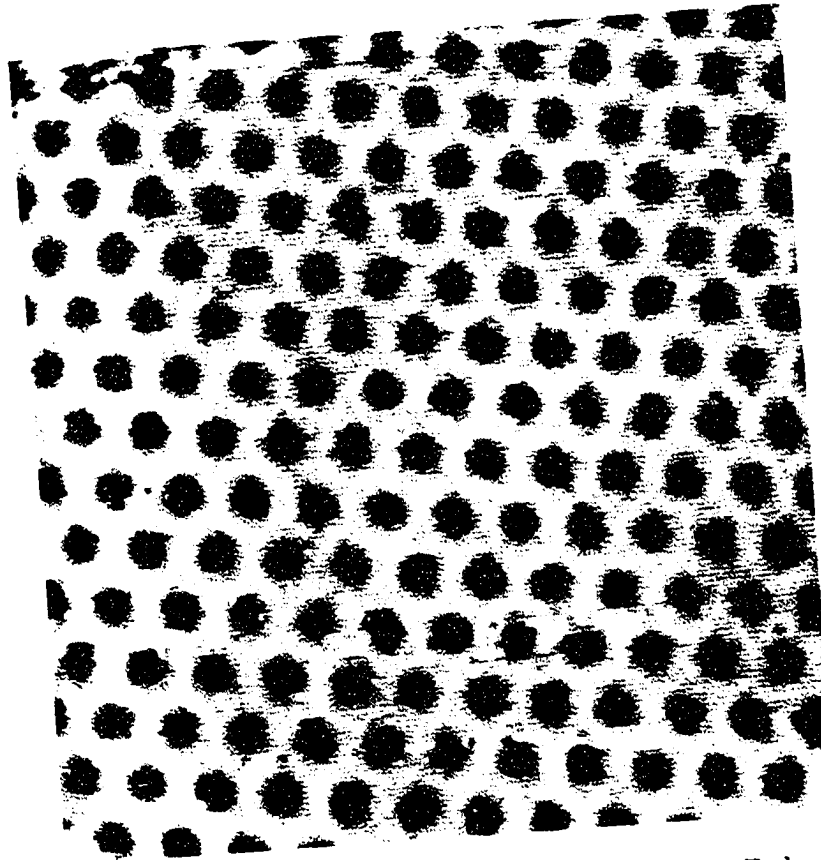
Figure 1.4: 600 × 600 nm scan of NbSe$_2$ at 1.8K in a field of 1 Tesla, $\frac{dI}{dV}$ ranges from $1 \times 10^{-8}\mho$ (black) to $1.5 \times 10^{-9}\mho$ (white).

10
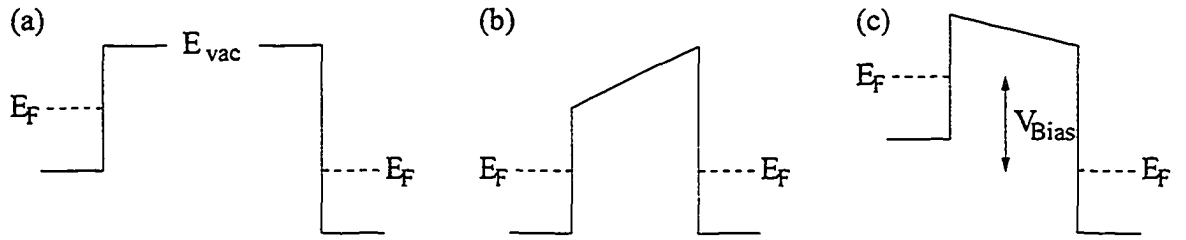
Figure 1.5: (a) Two metals well separated by a vacuum gap, the Fermi levels are separated by the difference in work function between each metal. (b) Metals are brought close together and reach an electronic equilibrium where they share a common Fermi level. (c) A bias voltage introduces a Fermi level shift between the two metals. Only electrons below the Fermi level on the left can tunnel into states above the Fermi level on the right.

tum tunneling. As we bring the metal STM tip towards the sample, the difference in Fermi energies between the metals is equal to the difference between their respective work functions, shown in panel (a) of figure 1.5. As the tip and sample are brought close enough that tunneling begins between tip and sample, an electronic equilibrium is established as a common Fermi level between the two metals, shown in panel (b). An electric field is also established due to the differing work functions of the two metals. If a bias voltage is applied between STM tip and sample the Fermi levels of each metal are shifted until their separation is equal to the bias voltage as shown in panel (c).

A simplified tunneling barrier, shown in figure 1.6 captures the essential character STM tunneling. Examining a free electron and a potential barrier (where the energy of the electron E is less than that of the potential barrier V_0) , we can write down the single particle Schrödinger equation:

$$\frac{-\hbar^2}{2m} \frac{d^2}{dx^2} \psi(x) + V(x)\psi(x) = E\psi(x) \tag{1.1}$$

Solving the Schrödinger equation on the left hand side of the barrier, shown in Figure 1.6, gives:

$$-\frac{\hbar^2}{2m} \frac{d^2}{dx^2} \psi_1(x) = E\psi_1 \tag{1.2}$$

$$\psi_1 = Ae^{ikx} + Be^{-ikx} \tag{1.3}$$

11
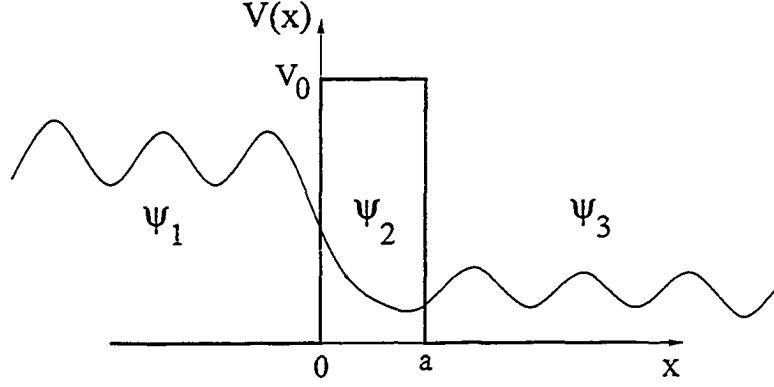
Figure 1.6: Potential Barrier

where $k = \sqrt{\frac{2mE}{\hbar^2}}$. Examining ψ inside the tunneling barrier where $E < V_0$:

$$\frac{\hbar^2}{2m}\frac{d^2}{dx^2}\psi_2 = (V_0 - E)\psi_2 \tag{1.4}$$

$$\psi_2 = Ce^{k'x} + De^{-k'x} \tag{1.5}$$

where $k' = \sqrt{\frac{2m(V_0-E)}{\hbar^2}}$. Finally looking at the right hand side of the tunneling barrier:

$$-\frac{\hbar^2}{2m}\frac{d^2}{dx^2}\psi_3(x) = E\psi_3 \tag{1.6}$$

$$\psi_3 = Fe^{ik''x} + Ge^{-ik''x} \tag{1.7}$$

where we set $G = 0$ for an incoming particle from the left, and where $k'' = \sqrt{\frac{2mE}{\hbar^2}}$ Matching equations 1.3 and 1.5 and their first derivatives at the $x = 0$ boundary gives us:

$$A + B = C + D \tag{1.8}$$

$$ik(A - B) = k'(C - D) \tag{1.9}$$

While matching equation 1.5 and 1.7 at the $x = a$ boundary gives:

$$Fe^{ik''a} = Ce^{k'a} + De^{-k'a} \tag{1.10}$$

$$ik''Fe^{ik''a} = k'(Ce^{k'a} - De^{-k'a}) \tag{1.11}$$

12

Eliminating variables C and D we can solve for the ratio's $\frac{B}{A}$ and $\frac{F}{A}$ also noting that by definition $k'' = k$, we write:

$$\frac{B}{A} = \frac{(k^2 + k'^2)(e^{2k'a} - 1)}{e^{2k'a}(k + ik')^2 - (k - ik')^2} \tag{1.12}$$

$$\frac{F}{A} = \frac{4ikk'e^{-ika}e^{k'a}}{e^{2k'a}(k + ik')^2 - (k - ik')^2} \tag{1.13}$$

At this point it would be possible to solve explicitly for A, B and F by normalizing the wavefunction $\int_{-\infty}^{+\infty} \psi^*(x)\psi(x)dx = 1$, but it is more convenient to simply calculate the reflection and transmission coefficients where the reflection coefficient is given by:

$$R = \frac{|B|^2}{|A|^2} = \left[1 + \frac{4E(V_0 - E)}{V_0^2 \sinh^2(k'a)}\right]^{-1} \tag{1.14}$$

And the transmission coefficient is given by:

$$T = \frac{|F|^2}{|A|^2} = \left[1 + \frac{V_0^2 \sinh^2(k'a)}{4E(V_0 - E)}\right]^{-1} \tag{1.15}$$

For effectively large tunneling barriers where $k'a \gg 1$, $\sinh^2(k'a) \approx \frac{e^{2k'a}}{4}$ so that T is given by:

$$T \approx \frac{16E(V_0 - E)}{V_0^2} e^{-2k'a} \tag{1.16}$$

The value $(2k')^{-1}$ can be thought of as a characteristic range for tunneling. Choosing a typical barrier height of $(V_0 - E) = 3$ eV and a tip height of 3 Å gives us a value $e^{-2k'a} = 4.89 \times 10^{-3}$. [4] From equation (1.16) we ascertain some essential characteristics of the tunnel junction. The tunneling transmission probability and hence the tunneling current will vary exponentially with tip/sample separation and the tunneling current will also vary exponentially with the square root of the effective tunneling barrier height (since $k' = \sqrt{\frac{2m(V_0 - E)}{\hbar^2}}$). This extreme current dependence on tip height suggests that the STM should have excellent resolution to small changes in sample topography. A topographic change towards or away from the surface of 1 Å can change the value of the exponential in equation 1.16 from 4.9×10^{-3} to 2.9×10^{-2}

---

[4]Comparing this with $\{4\sinh^2(k'a)\}^{-1} = 4.9 \times 10^{-3}$ shows that the approximation is sufficient in a reasonable tunneling configuration.

13

or 8.3×10^{-4} respectively, an order of magnitude change in tunneling current for a height change of just 1 Å! This exponential dependence can be seen over many orders of magnitude as the STM tip is withdrawn from a sample surface as shown in the early work of Binnig, Rohrer et al. [24].

In order to better explain the exact form of the tunneling current it is necessary to develop a detailed model of STM tip and sample. Features of this model will be the modification of tip and sample wavefunction as the two are brought into close proximity, and the detailed electronic states of tip and sample.

A detailed description of the theory of STM modeling can be found in chapters 2, 3 and 4 in Chen's "Introduction to Scanning Tunneling Microscopy" [21]. In this reference Chen details the development of the modified Bardeen approach, to model STM tunneling current. Comparisons are made with some exactly solvable quantum systems, and detailed approaches to calculate the tunneling matrix element are given. The fundamental equation of interest in calculating tunneling current is derived as:

$$I = \frac{4\pi e}{\hbar} \int_{-\infty}^{+\infty} [f(E_F - eV + \epsilon) - f(E_F + \epsilon)] \tag{1.17}$$
$$\times \rho_S(E_F - eV + \epsilon)\rho_T(E_F + \epsilon)|M|^2 d\epsilon,$$

where $f(E) = (1 + e^{\frac{(E-E_F)}{k_B T}})^{-1}$ is the Fermi distribution function used for both tip and sample in the above equation. ρ_S is the sample density of states and ρ_T is the tip density of states. M is the tunneling matrix element, which is related to the interaction between tip and sample states. From here we can simplify equation 1.17 by substituting a step function for the Fermi distribution allowing us to write:

$$I = \frac{4\pi e}{\hbar} \int_0^{eV} \rho_S(E_F - eV + \epsilon)\rho_T(E_F + \epsilon)|M|^2 d\epsilon. \tag{1.18}$$

If we have an STM tip with a constant density of states ρ_T then the tunneling current can be written as:

$$\frac{dI}{dV} \propto \rho_S(E_F - eV), \tag{1.19}$$

14

where we see that the derivative of the STM tunneling current is a direct local probe into the sample local density of states at the applied bias voltage V. Returning to equation 1.17, the tunneling matrix M is given by:

$$M = -\frac{\hbar^2}{2m} \int \left(\chi_\nu^* \nabla \psi_\mu - \psi_\mu \nabla \chi_\nu^* \right) \bullet d\vec{S}, \qquad (1.20)$$

where ψ_μ is the wavefunction of the sample and χ_ν is the wavefunction of the tip. In determining the wave function of the tip we limit our choice to wavefunctions extending out of the tip into the vacuum between tip and sample. Following Chen's derivation one finds that for a given tip state, there exists a matrix element operator for the surface state.

This result, first derived by Tersoff and Hamann [25, 26] reduces the calculation of the matrix element to the problem of simply finding the appropriate surface wavefunction.

To determine the surface wavefunction many models have been developed. These models account for bulk Bloch wave states through the material, surface states which would be forbidden in the bulk material as they would rest within material bandgaps, and surface resonant states which are surface states with overlapping bulk Bloch states. One of the early models of the electronic structure of a metal surface is the Jellium model. This model consists of a bulk Sommerfeld free-electron model where the background ion potential drops to zero at the surface. Using this model, Bardeen [27] estimated the work function of various metals and found fair agreement with observation (within about 25%). This model is not particularly useful as it does not incorporate any atomic structure necessary to predict things like surface states, however this model has found use in calculating surface wavefunctions for single adatoms on a surface as shown by Eigler et al. [28]. A model explicitly predicting the existence of surface states was formulated in 1932 by Tamm [29], based on a Krönig-Penney potential with a boundary. But the most accurate and successful calculations of surface wave functions are first principle calculations using density-functional theory. Using

density-functional theory Appelbaum and Hamann pioneered the first calculations of electronic surface structure examining sodium and aluminum in the early 1970's [30]. Of course it is of great interest and use to be able to calculate surface wavefunctions, but STM measurements provide a simple and effective way to access this same information, through local density of states measurements.

The origins of the STM tunneling current can now be seen. Beginning with the equation for tunneling current, we substitute in the Fermi functions for STM tip and sample. Then we approach the tunneling matrix element, using the appropriate STM tip wavefunction (determined by the material and detailed shape of the STM tip apex) and calculated surface wavefunction. The significance of both the tip and surface wavefunction on the tunneling current belies the assumption that STM images always convey true surface topography. Care must be taken in any interpretation of an STM topographic scan. A dramatic example of how the tip wavefunction can affect topographic images is shown in Figure 1.7 from work by Mizes, Park and Harrison [31]. The left image of each pair labelled a) through d) is an actual STM scan while the right image is computer generated using a model tip geometry (since the geometry of the tip atoms dictate the overall tip wavefunction shape). Only panel a) shows the accurate topography of the graphite sample being studied. The images from panels b) through d) show actual STM images of a graphite surface but because the tip of the STM had multiple atoms involved in tunneling the images do not display the true topography of the surface.

Now that the basic principles of STM operation have been discussed we will begin discussion into methods to add ultra-fast time resolution to this microscopy.

16
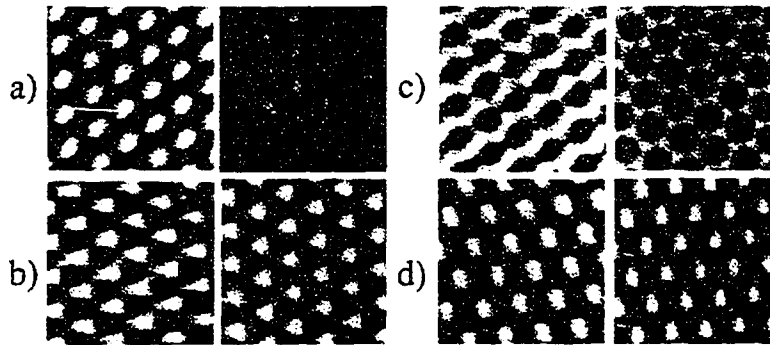
Figure 1.7: Anomalous STM images of graphite.

1.2 History of Time Resolved STM

1.2.1 Initial Developments in Time-Resolved Scanning Probe Microscopy

The young field of time resolved scanning tunneling microscopy has mysterious o-
rigins. The first proposal can be traced back to a two paragraph note published
anonymously as Research Disclosure # 30480 in August 1989 in the journal Re-
search Disclosures [32]. This disclosure, entitled "Contactless, High-Speed Electronic
Sampling Probe" proposes the use of a vacuum tunneling probe to sample electrical
transients which are produced optically or electronically and rectified by the nonlin-
earities of the current-voltage characteristic of the tunnel junction. Due to the brevity
of the article it will be quoted below:

> "A vacuum tunneling probe may be used for the sampling of
> electrical transients.
>
> The sampling device consists of a metal tip in close proximity to an
> electrical conductor in which the transient propagates. An optical pulse
> incident on this metal-vacuum-metal tunneling junction is rectified by non-
> linearities in the current-voltage characteristic of the junction. The coinci-
> dence of electrical and optical pulses changes the junction response, thereby
> providing a cross-correlation of the pulses. By varying the delay between
> the pulses, the complete cross-correlation is obtained. This vacuum tun-
> neling junction is expected to have a frequency response better than 200
> THz (5 fs). The contactless probe may also be laterally scanned in order
> to probe different parts of the circuit. With a scan length of the order of

microns, it is possible to look for inhomogeneities and defects of individual elements in an integrated circuit.

The sample is shown schematically in the drawing[figure not shown]. A DC tunneling current i_b produced by a DC voltage bias is used to maintain a constant tip-sample separation. Electrical pulses at the junction will effectively change the bias, producing a current i_e. Optical pulses will be rectified by the nonlinearities of the junction producing a current i_o. Because the nonlinear properties of the junction depend on the bias, coincident optical and electrical pulses will produce an additional component i_{oe} of the total current. This component provides a measure of the cross-correlation between electrical and optical pulses. The correlation signal i_{oe} may be enhanced using difference frequency lock-in techniques. We note that even without the presence of optical pulses, this device may be used for contactless electrical sampling with conventional electronic bandwidths due to the current i_e. We also note the possibility of using this sampler, in conjunction with the vacuum tunneling pulse generator, to measure the transient response of a circuit or device with subpicosecond resolution and also as a broadband autocorrelator to measure subpicosecond laser pulse widths."

Due to the unusual nature of this publication, and the small audience which received it, little was known of time resolved STM until the independent work of Hamers and Cahill [33, 34]. The primary paper, entitled "Ultrafast time resolution in scanned probe microscopies", demonstrated the first attempt to combine laser methods for ultrafast time resolution with a scanning capacitance microscope. The authors went further though, in outlining the technique and requirements to add ultrafast time resolution to scanning probe microscopes in general (their original motivation had been to attempt a time-resolved detection of surface photovoltage using a scanning tunneling probe).

The process that the authors studied was the decay of photoexcited carriers at a Si (111) (7 × 7) surface. Their experimental setup is shown in Figure 1.8.
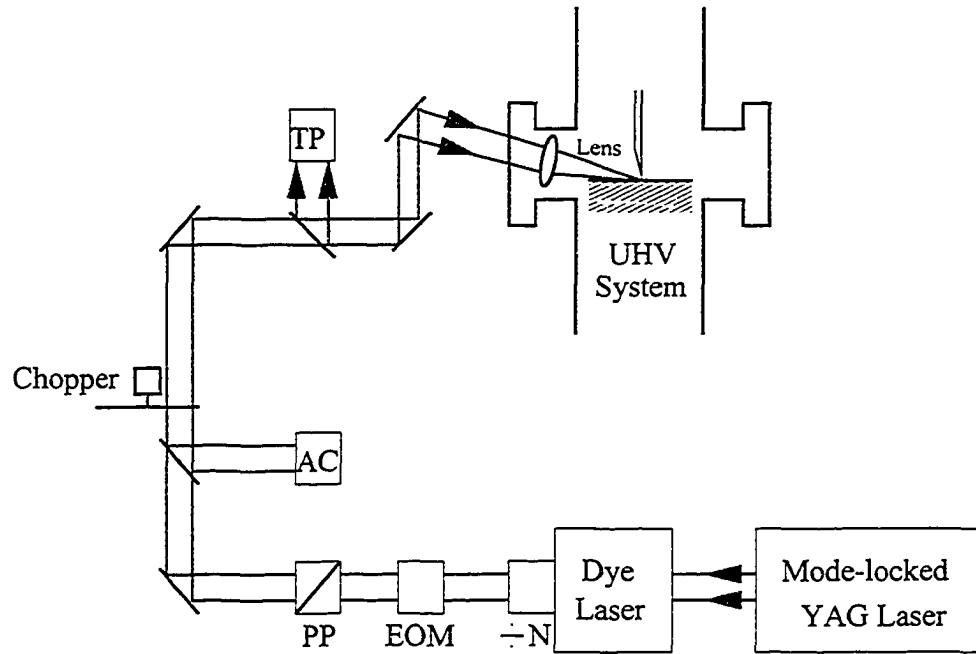
Figure 1.8: Schematic diagram of experimental apparatus. $\div$ N = Cavity dumper, EOM = electro-optic modulator, PP = polarizing prism, AC=autocorrelator, TP = thermopile detector.

In this scheme, they proposed that, "Using the SXM[5] probe tip as a local detector of a deviation from equilibrium which is a nonlinear function of an externally controlled stimulus (such as an optical pulse), it is possible to achieve unprecedented time resolution which is limited only by the inherent time scale of the underlying physical process."

In their experiment a scanning capacitance microscope was used as the local probe, and optical pulses from a dye laser were used to create a transient surface photo-voltage (SPV) which was detected by the probe. Using a capacitive probe allows the tip sample separation to be large minimizing the effects of photothermal expansion or sample and tip due to laser intensity fluctuations. Under continuous illumination the magnitude of the SPV varies as:

$$SPV \approx A\ln(1 + C\delta Q/Q) \tag{1.21}$$

---

[5]Where SXM refers to a generic scanning probe microscopy

19
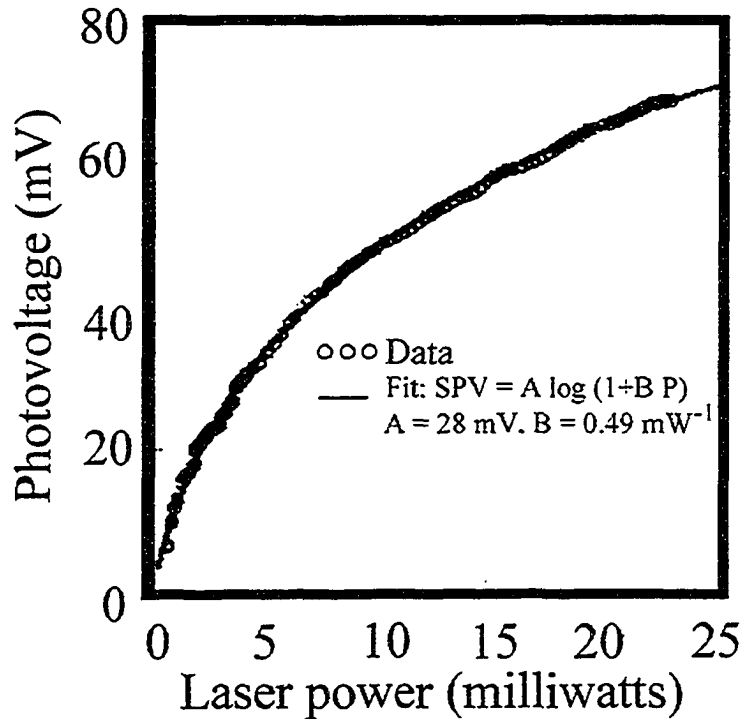
Figure 1.9: Dependence of SPV on incident power using 1 ps pulses separated by 13.1 ns.

where A and C are constants and δQ is the photoexcited carrier density [35]. Under pulsed illumination using 1 ps pulses every 13.1 ns the SPV can be fit with this same equation (with modified values of A and C) as shown in Figure 1.9. The fitting curve was generated with A=28 mV which is almost identical to the value A=31 mV found under continuous illumination suggesting that carrier relaxation occurred on time scales slower than 13.1 ns. To probe carrier relaxation on longer time scales a cavity dumper was used to vary the repetition rate of laser pulses at the sample surface. One picosecond duration excitation pulses would arrive with a spacing (in time) in increments of $\tau_{ML} = 13.1$ ns. The authors measured the average photo-voltage as they varied the repetition rate of their excitation pulses from τ_{ML} to $40 \times \tau_{ML}$ while maintaining a constant time averaged illumination intensity. In this way they could look for deviations from Equation 1.21.

20

When the cavity dumper repetition rate was high with respect to the carrier relaxation time, a large carrier density would be established producing a saturated SPV and measured displacement current signal (through repeated pumping of the sample). For a long repetition rate (compared to the recombination time) most photo-carriers recombined diminishing the SPV before the next excitation pulse resulting in a diminished current signal. The excitation pulse train was optically chopped at 4 kHz so that a lock-in amplifier could be used for detecting and discriminating the time resolved signal. An averaging transient recorder measured the displacement current induced in the tip at 4 kHz. Integrating the displacement current over the "on" time of the chopper gave an averaged value proportional to the time-averaged SPV. A SPV plot with respect to the pulse separation time is shown in Figure 1.10.

This curve was fit and a $1\mu s$ carrier decay time was deduced in the limit of small photovoltages. This experiment was the first to use a scanning probe to detect a signal with fast transient origins. The authors did not report on the effect of scanning the detector over the silicon surface so combined spatio-temporal resolution was not demonstrated. The technique used to achieve time-resolution in this case relied solely on properties of the sample under investigation. The saturation of the SPV at different pump powers and pump repetition rates allowed the authors to deduce the carrier recombination time for the Si (111) surface, but this technique is not generalizable for time-resolved studies of other material properties. Nonetheless the authors demonstrated the first use of a local probe to investigate the $1\mu s$ photoexcited carrier recombination time of a Si (111)-(7 × 7) surface.

1.2.2 Time-Resolved Electrostatic Force Microscopy

Two years after the work by Hamers and Cahill, the group of Hou, Ho and Bloom published results demonstrating picosecond time resolution using a scanning electrostatic force microscope (SFM) [36]. Atomic force microscopes (AFM) had only been invented about 6 years earlier by Binnig, Quate and Gerber [6] and were already

21
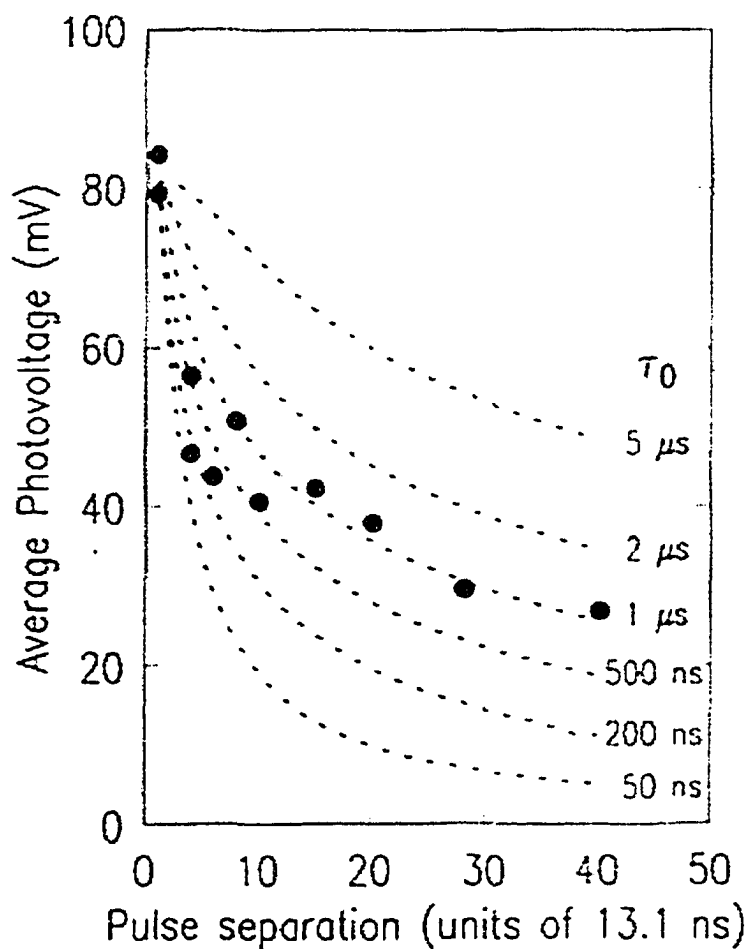
Figure 1.10: Time dependence of surface photovoltage, obtained by measuring the displacement current induced in the tip as a function of delay time between optical pulses, at constant average illumination intensity. Individual points were measured in random order.

22

acquiring a great number of industrial applications due to their flexibility and ease of use. Adding ultrafast time resolution to a modified AFM would prove to be not only interesting, but quite practical. In the Hou, Ho, Bloom scheme the nonlinear force $F = -\frac{\epsilon_0 A V^2}{2z^2}$ between SFM tip and the sample would serve to mix the excitation response of the system with a time varying probe signal. This differed from the Hamers and Cahill experiment where they used repetitive pumping at differing time intervals to build a measurable signal (there was only a pumping stimulus and the frequency of this stimulus was varied). In the Hou, Ho, Bloom configuration two different signals, a pump and a probe signal at different frequencies were mixed in the force nonlinearity to produce a difference frequency signal within the bandwidth of the SFM cantilever and electronics.

In demonstrating this technique the authors combined the 1 Volt outputs of two synthesized sinusoidal signals at frequencies f and $f + \Delta f$, and launched the combined signal down a transmission line (TRL). The fundamental frequency f=1GHz was used and Δf was varied from 0 $\rightarrow$ 25 kHz. The deflection amplitude of the cantilever is shown in Figure 1.11.

The 19 kHz peak corresponds to the mechanical resonance frequency of the cantilever. By characterizing the mechanical resonances of the SFM tip, the mixing signal can be obtained. Similar mixing experiments were successful up to 20 GHz, limited by the quality of the experimenters' high speed electronics.

This group also performed experiments in the time domain using a pair of step-recovery-diode (SRD) comb generators, which produced 110 ps pulses at 500 MHz and 500 MHz + 10 Hz respectively. These pulse trains were combined and launched onto a co-planar waveguide structure patterned onto a GaAs substrate. The beat pattern from the two pulse trains is shown in Figure 1.12, where a 130 ps correlation between pulse trains is shown.
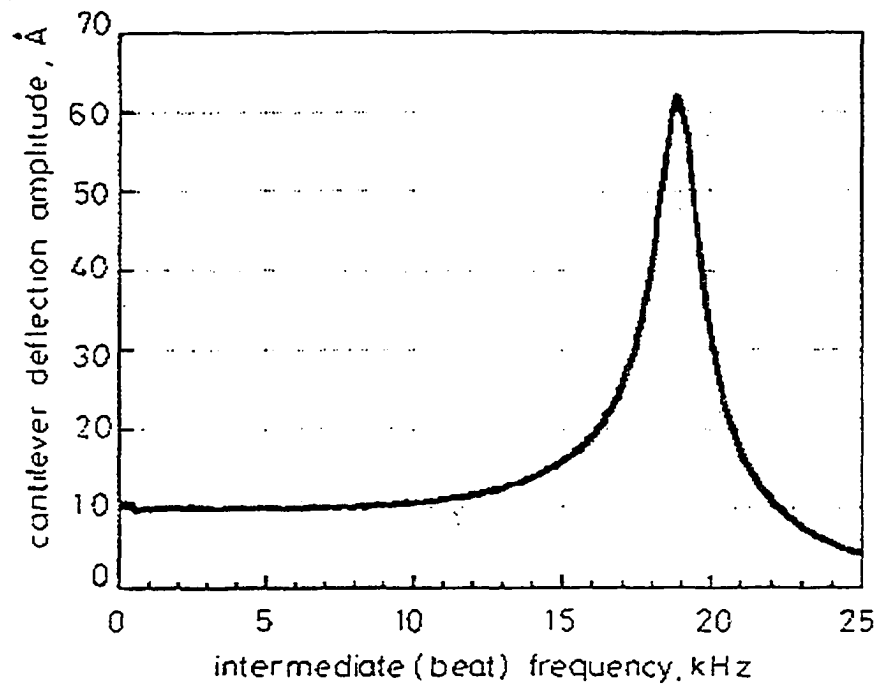
Figure 1.11: SFM electrical mixing at 1 GHz.
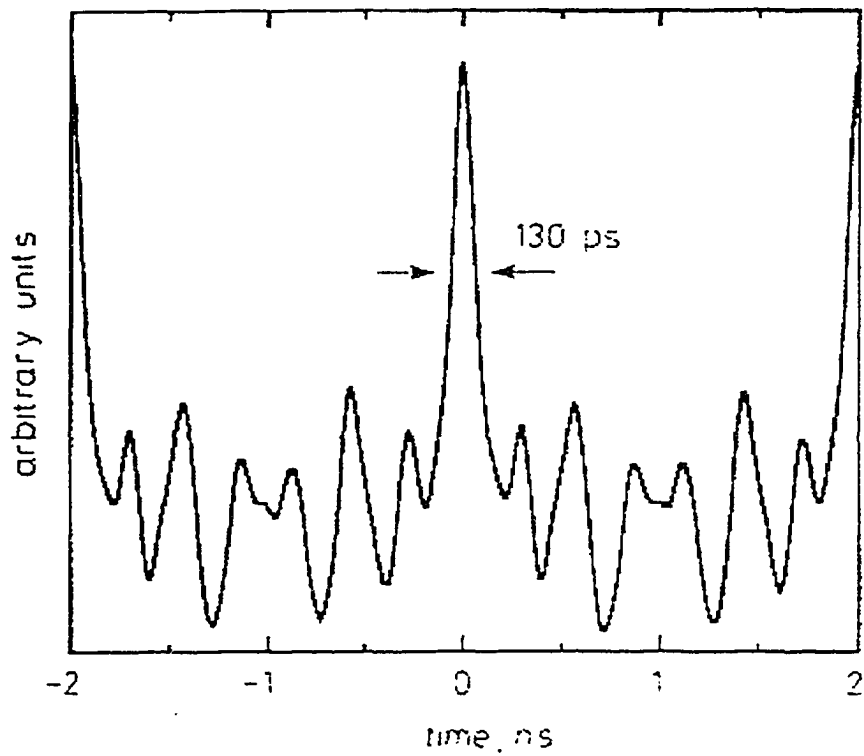
Figure 1.12: Equivalent-time correlation trace of two 110 ps pulse trains

24

In their concluding remarks, the authors contend that this technique should be capable of measuring voltage signals with picosecond time resolution and submicron lateral resolution. This technique should be quite useful especially when excitation and probe pulses are close enough in frequency that the mechanical cantilever will respond with sufficient amplitude to be detected. One questions the ultimate resolution of this technique as it relies on a tip sample force which is capacitive in origin, yet the technique should provide the submicron resolution the authors suppose.

The absolute magnitude of the mixed signal is a convolution of the force exerted on the cantilever, due to the voltage pulses being measured, and the mechanical response of the cantilever. This complication was later addressed using a nulling method developed by Bridges, Said and Thompson [37] in their time-resolved AFM system. In the work by Bridges et al. the electrostatic force between a flexible tip and sample is monitored and used to demodulate an ultrafast signal. The sample under investigation is repetitively pumped and probed and by cleverly modulating the amplitude of the repetitive probe signal while adding a variable AC dither the sample response can be accurately mapped, irrespective of the cantilever displacement. The force between cantilever tip and sample can be written as:

$$F_Z = -\frac{1}{2}\frac{\partial}{\partial z}C(x,y,z)\left[v_p(t) - v_c(x,y,t)\right]^2 \qquad (1.22)$$

where v_c is the voltage on the circuit element being tested, v_p is the voltage on the scanned probe, and $C(x,y,z)$ is dependent on the probe tip/circuit geometry and position. To measure v_c one could use a series of probe pulses similar to the technique of Hou et al., calibrating the response of the cantilever would still be a problem though. The trick that Bridges, Said and Thompson used was to use a modulated pulse train to probe the circuit voltage. The initial sampling voltage train was given as $v_s(t) = G_\delta(t - \tau)$ (where $G_\delta(t - \tau)$ is a step function at time τ with width δ) but this was modified, giving $v_p(t) = [A + K\cos(\omega_r t)]v_s(t)$ where w_r is the resonant frequency of the cantilever. In the previous equation the variables A, K and

25

$v_s(t)$ are all user controlled parameters. Using $v_p(t)$ in equation 1.22, gives a number of terms in the force equation. Most of these terms will appear as DC contributions but there will be a term at the modulation frequency ω_r, which a lock-in amplifier can detect. This term is expressed as:

$$F_z|_{\omega \simeq \omega_r} = -\frac{\partial}{\partial z}C(x,y,z) \times [A\langle v_s(t), v_s(t)\rangle - \langle v_s(t), v_c(x,y,t)\rangle] K\cos(\omega_r t) \quad (1.23)$$

where $\langle a,b\rangle = \frac{1}{T}\int_T a(t)b(t)dt$ is the inner product over the period T. Using $v_s(t)$ in equation 1.23 and evaluating the inner product $\langle v_s(t), v_s(t)\rangle$ noting that δ is the width of the impulse $G_\delta(t-\tau)$, we rewrite F_z as:

$$F_z|_{\omega \simeq \omega_r} = -\frac{\partial}{\partial z}C(x,y,z) \times \left[A \cdot \frac{\delta}{T} - \langle G_\delta(t-\tau), v_c(x,y,t)\rangle\right] K\cos(\omega_r t) \quad (1.24)$$

Under the condition that the width of the impulse approaches zero, we note that $\langle G_\delta(t-\tau), v_c(x,y,t)\rangle \Rightarrow v_c(x,y,t=\tau) \cdot \frac{\delta}{T}$. Recalling that $v_c(x,y,t)$ is the function we are trying to determine, we see that by adjusting the modulating parameter A to null the force F_z, one can easily determine v_c. This approach only works when the response of the detection system is very slow compared to the speed of the sampling pulses.

The work by Hou, Ho and Bloom was quite illustrative for early proposals for time-resolving STM operation, especially the junction mixing techniques. In the Bloom work, a pump/probe configuration was used, where pump and probe signals were mixed in the squared voltage nonlinearity exerting a force on the AFM tip. The technique of Greg Bridges et al., employed this same nonlinearity, but by using a single excitation source for pump and probe pulses, the electronics required were greatly simplified. The nulling procedure overcomes the problems of calibrating cantilever response and allows the determination of the response of a sample to electrical excitation. These techniques offer fast time resolution, demonstrated into the picosecond range, but the spatial resolution of this technique will be limited by the range of

26

the geometrical capacitance between tip and sample. For time-resolved microscopies where atomic scale spatial resolution is necessary one must look past other scanning probe microscopes to the grandfather of the field, the STM.

1.2.3 Time-Resolved Scanning Tunneling Microscopy

1993 was a banner year for experiments demonstrating the time-resolved operation of the scanning tunneling microscope. Four papers, published over a two month span by three different groups, brought three competing methods to add ultrafast time resolution to STM operation. These papers were published virtually simultaneously, but they will be introduced chronologically for consistency.

The first of the four introduced the technique of photo-gated or PG-STM [38]. In PG-STM an optical pulse train was split into a pump/probe configuration, the pump beam repetitively stimulated the sample under investigation while the probe beam was directed to an optical switch embedded in series with the tip of the STM. Because the switch has a finite "dark" resistance of $30 M\Omega$ (small compared to a typical STM tunnel junction resistance of $100 M\Omega$ or more) the STM can still operate without illuminating the switch. The idea with this configuration is to use the pump beam to stimulate the sample such that the tunneling current between tip and sample will be modified when the sample is being pumped. Without the probe beam the additional current will be small, the electronics of the STM will integrate this additional current contribution and the feedback system of the STM will compensate by adjusting the STM tip height. When the probe is implemented, the current contribution from coincidence between pump excitation and probe gating will be enhanced. Under these circumstances, the STM electronics will again integrate the excess current and the STM feedback electronics will adjust the tip height accordingly. To avoid this, the pump and probe beams are optically chopped at different frequencies, where the chopped frequencies are outside the response time of the feedback system, but within

27
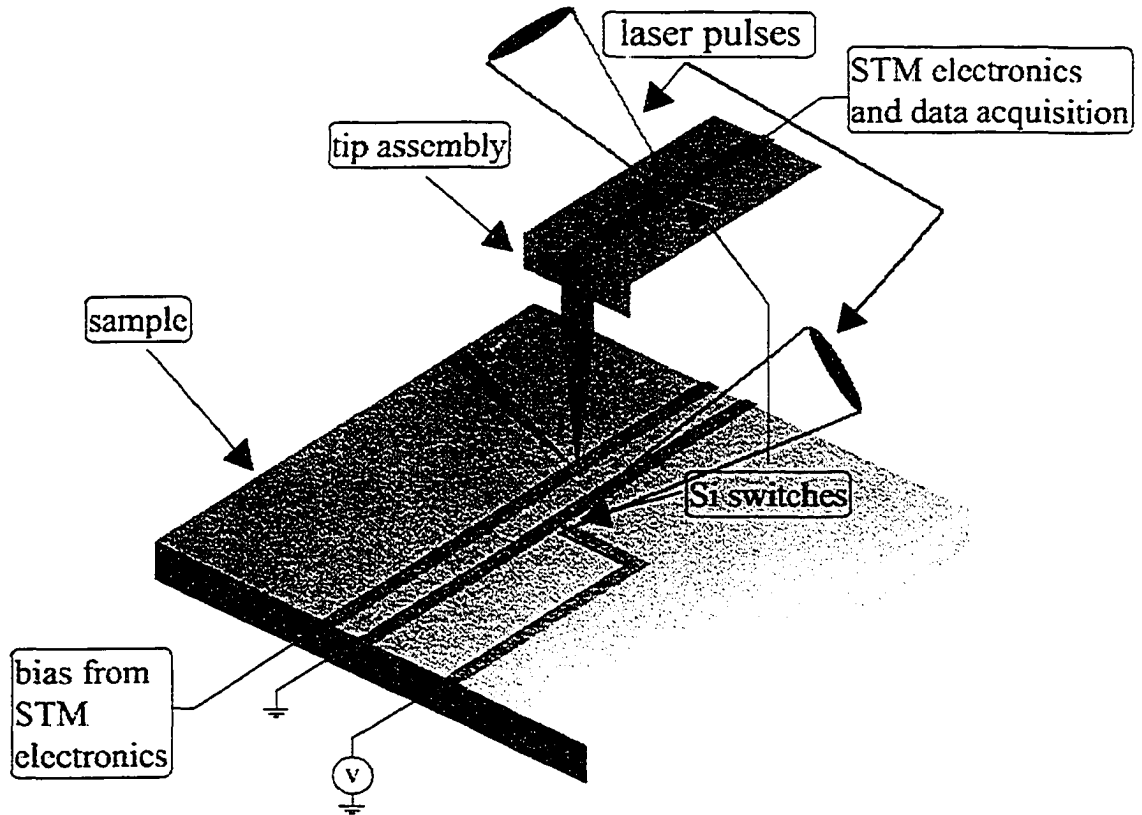
Figure 1.13: Ultrafast STM. One laser pulse excites a voltage pulse on a transmission line. The second pulse photoconductively samples the tunneling current on the tip assembly.

the bandwidth of the STM current pre-amp. A lock-in amplifier is used to detect the excess current at the chopping sum or difference frequency (beating). By shifting the phase between pump and probe pulse trains, a cross-correlation between the response of the sample (to the pump pulse), and the response of the photo-conducting switch (to the probe pulse), can be created. If one characterizes the response of the photo-conductive switch, the response of the sample can be extracted by deconvolution. The experimental setup used by Weiss et al. is shown in Figure 1.13. The cross-correlated current measured by this device is shown in Figures 1.14 and 1.15. In Figure 1.14 each trace is at a different tunneling resistance. Figure 1.15 shows the time-resolved current measured through tunneling and across a tip in contact with the transmission line. In their results Weiss et al. noted that the time resolved signal is proportional

28
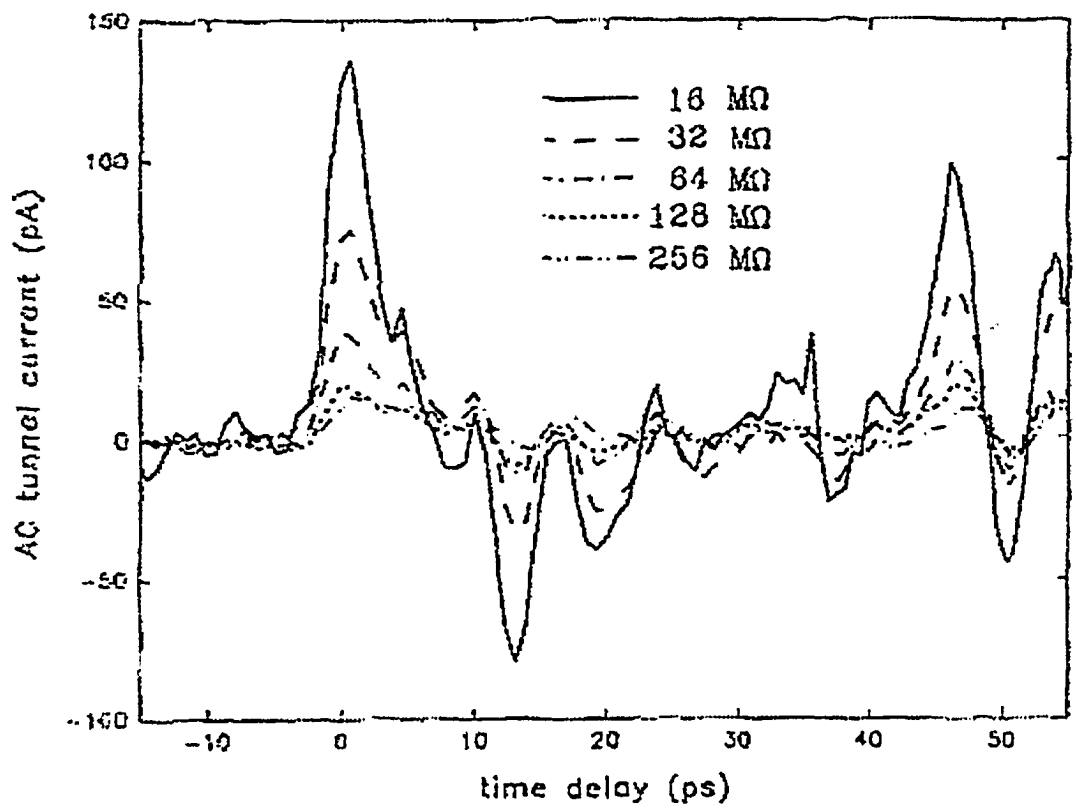
Figure 1.14: The tunneling current $\Delta I(\Delta t)$ for different gap resistances (16, 32, 128, and 256 MΩ from top to bottom).

29

-10 0 10 20 30 40 50

$I_{tunnel}(t)$ (nA)

5.3
5.2
5.1
5.0

(a)

$I_{crashed}(t)$ (nA)

95
90
85
80
75

(b)

$\partial I_{crashed}/\partial t$

4
3
2
1
0
-1
-2

(c)

-10 0 10 20 30 40 50

time delay (ps)
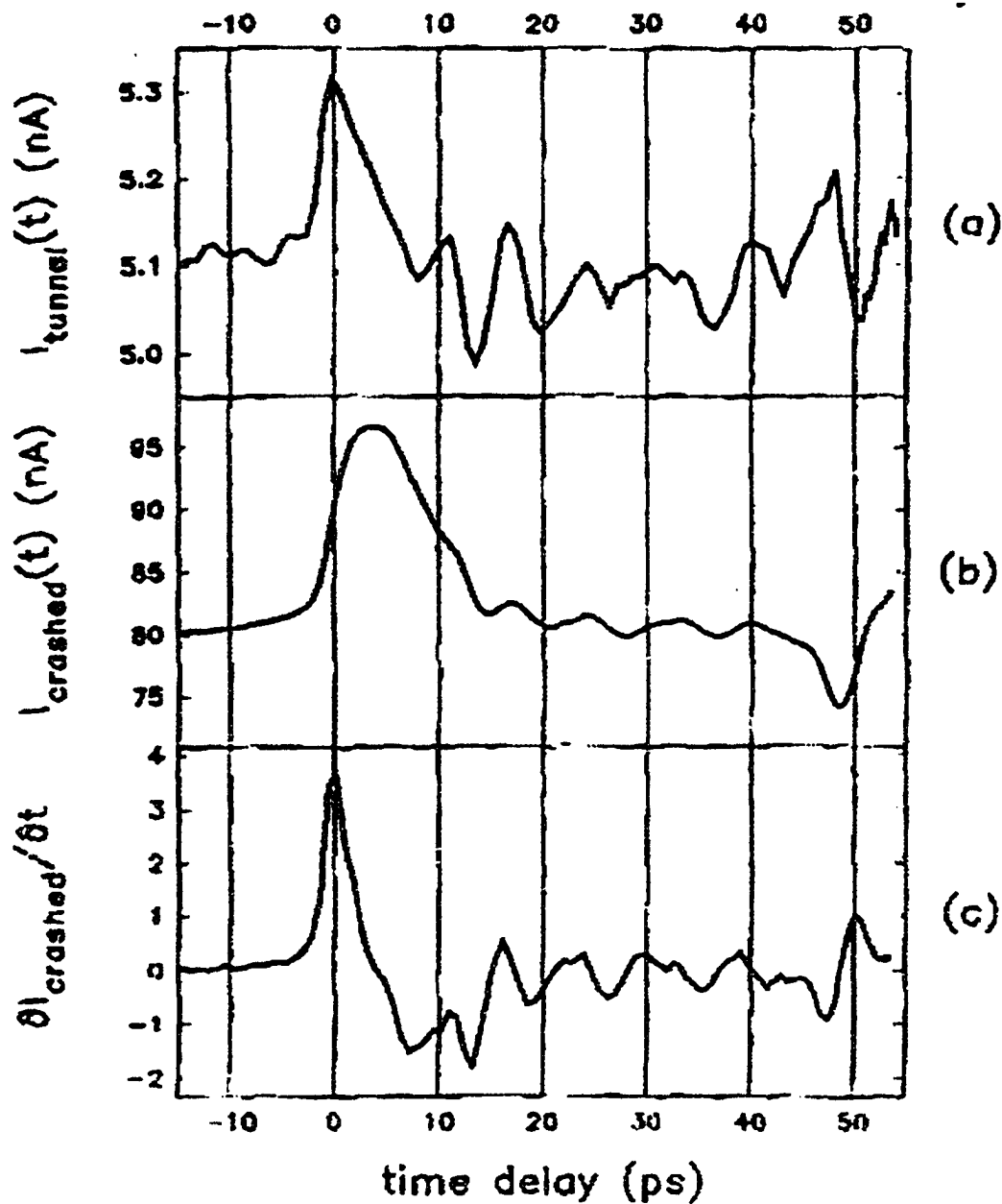
Figure 1.15: Time-resolved current cross-correlation detected on the tip assembly, (a) in tunneling (5 nA and 80 mV settings), (b) when the tip is crashed into the sample, and (c) is the time derivative of (b).

30

to the average tunnel currents, from which they concluded that there is no geometrical capacitive contribution to the time resolved signal. By extracting the tunneling tip 50 Å from the surface, the DC and time-resolved currents drop to zero. The authors used this evidence to conclude that the PG-STM technique has spatial resolution of at least 50 Å. This conclusion is not valid. Even in ordinary STM I/Z sensitivity and lateral resolution are essentially unrelated. Another interesting observation was that the time-resolved correlation pulse width increases with increasing gap resistance. This the authors attribute to an *RC* time for the tunnel junction, where *R* is the gap resistance and *C* is a quantum capacitance between tip and sample. In the conclusion of this publication the authors included a (0.7 × 0.7 μm^2) topographic scan of their transmission line. They contest that this spatial scan represents a frame in a time-resolved movie; this is not the case as contrast in the image contains no time-dependence.

The Weiss et al. interpretation of these experiments was not satisfying. One perplexing question was the role of tip/sample geometrical capacitance. According to Weiss et al., a quantum tip/sample capacitance ($\approx 10^{-18}F$) played a significant role in the shape of the time-resolved current. This was supported by the evidence that the shape of the time-resolved signal changes dramatically if the STM tip is crashed into the sample (transmission line) as shown in Figure 1.15. The time resolved signal in contact looked like the integral of the tunneling signal. If a quantum capacitance were the only source of the time resolved signal then the geometrical tip/sample capacitance, in parallel with the quantum capacitance and 3 orders of magnitude bigger was not having any contribution.

The true nature of capacitance in PG-STM was not resolved until 1996 by Groeneveld and van Kempen [39]. In their paper, "The capacitive origin of the picosecond electrical transients detected by a photoconductively gated scanning tunneling mi-

31

croscope" the authors established that PG-STM was a capacitive microscope limited to μm scale spatial resolution. In the Groeneveld and van Kempen model, a simple circuit model is used where the tunnel junction is represented by a linear conductance γ in parallel with the geometrical capacitance C_t. This tunnel junction is in series with the photoconductive switch with time dependent conductance $g_s(t)$ in parallel with the switch capacitance C_s. This configuration is shown in Figure 1.16. The time dependent switch conductance and bias voltage $V_{in}(t)$ are periodic with period T (10 ns), an essential feature since RC times of the tip/sample (eg. 10 Mω $\times$ 1 fF=10ns) are comparable to the period. From this model the time-dependent tip voltage on the tip of the STM (before the switch) is given by:

$$C_p \frac{dV}{dt} + [g_s(t) + \gamma] V = C_t \frac{dV_{in}(t)}{dt} + \gamma V_{in}(t), \tag{1.25}$$

where $C_p = C_s + C_t$. Integrating the product of V(t) with g_s(t) over the period T we get the averaged current:

$$I_c = \frac{1}{T} \int_0^T g_s(\tau) V(\tau) d\tau. \tag{1.26}$$

If the STM tip is withdrawn from the sample surface and γ drops to zero, then the integrated current becomes zero since no net current can flow through a capacitor. This explains one of the strange results of the Weiss publication. Solving equations 1.25 and 1.26 for an STM tip tunneling and in contact with a transmission line also fits the Weiss et al. result as shown in Figure 1.17.

The excellent agreement between the Groeneveld and van Kempen model and the Weiss et al. results confirmed that the PG-STM technique would not maintain STM spatial resolution in its application. PG-STM used the electronics of a scanning tunneling microscope to detect a time-resolved signal which was capacitive in origin. The ultimate spatial resolution of PG-STM is limited by the spatial extent of the geometrical capacitance of the tip, on the order of μm's. Another technique must be employed if ultra-fast temporal and atomic spatial resolution are demanded.
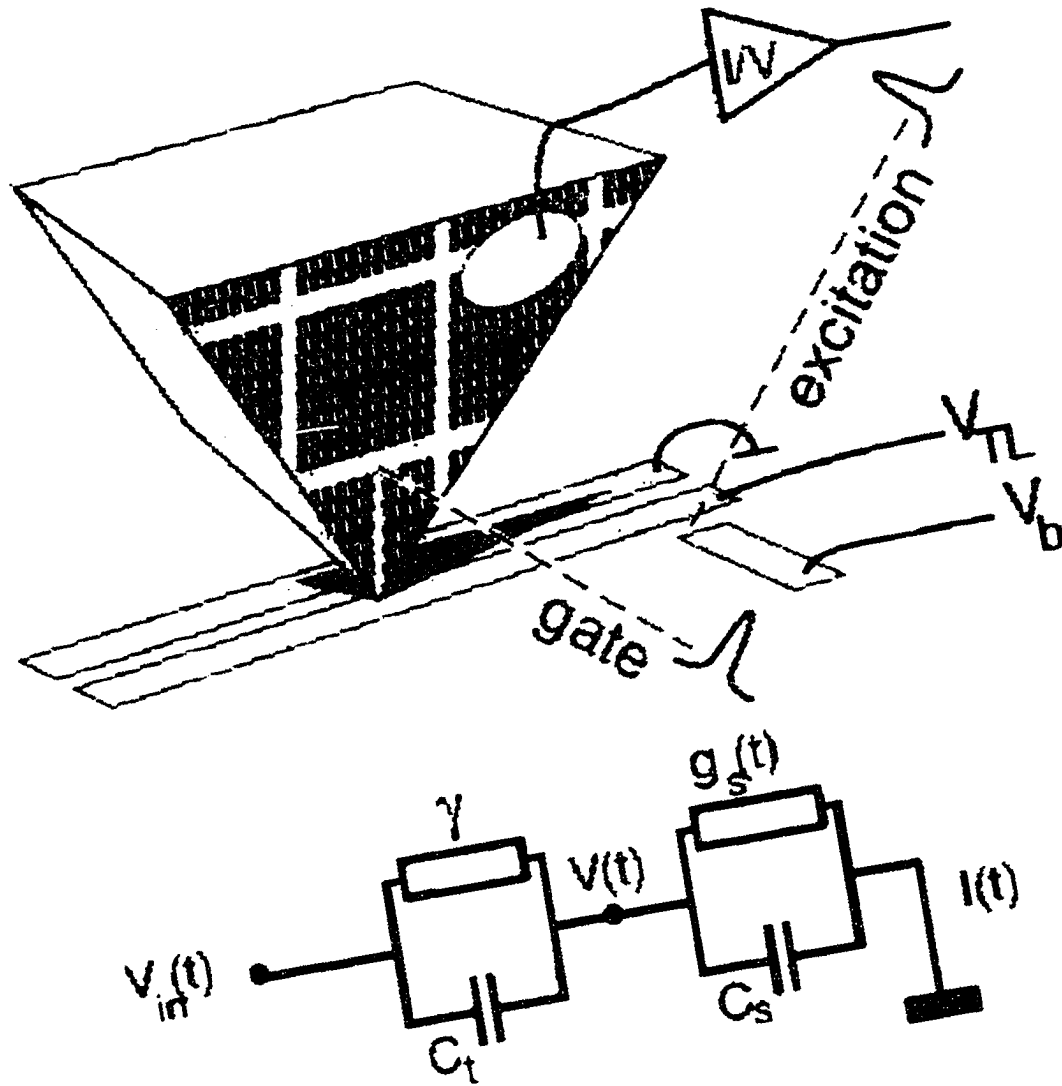
Figure 1.16: Photoconductively gated STM tip above a coplanar stripline and its equivalent circuit model shown below.

33
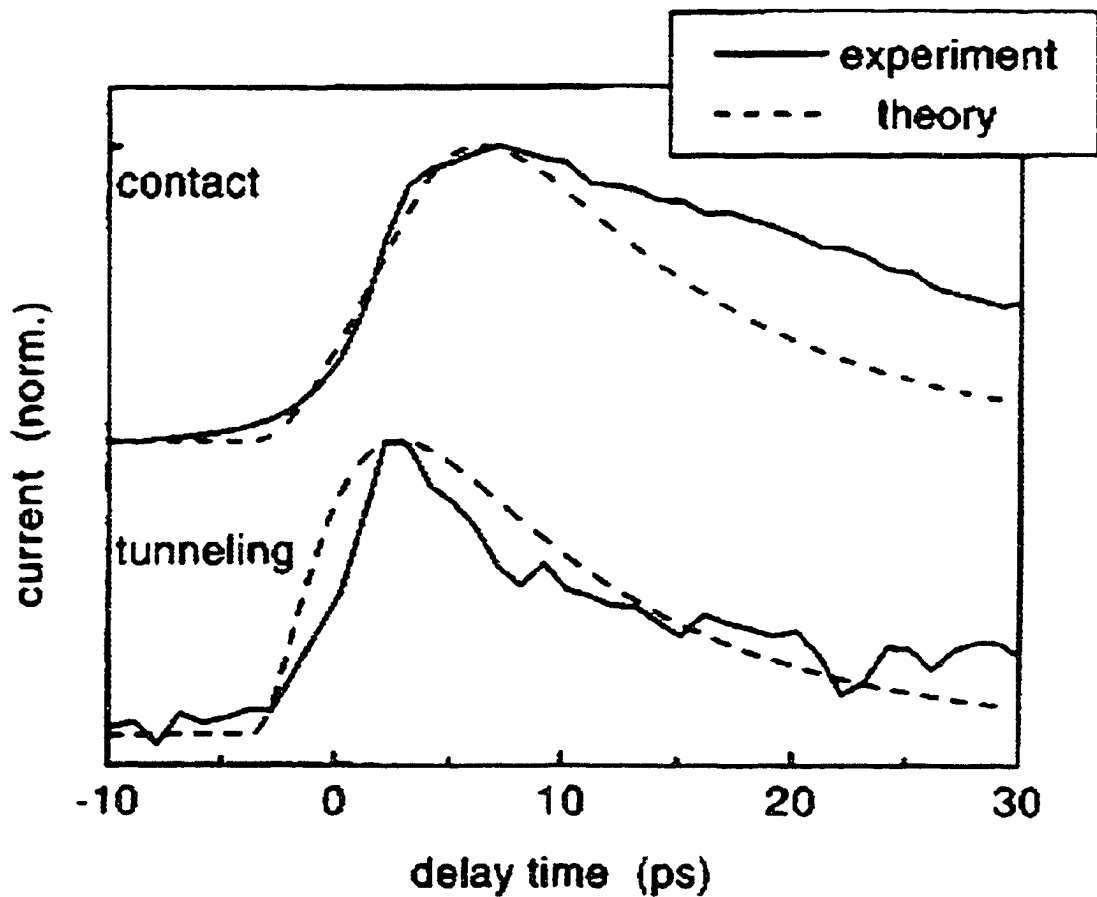
Figure 1.17: Comparison between the measured (solid curve) and calculated (dashed curve) correlation current for different tunnel conductance γ. In contact $\gamma = 10^{-2}\Omega^{-1}$ and tunneling $\gamma = 1.4 \times 10^{-8}\Omega^{-1}$, each curve has been independently scaled.

34

One week after the results of the photo-gated STM technique were published (also in Appl. Phys. Lett.), Freeman and Nunes [40] reported a completely different technique for time-resolving an STM, the distance modulation technique. In this work a sample is repetitively stimulated while the distance between tip and sample is varied on a nanosecond time scale. Recall that STM tunneling current varies exponentially with tip/sample separation. Varying this separation on a short time scale allows the gating (or fast sampling) of a signal. This is a technique to mechanically switch the tunneling conductance of the STM without the inherent capacitance problems associated with having an electrical switch on the STM tip. The experimental setup is shown in Figure 1.18 where the STM tip was electro-chemically etched nickel wire (125 μm diameter). Nickel is magnetostrictive, changing its structure by constricting or elongating with applied magnetic field. A pulsed magnetic field can cause an acoustic pulse to be launched along the magnetostrictive nickel tip, modulating STM tip/sample separation on nanosecond time scales. When biased to the steepest part of its magnetization curve the maximum reversible magnetostriction was $\approx$ 0.1 ppm/Oe. Using a static bias field of 30 Oe and applying a 80 ns, 20 Oe pulse resulted in a maximum absolute tip displacement of 5 Å (measured through time-resolved fiber-optic interferometry). The direction of tip deflection can be changed by reversing the polarity of the field pulse. For the experiment described, the effective tunneling work function $\overline{\phi}$=0.45 eV gives a characteristic tunneling range $(2k')^{-1}$=1.45Åwhich is less than the 5Å displacement of the tip, indicating that the acoustic pulse will have a very significant effect on the tunneling current signal over its duration.

Using the distance modulation technique to sample an electrical pulse sent down a gold transmission line, as shown in Figure 1.18 gives the curves shown below in Figure 1.19 [6]. The fact that the Time-Resolved signal reversed polarity as the pulse field polarity was reversed illustrated the fact that the time-resolved current contribution

---

[6]Note that the figure reference of Fig. 2 has not been included in this work – Fig. 2, shows an I/Z curve and the Tip Extension time profile for the nickel tip

35
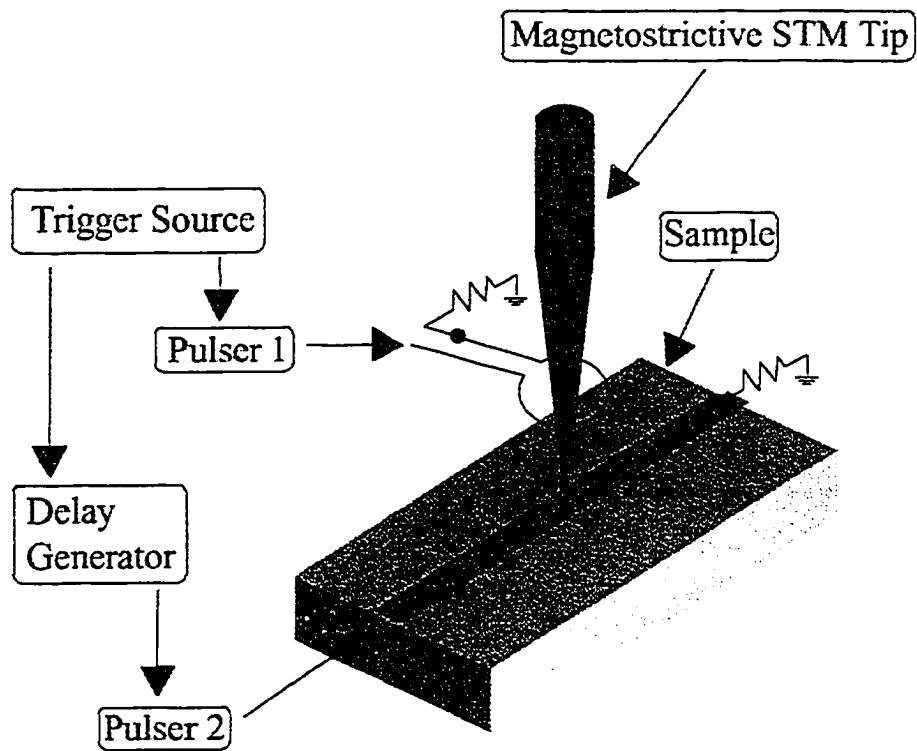
Figure 1.18: A schematic diagram of the apparatus which illustrates how the tip is threaded through a local magnetic field coil and the arrangement of the pulsers. Pulser 1 delivers current pulses to the field coil, and pulser 2 applies voltage pulses to the gold stripline sample. The resistive $(50\ \Omega)$ terminations eliminate electronic reflections.

36
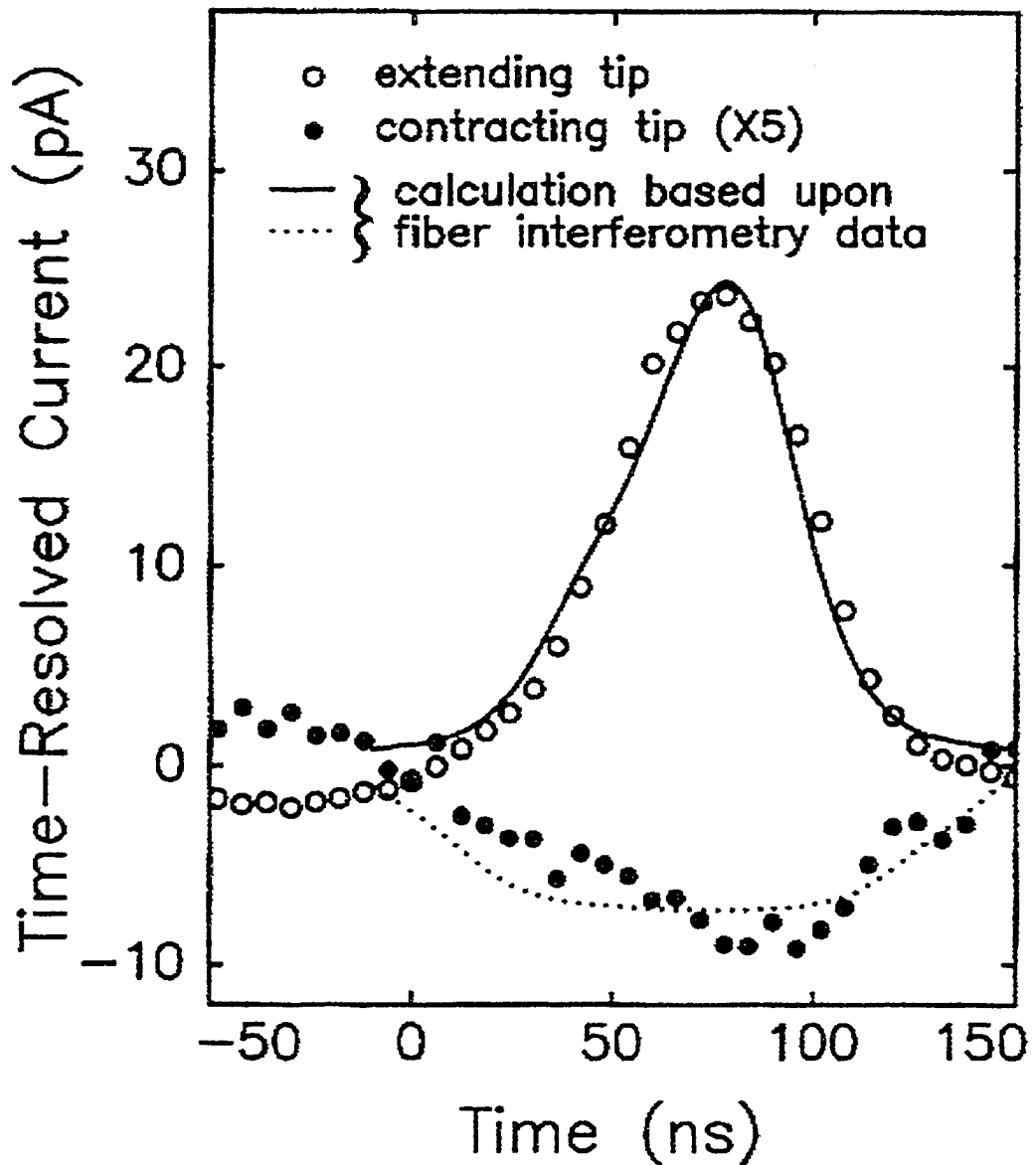
Figure 1.19: Measured time-resolved tunneling current obtained using the tunnel distance modulation technique to sample the presence of a voltage pulse on the transmission line sample. Data are shown for both directions of current flow through the magnetic field pulse coil, and are compared with a model calculation based on the data of Fig. 2 of Ref [40]. Note that the vertical scale for the lower curve has been expanded by a factor of 5. DC tunneling parameters used to stabilize the quiescent tip position are 1 nA, 50 mV.

37

decreases as the tip is withdrawn. It does not represent a negative current, just a lowering of current relative to the average since the y-axis zero corresponds to a DC current of 1 nA. This apparent bipolar signal is evidence that tip magnetostriction is responsible for the time-resolved current observed. This technique is quite general in its applications. It poses few restrictions on the type of samples which can be studied. So long as the samples can be stimulated repetitively in a way that the STM can detect, distance modulated STM can be used. The primary hindrance of the technique is the inertia of the tip (limiting distance modulated STM to the nanosecond time domain). A technique with "no moving parts" would enable superior time-resolution. Motivated by this criterion the junction mixing technique was developed.

Details of the junction mixing (JM) STM technique were published less than two weeks after the PG-STM paper [41] (3 time-resolved STM publications in 11 days!). This approach looks remarkably similar to PG-STM but its differences are very significant. In junction mixing the non-linearity of the STM tunnel junction is used to demodulate ultra-fast excitations, as was proposed in the 1989 anonymous disclosure [32]. In this technique a sample is repetitively stimulated (or pumped) where this stimulus will, in some way, affect the tunneling current of the STM. The effect could be to change the tunneling I/V characteristic, through some local surface modification, or to change the bias voltage within the original I/V characteristic. I/V characteristics for metal insulator metal tunneling are typically given by a form of the Simmons equation [42]:

$$I = \beta(V + \gamma V^3) + O(V^5), \tag{1.27}$$

showing a cubic non-linearity. The probe pulse, in the junction mixing technique is launched either from the tip or the sample towards the tunnel junction, mixing with the pump pulse at the junction itself. This leads to a time-resolved current contribution which varies with the time delay between pump and probe pulses as they arrive at the tunnel junction. This was demonstrated by Nunes and Freeman

38
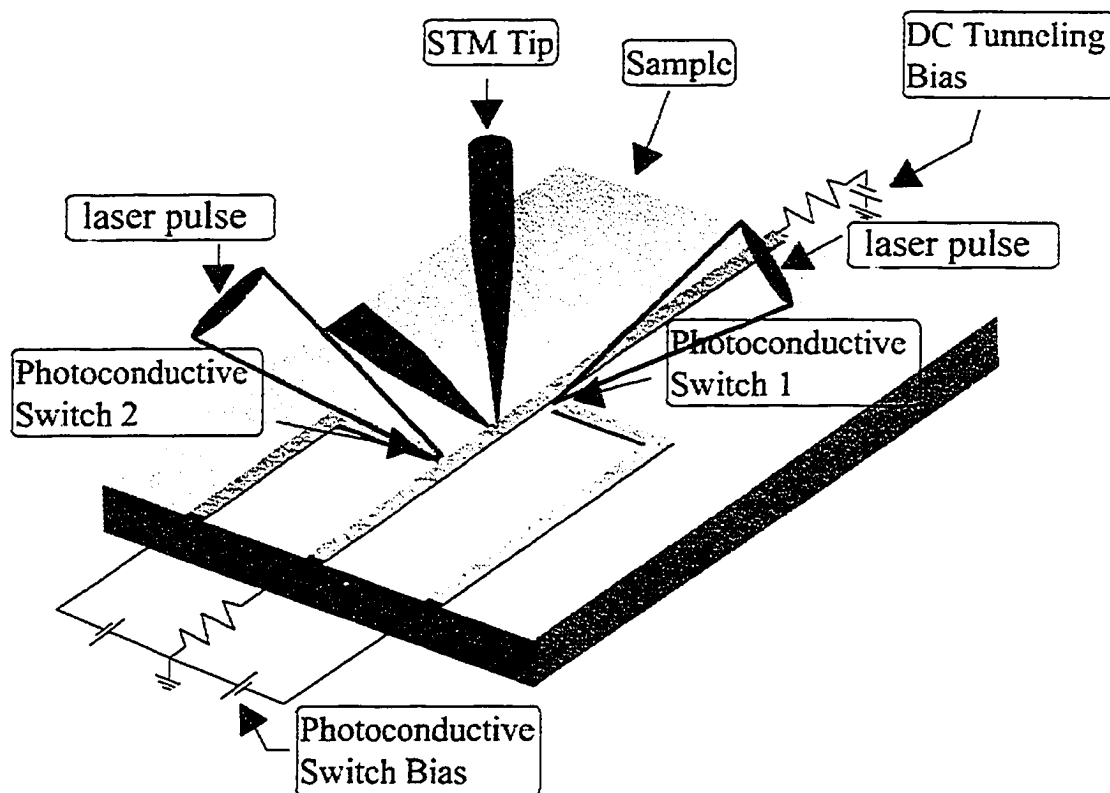
Figure 1.20: Experimental layout for JM-STM.

in their Science paper. The experimental setup is shown in Figure 1.20. In order to distinguish the time-resolved current contribution, an optical chopper was used to chop pump and probe beams at different frequencies and a lock-in amplifier was used to detect at the sum frequency. As a proof of principle experiment, photoconductively generated optical pulses were sent down a transmission line, with one pulse acting as pump and one as probe. A variable delay between pump and probe was the result of an optical delay line. When these electrical pulses arrived simultaneously at the tunnel junction of the STM, the sum voltage leads to a non-linear increase in tunneling current which can be seen in Figure 1.21. Because the mixing between pump and probe pulse is occurring in the tunnel junction, this technique should

39
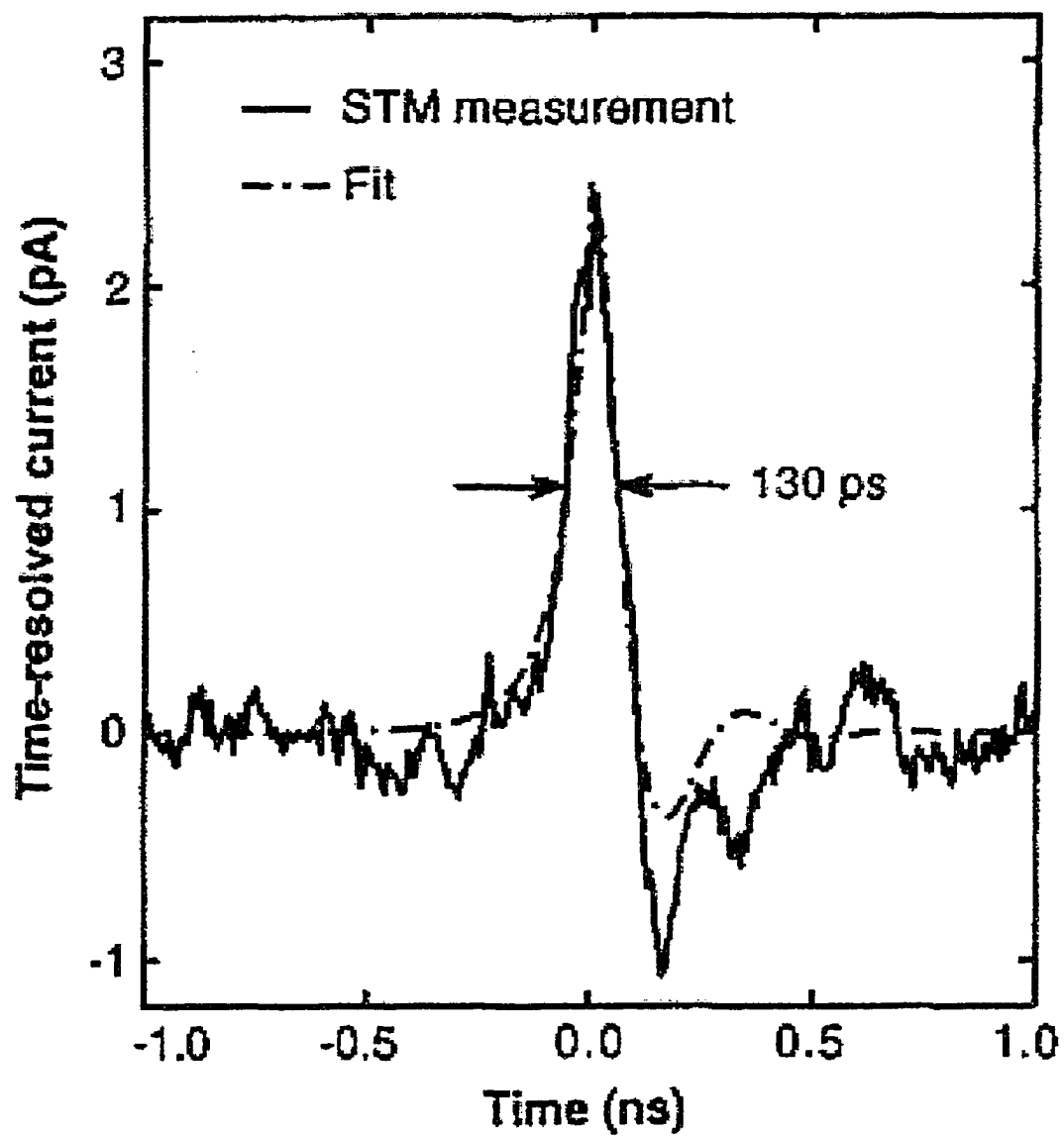
Figure 1.21: JM-STM time-resolved current.

40

maintain the spatial resolution of STM. This method is non-contact and essentially non-perturbative, considering that the current leaking from the circuit under test is on the order of pA. There are limitations to the junction mixing technique; for the signal to "mix" in the tunnel junction the stimulated sample must offer I/V contrast with the unstimulated sample. This might not be the case if the stimulated sample undergoes a structural phase change which one wants to resolve, for example. This technique offers considerable speed advantages over the distance modulation technique and should be comparable to PG-STM in terms of speed while outstripping PG-STM with atomic spatial resolution. Since the time-resolved signal in JM-STM is produced at the STM tunnel junction there is no reason to suspect that the spatial resolution of this technique will not be identical to that of an ordinary STM (the same should be true of the distance modulation technique).

The last of the pioneering TR-STM papers was published on December 27, 1993, two months later than the previously reported experiments. This work by Takeuchi and Kasahara [43] seems to have been developed independently of any of the other previous works. It seems clear the authors only became aware of the work of Hou et al. and Weiss et al. during the course of publication. Regardless, they developed a photo-gated STM technique and used it to show better than 300 ps time resolution. The photo-gated technique of Takeuchi and Kasahara also falls victim to the analysis of Groeneveld and van Kempen as a capacitive microscopy without STM spatial resolution. The experimental setup is shown in Figure 1.22.

The sample (a gold transmission line) is stimulated by the pulsed output of a Schottky barrier diode, driven by a 100 MHz synthesized sinusoid. A Pt/Ir STM tip is attached to a photo-conductive switch of Au/Mo patterned onto a semi-insulating InP substrate. The dark resistance of the switch is around 1 MΩ, less than a typical tunneling resistance, so the STM can operate with the photoconductive switch closed. By illuminating the switch with 80 ps pulses (400 μW (average power) at 670nm) at

41
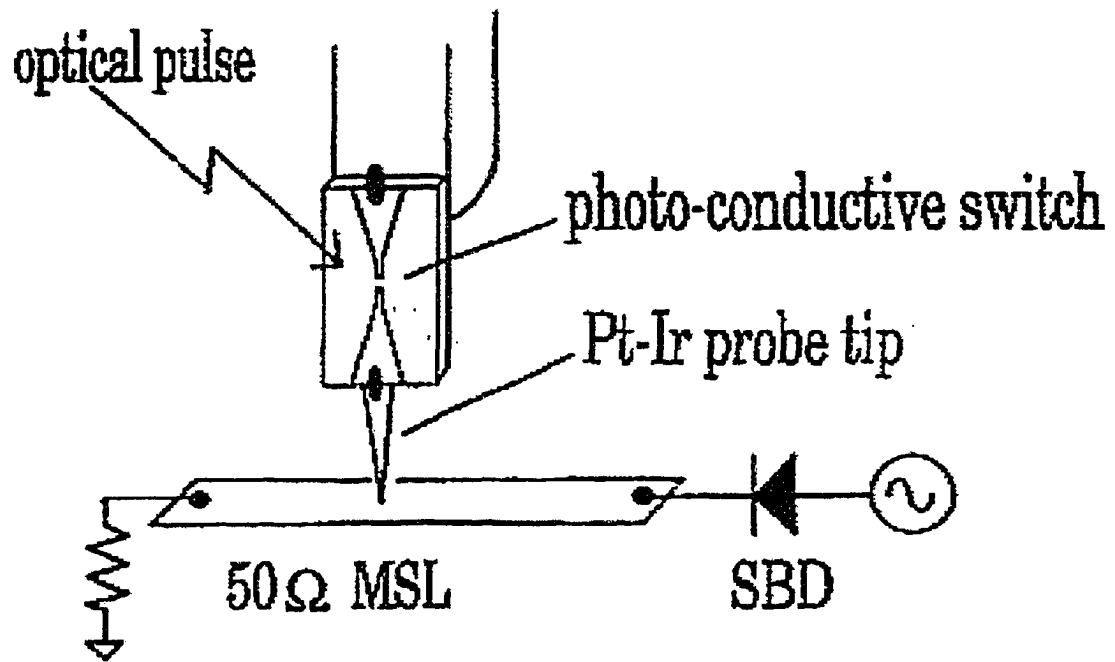
Figure 1.22: Schematic of probe tip and sample device, SBD is Schottky barrier diode and MSL is metal stripline.

a 100 MHz + 1 kHz repetition rate from a driven laser diode, additional current from the STM can be gated into the STM electronics, through the 1 kΩ open resistance of the InP switch. The pump frequency of the sample was set to be 100 MHz, so that the probe beam would sweep across the period of the stimulated sample in 100,000 cycles. This brought the dynamics of the sample within the bandwidth of the STM electronics, as shown in Figure 1.23. Implementation of this technique relies on an electrical synthesizer to pump the sample and gate the STM tip current using a photo-conductive switch stimulated by a driven laser diode. The speed of the synthesizer will limit the time resolution of this technique. It would be advantageous to instead rely on all optical methods for generating electrical pulses needed to stimulate the sample under investigation. This technique is essentially a modification of the Weiss et al. photo-gated STM technique as a photo-conductive switch mounted on the STM tip is used to gate the STM tunneling current. This implies that the Takeuchi, Kasahara method for time-resolving an STM will not maintain STM spatial resolution.

42
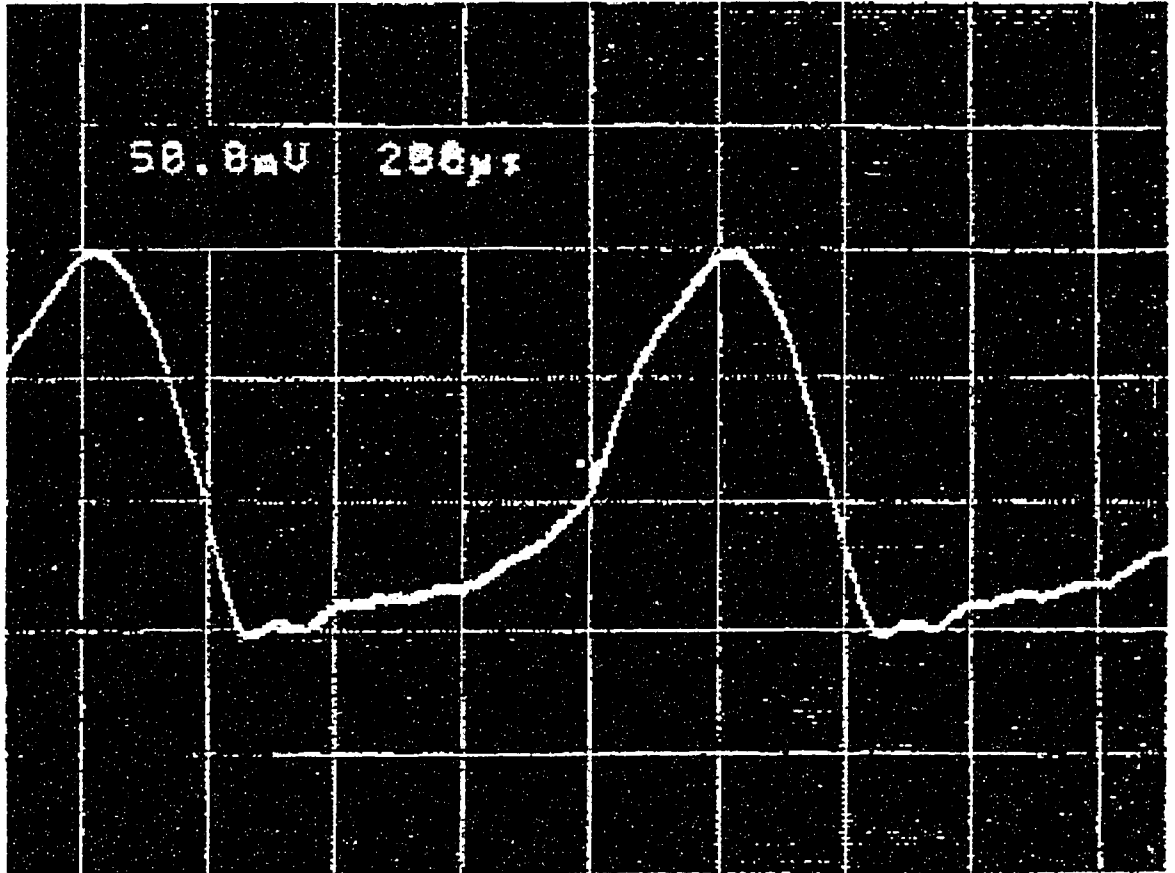
Figure 1.23: Output of the Schottky barrier diode as measured using a high-speed oscilloscope.

43

This concludes the introduction to STM and to early developmental work on time-resolved scanning probe microscopy. STM is capable of imaging surface topography and sample local density of states with atomic spatial resolution. Through current-distance and current-voltage spectroscopies the STM is capable of characterizing additional material properties. Conventional STM images are essentially static, as STM control electronics are limited to kHz bandwidths. In order to time-resolve the operations of a scanning tunneling microscope various pump/probe schemes were explored.

The three most prominent of these are photo-gated STM, distance modulated STM and junction-mixing STM. Photo-gated STM has been demonstrated to have 2 ps temporal resolution and 50 Å vertical resolution limited only by the apparatus used in these early experiments. Photo-gated STM does not achieve STM spatial resolution, as shown by Groeneveld and van Kempen [39]. Distance modulated STM has been shown to have nanosecond time resolution as well as Å vertical resolution. The mechanical response of the magnetostrictive tip should ultimately limit the time resolution of this technique. There is no reason to suspect that the distance modulation technique will not achieve the same atomic spatial resolution as an ordinary STM. Junction mixing STM, like photo-gated STM was shown to have picosecond time resolution (130 ps) and Å vertical resolution. Since the junction mixing technique mixes pump and probe excitations at the tunnel junction of the STM this technique should also maintain atomic spatial resolution.

The junction mixing technique presented above is the most promising technique for adding ultrafast time resolution to the STM. A JM-STM is an electrical demodulation technique without moving parts, expected to outperform the method of distance modulation. In junction mixing, the tunnel junction of the STM should give rise to the time-resolved signal. No spatial resolution should be lost, as in the capacitively coupled signal measured using PG-STM. Though JM-STM seems the best candidate

44

for time-resolved STM further experiments were required to prove it.

References

[1] G. Binnig and H. Rohrer. *Helv. Phys. Acta.*, 55:726, 1982.

[2] G. Binnig and H. Rohrer. *Rev. Mod. Phys.*, 56:615, 1987.

[3] G. Binnig and H. Rohrer. *Surface Science*, 126:236, 1983.

[4] G. Binnig and H. Rohrer. *Scientific American*, August:3, 1985.

[5] G. Binnig and H. Rohrer. *IBM J. Res. Develop.*, 30:355, 1986.

[6] G. Binnig, C. F. Quate, and Ch. Gerber. *Phys. Rev. Lett.*, 56:930, 1986.

[7] A. Selloni, P. Carnevali, E. Tosatti, and C. D. Chen. *Phys. Rev. B*, 31:2602, 1985.

[8] J. A. Stroscio, R. M. Feenstra, and A. P. Fein. *Phys. Rev. Lett.*, 57:2579, 1986.

[9] J. A. Stroscio, R. M. Feenstra, and A. P. Fein. *J. Vac. Sci. Technol.*, A5:838, 1987.

[10] R. M. Feenstra, J. A. Stroscio, and A. P. Fein. *Surface Science*, 181:295, 1987.

[11] G. Binnig, H. Rohrer, Ch. Gerber, and E. Weibel. *Phys. Rev. Lett.*, 50:120, 1983.

[12] R. A. Wolkow and Ph. Avouris. *Phys. Rev. Lett.*, 60:1049, 1988.

[13] Zheng Gai, Yi He, Hongbin Yu, and W. S. Yang. *Phys. Rev. B*, 53:1042, 1996.

[14] H. F. Hess, R. B. Robinson, R. C. Dynes, J. M. Valles, Jr., and J. V. Waszczak. *Phys. Rev. Lett.*, 62:214, 1989.

[15] S. H. Pan, E. W. Hudson, K. M. Lang, H. Eisaki, S. Uchida, and J. C. Davis. *Nature*, 403:746, 2000.

[16] E. Ruska. *Z. Phys.*, 87:580, 1934.

[17] A. Prebus and J. Hillier. *Can. J. Res.*, A17:49, 1939.

[18] D. M. Eigler and E. K. Schweizer. *Nature*, 344:524, 1990.

[19] R. H. Fowler and L. Nordheim. *Proc. R. Soc. London*, A119:173, 1928.

[20] J. Curie and P. Curie. *Comptes Rendus*, 91:383, 1880.

[21] C. Julian Chen. *Introduction to Scanning Tunneling Microscopy*. Oxford, New York, 1993.

[22] K. Takayanagi, Y. Tanishiro, S. Takahashi, and M. Takahashi. *Surface Sci.*, 164:367, 1985.

[23] J. J. Boland. *Surf. Sci.*, 244:1, 1991.

[24] G. Binnig, H. Rohrer, Ch. Gerber, and E. Weibel. *Appl. Phys. Lett*, 40:178, 1982.

[25] J. Tersoff and D. R. Hamann. *Phys. Rev. Lett.*, 50:1998, 1983.

[26] J. Tersoff and D. R. Hamann. *Phys. Rev. B*, 31:805, 1985.

[27] J. Bardeen. *Phys. Rev.*, 49:653, 1936.

[28] D. M. Eigler, P. S. Weiss, E. K. Schweizer, and N. D. Lang. *Phys. Rev. Lett.*, 66:1189, 1991.

[29] I. Tamm. *Phys. Z. Sowjetunion*, 1:733, 1932.

[30] J. A. Appelbaum and D. R. Hamann. *Rev. Mod. Phys.*, 48:479, 1976.

[31] H. A. Mizes, Sang il Park, and W. A. Harrison. *Phys. Rev. B*, 36:4491, 1987.

[32] anonymous. *Research Disclosure*, August:# 30480, 1989.

[33] R. J. Hamers and David G. Cahill. *Appl. Phys. Lett.*, 57:2031, 1990.

[34] R. J. Hamers and David G. Cahill. *J. Vac. Sci. Technol. B*, 9(2):514, 1991.

[35] R. Hamers and K. Markert. *Phys. Rev. Lett.*, 64:1051, 1990.

[36] A. S. Hou, F. Ho, and D. M. Bloom. *Electron. Lett.*, 28:2302, 1992.

[37] G. E. Bridges, R. A. Said, and D. J. Thompson. *Electron. Lett.*, 29:1448, 1993.

[38] S. Weiss, D. F. Ogletree, D. Botkin, M. Salmeron, and D. S. Chemla. *Appl. Phys. Lett.*, 63:2567, 1993.

[39] R.H.M. Groeneveld and H. van Kempen. *Appl. Phys. Lett.*, 69:2294, 1996.

[40] M. R. Freeman and Geoff Nunes, Jr. *Appl. Phys. Lett.*, 63:2633, 1993.

[41] Geoff Nunes, Jr. and M. R. Freeman. *Science*, 262:1029, 1993.

[42] J. G. Simmons. *J. Appl. Phys.*, 34:238, 1963.

[43] K. Takeuchi and Y. Kasahara. *Appl. Phys. Lett.*, 63:3548, 1993.

Chapter 2

Advances in picosecond scanning tunneling microscopy via junction mixing

2.1 Context

In early 1996 four groups were attempting to demonstrate time-resolved STM experiments. Using photo-gated STM there was the group of Weiss et al. [1] and the Groeneveld, van Kempen et al. group [2]. Both Freeman and Nunes, having demonstrated the distance modulation technique [3], were inclined to abandon it in pursuit of the faster electrical junction mixing alternative [4]. For the work developed in this thesis the photo-gated STM technique was not pursued as it was clear the effect of tip/sample capacitance should dominate the time-resolved signal. In the junction mixing technique there is no where for charge to accumulate so it was suspected that junction mixing would be immune to capacitive artifacts.

The work presented here was stimulated by the desire to improve and develop the junction mixing technique into a proven method for acquiring ultrafast time-resolution with an STM while maintaining STM spatial resolution. Initial experiments were designed to repeat and improve on the experiments of Nunes and Freeman [4]. The first experiment set out to tunnel into a transmission line structure while launching two electrical pulses towards the STM tunnel junction. The pulses would be launched

48

from photo-conductive "Auston" switches [5]. By using an ion implanted GaAs substrate similar to ones studied by Elezzabi et al. [6], time-resolution could be improved over earlier work. Looking for a time-resolved signal both in tunneling range and out of tunneling range was another test designed to show that the time-resolved signal was not merely capacitive in origin.

Another significant aspect of the proposed experiment was that pulses could be launched from the same side or the opposite sides of the STM tip. In previous junction mixing experiments both pulses were launched towards the tip from the same direction. This did not rule out the possibility that a non-linear interaction could mix the pulses before they reached the tunnel junction, effectively eliminating any spatial dependence on the time-resolved signal. By launching electrical pulses from opposite sides of the transmission line towards the tip, no pulse interactions are possible before the pulses reach the tunnel junction implying that any non-linear mixing must occur at the tunnel junction.

2.2 Experimental Details

Details of the equipment necessary to perform time-resolved STM experiments will now be disclosed. A working room temperature STM had been constructed by David Fortin [7] and it provided enough optical access that time-resolved experiments could be considered. The microscope consisted of a nano-scope STM head shell, which incorporated the STM tip mounted on a piezo tube which had been sectioned into 4 outer quadrants and an inner surface.

The piezo tubes used were from Staveley Sensors Inc.[1]. The material was EBL#2(PZT-5A) coated with gold or nickel electrodes. The piezoelectric coefficients [2] of this material are:

---

[1]contact Paul Stokes (860)291-2537
[2]the ratio of the strain component over a component of applied electric field

49

d_{31} Å/V @ 293 K = -1.73

d_{31} Å/V @ 4.2 K = -0.31

Young's modulus 10^{10} N/m^2 = 6.3

Mechanical Q = 100

For a voltage applied to the inner conductor: $\frac{\Delta L}{V} = \frac{d_{31}L}{t}$ and for equal and opposite voltages applied to opposite outer quadrants: $\frac{\Delta L}{V} = \frac{0.9d_{31}L^2}{d_m t}$ where $d_m = \frac{OD+ID}{2}$ is the mean diameter of the tube, L is the length of the tube and $t = \frac{OD-ID}{2}$ is the wall thickness of the tube. Typical scan tubes have an OD=0.250", t=0.020" and L=1.000" giving a lateral displacement of 34 nm/V and a longitudinal displacement of 8.7 nm/V (at room temperature). To make electrical contact to the piezo electrodes use Indium Flux #3 and Indium solder #2. Use a soldering iron at 450 F, do not overheat the piezo as it will de-pole(to re-pole a piezo follow the procedure of Russell Petrucci from Staveley Sensors outlined on page 235 in Ref. [8]). At room temperature it is easy to calibrate a piezo tube using the Fabry Perot interferometer, but at low temperatures this is not always easy or possible. In this case, C. Julian Chen devised a method for in situ piezo calibration(pages 229-233 in Ref. [8]).

The head-shell was mounted vertically, resting on 3 support screws. The tunneling sample was mounted face up, between the 3 screws, such that the tip of the STM would be lowered down onto the sample. The 3 screws allowed course positioning of the STM tip and one screw could also be rotated using a stepper motor, allowing one side of the head-shell to be raised or lowered about 800 nm per half step of the motor. As the head-shell was being tilted the STM tip moved in increments of only 8 nm per half step(due to mechanical reduction caused by mounting the STM tip close to the tilting axis of the head-shell). The STM tip assembly is shown in Fig 2.1. The whole assembly, including head-shell and mounting support was itself mounted on two heavy metal plates suspended by springs as shown in Fig 2.2. Eddy current damping was also employed to dampen oscillations of the mounting plates the STM rests on. The

50
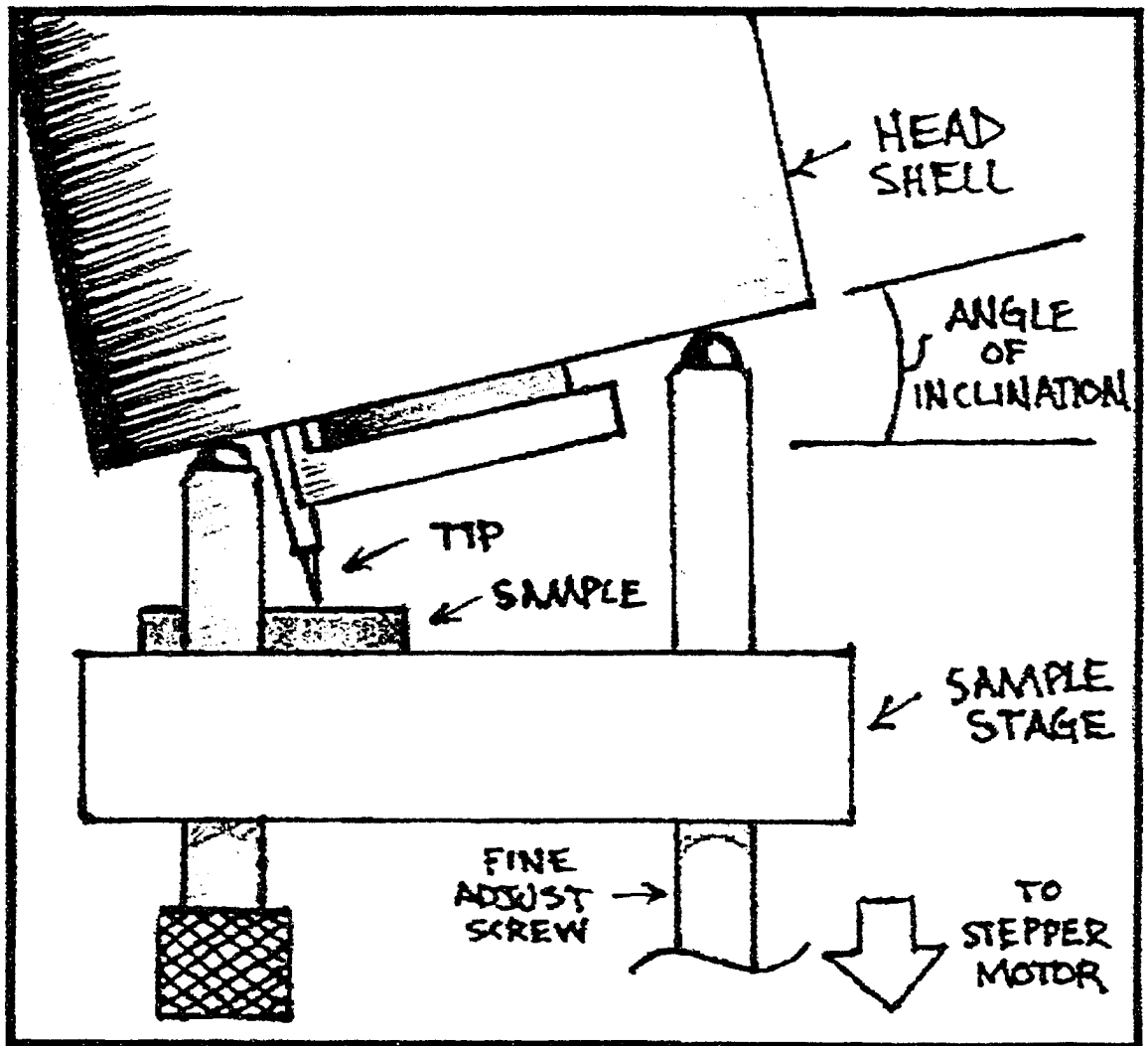
Figure 2.1: STM head-shell, tip and support screws.(Hand drawn by David Fortin)

51
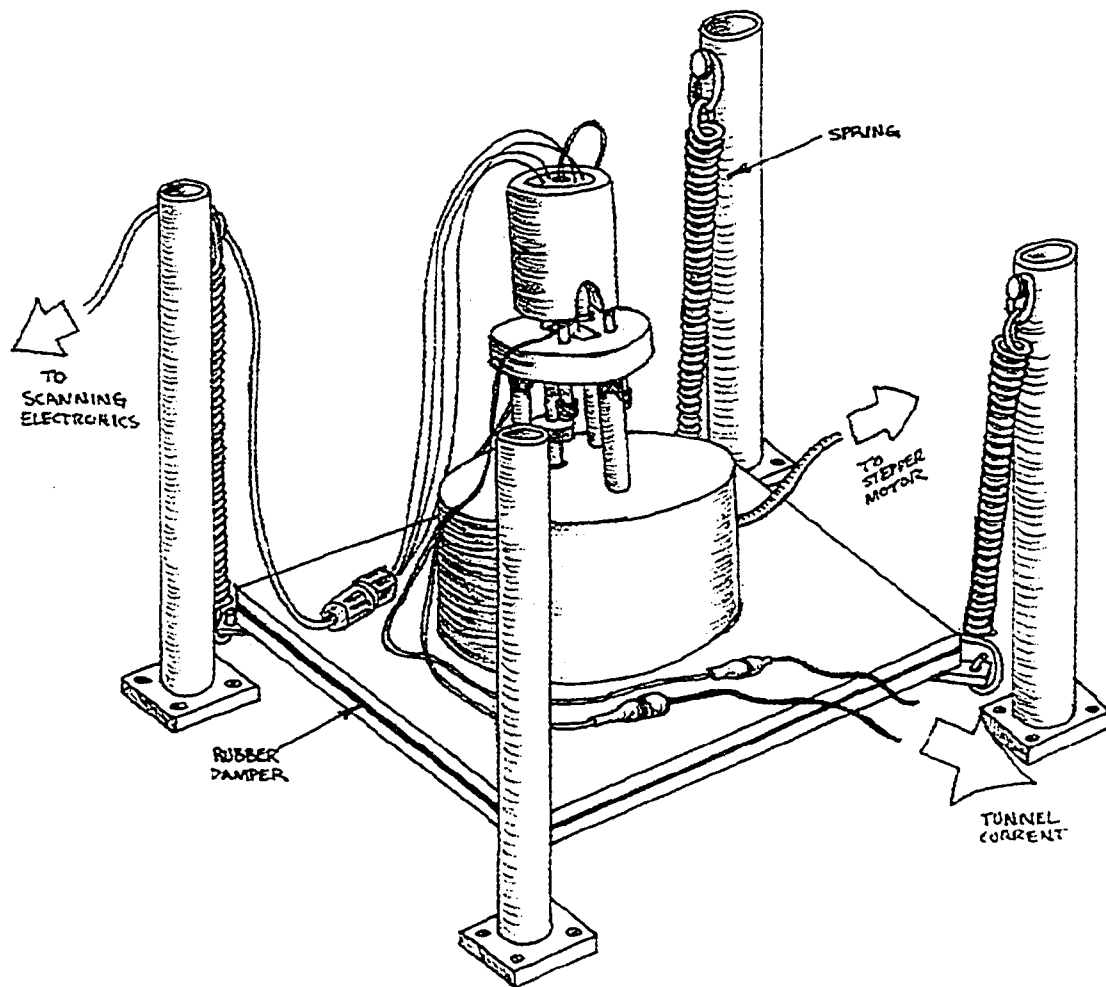
Figure 2.2: Illustration of the STM showing all mechanical components.(Hand drawn by David Fortin)

52

microscope was placed in a metal enclosure with Sonex acoustic damping foam panels lining its interior[3]. The enclosure was mounted on a pneumatically supported optics table in order to minimize seismic vibrations. The principle behind this vibration isolation system is to eliminate all but the lowest frequencies reaching the working part of the STM(the tunnel junction). The head-shell of the STM and the sample mount are designed with high resonance frequencies so that low frequency oscillations will drive the tip and sample together minimizing their relative motion.

The STM electronics were composed of an Ithaco 1211 current pre-amp, an IBM CSS-D1760 analogue feedback controller and bias current supply and an IBM CSS-F4812 high voltage amplifier. The current pre-amp, bias voltage and piezo's are hooked up to the electronics as shown in Fig. 2.3. For the 0.5 nA tunneling current set point, the Ithaco pre-amp should be set on a gain of 10^8 V/A and the IBM feedback controller set point should be 4.24. Feedback time constants of 1×1000 were typical as was a bias voltage of 50 mV. With this equipment it is also possible to perform I/V and I/Z scans but it is necessary to connect a co-ax at 5 V to two locations on the CSS-D1760. The first location is the Feedback/-Hold input on the feedback control section of the CSS-D1760. The second location is the Bias/-Ramp input on the bias voltage section of the CSS-D1760. When an I/V or I/Z scan is initiated this 5 V line must go low, to 0 V to suspend the feedback mechanism. This 5 V line also controls the bias voltage, switching one of the bias outputs(2nd BNC from the right) from an internal source to a ramp source(3rd BNC from the right) for I/V scans. If one is performing I/Z scans it is important that the bias voltage is connected to the right most BNC, to avoid any fluctuations in bias voltage.

The junction mixing STM technique relies on repetitive stimulation of the tunnel junction by pump and probe excitations. These excitations can come from electrical sources such as current pulsers, but for excitations in the picosecond to femtosecond

---

[3]contact Illbruck inc. (517)548-6700

53
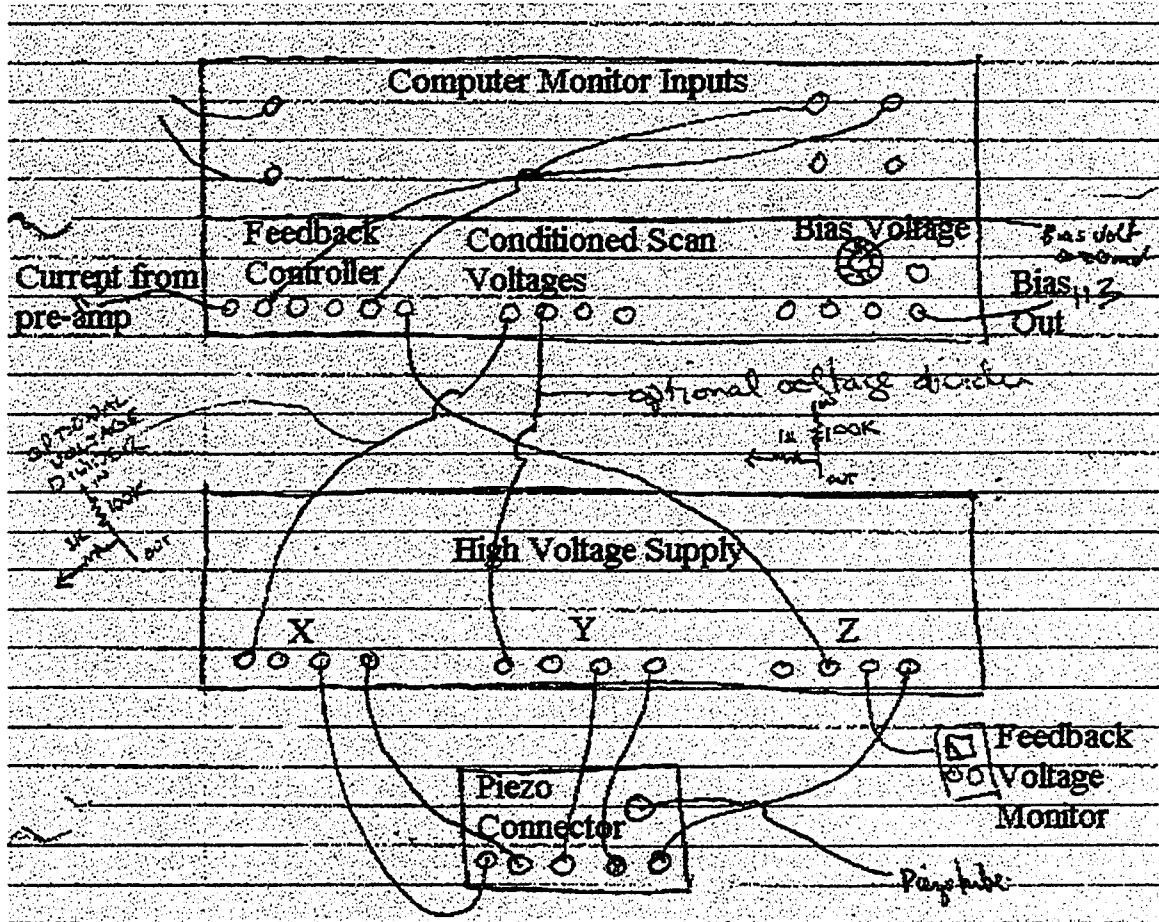
Figure 2.3: Connection diagram for the IBM feedback electronics and HV supply.

54

time scales, pulsed laser systems are typically used. At the time of these experiments the laser system available was an Nd doped YAG system pumping a dye laser, producing 2.8 ps pulses at 610 nm. The dye beam was split in order to create pump and probe beams. The pump beam was focused into a single mode fiber in order to bring the pulses into the STM chamber(metal enclosure with Sonex lined interior). The probe beam was first sent through an optical delay line after which it was directed into another fiber and into the STM chamber. Dispersion was not significant for these pulses as 2.8 ps resolution was attained with this setup in a later experiment.

The initial junction mixing experiments which were published and appear later in this chapter were electrical mixing experiments. In these experiments, two electrical pulses were optically generated and traveled down a transmission line to the tunnel junction of the STM(the STM was tunneling into the transmission line). In order to create these electrical pulses suitable transmission line structures had to be created through optical lithography. A mask was created and used to pattern a gold transmission line structure onto an ion implanted GaAs substrate. The masks were generated using LEDIT and printed on transparencies by Screaming Colour Press[4](at 3600 dpi resolution). Semi-insulating GaAs wafers(current supplier - Sumitomo Canada Limited[5]), polished on one side were sent to IICO Customized Wafer Services[6] for ion implantation. They were implanted at various doses(H^+ implanted at 200 keV, 7° tilt, and implant doses 0.5, 1.63, 2.75, 3.88 and 5 $\times 10^{15} cm^{-2}$). The implant is done to produce recombination centers in the material [9]. These recombination centers add additional energy states within the GaAs band gap allowing a faster carrier/hole recombination than would normally occur in unimplanted GaAs(for really fast recombinations, use low temperature grown GaAs). Ion implants age quickly! Over the course of months carrier recombination times grow much longer(from a few ps

---

[4]phone (780)486-3300
[5]phone (416)860-3846
[6]phone (408)727-2547, note: last time they broke 2 of our substrates and did not compensate us

55

to 10's and 100's of ps). To reduce aging store in a cold place like a liquid nitrogen dewar). Once the GaAs had been ion implanted, it was cleaned in an HCl dip and then a 200 Å layer of chromium and a 1000 Å layer of gold were sputtered onto its surface. Photoresist was spun onto the gold surface and then cured. After this we used the UV lithography facility on the 6th floor to expose the resist. The exposed resist was dissolved away and the sample was placed in both gold and then chromium etchants. Once the GaAs substrate had been prepared it was cleaved into samples. Each sample was mounted on a copper coated PC board. The copper provided a ground for the transmission line structure. Contacts were made on the PC board and wire bonds were made between the gold transmission lines and the external contacts. BNC connectors were connected to the PC board contact pads to connect the sample to external electronics. The characteristic impedance of this stripline transmission line structure was calculated to be 68 Ω from page 326 of "Transmission lines for digital and communication networks" [10].

2.2.1 Anomalous Signal

During the course of these experiments we encountered one unexpected result which might be worth following up on. On one occasion a time-resolved signal was repeatably detected after moving the tip out of the tunneling regime shown in Figure 2.4. The experimental setup for the time-resolved experiment is shown in Figure 2.5 with the STM tip out of tunneling range at position (B) as shown in Figure 2.5. It was suggested that the non-contact signal was radiative in origin, coming from the photo-conductive switches as they were illuminated. If this were the origin, then one would expect the radiative signal would be present at the tip regardless of the relative pump/probe timing. To detect a time-resolved signal there must be some non-linear pump/probe interaction and the location for this interaction would probably be the photo-conductive switches. Exploring this possibility we consider that a pulse is generated at switch (1) travels to switch (2) as the second optical pulse arrives and

Time Resolved Signal - in and out of tunneling range
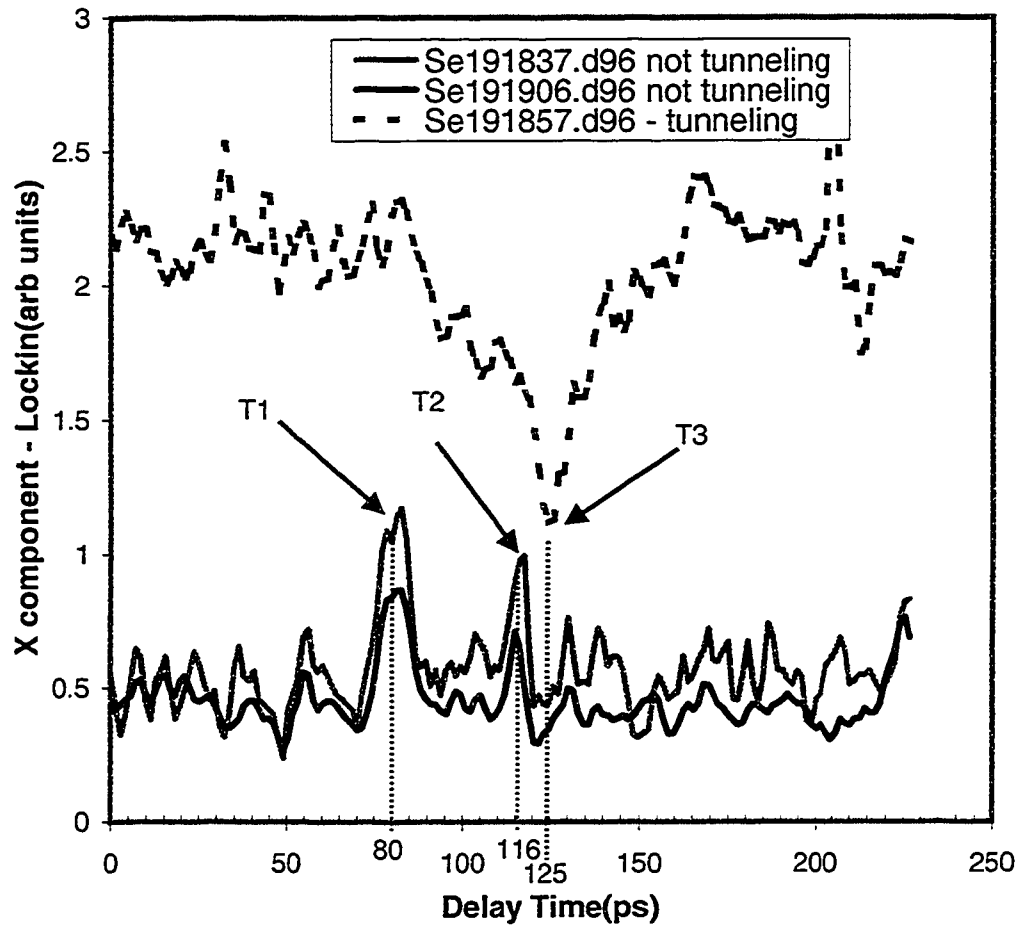
Figure 2.4: Top most trace shows the junction mixing signal, where the dip at T_3 corresponds to pump and probe pulses arriving at the tunnel junction synchronously. The lower traces show two separate instances where current transients were detected out of tunneling range. Timing arguments suggest that the transients were produced at T_1 and T_2 as each photoconductive switch was illuminated.

57

produces one peak. Similarly the other peak is generated as an optically generated electrical pulse from switch (2) arrives at switch (1). Looking at the distance between switches, 5mm and the time between peaks, 45ps gives an electrical pulse speed down the transmission line of $\frac{1}{9}$ mm/ps, which is not too far off the calculated value of $\frac{1}{8}$ ps/mm given in reference [11]. Further experiments to reproduce this signal were unsuccessful.

2.3 Publication

Scientific and technical interest in the dynamics of microscopic structures continues to drive the development of ultrafast scanned probe microscopies. The first reports of picosecond resolution in scanning tunneling microscopy (STM) appeared several years ago [4, 1, 3, 12]. Several alternative approaches have been pursued. In photoconductively-gated STM (PG-STM) [1, 2] a photoconductive switch, electrically in series with the STM tip, is used to create a narrow boxcar window for resolving fast signals. Very recently subpicosecond signals from the PG-STM were reported [13]; however, a new model to resolve the enigmatic role of the geometrical capacitance in these measurements suggests that these signals are capacitive in origin [14], limiting the spatial resolution of this technique to the micrometer scale. The other methods use characteristics of the tunnel junction itself to demodulate fast tunneling signals. In the most general approach, the tunneling impedance is directly modulated via the tip-sample separation, enabling gating of the tunneling signal [3, 15, 16]. This has been demonstrated on nanosecond time scales, but because of the mechanical motion involved it is more difficult to extend to the picosecond and subpicosecond regimes. In another approach the tunneling impedance is *electrically* modulated on very short time scales, thus adding short electrical pulses to the STM voltage bias. In this case, the inherent nonlinearity of the current-voltage characteristic allows the fast signals
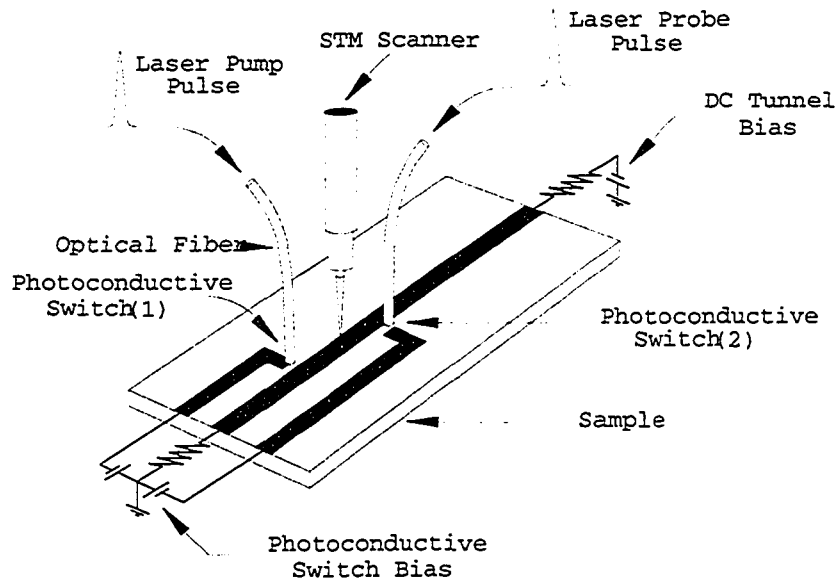
Figure 2.5: Schematic illustration of the transmission line and photoconductive switches, showing the placement of the optical fibers and the positions of the STM tip for different measurements.

to be extracted in a background-free manner [4]. This technique is referred to as junction-mixing (JM-STM). In this work we report an order of magnitude improvement in time-resolution for JM-STM, along with the first direct timing evidence which confirms that the signals originate at the tunnel junction.

The original JM-STM experiment [4] used a pair of GaAs-based photoconductive switches to launch electrical pulses onto a gold transmission line. In this early experiment, the switches were electrically connected to the line through wire bonds, and time-resolved tunneling was detected by mixing the two electrical pulses in the junction of an STM tunneling into the transmission line. The electrical pulse widths were quite long, on the order of 100 ps (determined by the carrier lifetime in the GaAs), and in addition the high-speed electrical characteristics of the structure were relatively poor. An improved structure, illustrated in Fig. 2.5, has been employed for the present work.

The 30 μm gap switches and 250 μm wide linear conductor are produced in a single lithography step from a gold film on an ion (H^+) damaged semi-insulating

59

GaAs substrate. An electrical ground plane beneath the substrate completes the transmission-line nature of the structure. To avoid electrical reflections the transmission line is terminated at both ends, using surface mount resistors equal in value to the calculated characteristic impedance of the line (68Ω).

2.8 ps duration (610 nm, 250 pJ) optical pulses are delivered to the photoconductive switches through optical fibers, at a 76 MHz repetition rate. The resulting electrical pulses are characterized by cross-correlation measurements using the two switches alone [5]. A 5 mm separation of the two switches allows clear relative timing comparisons of the correlation signals to the STM-detected signals, as well as of STM signals detected at different positions along the line. Fig. 2.6(a) illustrates the electrical cross-correlation waveform measured by launching an electrical pulse at one switch (biased at 8 V), and photoconductively sampling the current at the other switch. The sampled current as a function of probe pulse delay is shown by the solid line in the figure. To estimate the actual electrical waveform through a deconvolution, we have assumed a shape for the electrical pulse with rise time governed by the 2.8 ps optical pulse width, and fall time determined by the carrier lifetime, τ, of the semiconductor. Here τ can then be determined by a best fit to the cross-correlation signal, shown by the dashed line in Fig. 2.6(a). We neglect the additional structure, arising from small electrical reflections, on the right hand side of the correlation pulse. The resulting pulse with $\tau = 7$ ps is shown for reference at an arbitrary time position by the dotted line in the figure. This lifetime is significantly longer than the 3 ps value reported in the literature for this 200 keV H^+ implantation dose of $7 \times 10^{13} cm^{-2}$ [17]. We have confirmed that pulse dispersion is not a significant factor in the measurement; correlation signals from a similar structure having the switches in direct opposition (i.e. the 5 mm separation reduced to zero), fabricated on the same substrate, yield the same correlation width.

60
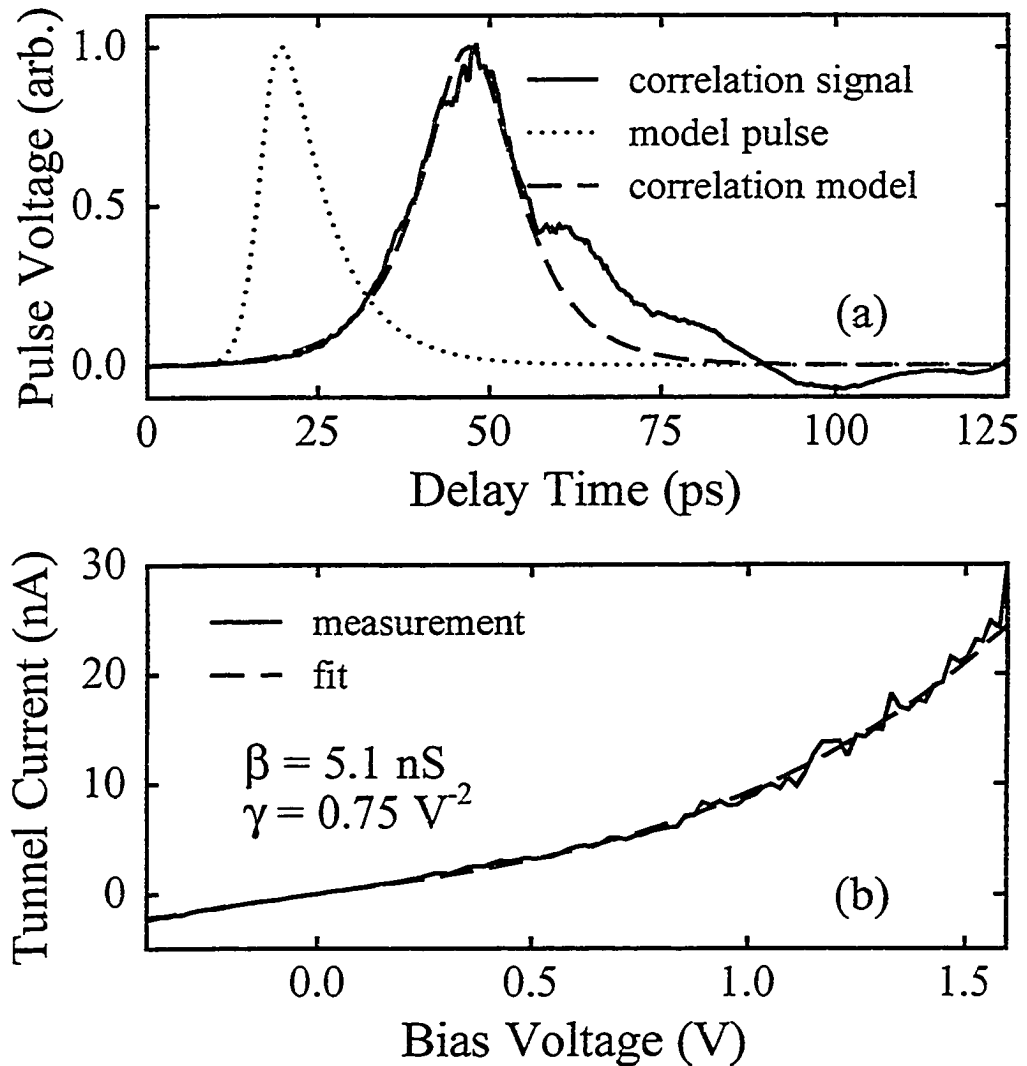
Figure 2.6: (a): Two-switch electrical cross-correlation signal, for electronic pulse characterization (solid line). The dashed line is a model signal calculated for the 2.8 ps optical pulse width and a 7 ps carrier lifetime. The corresponding deconvolved electrical pulse shape is shown by the dotted line. (b): Measured current-voltage characteristic of the STM (Pt/Ir tip, ambient operation) tunneling into the transmission line (solid line). The quiescent tunneling parameters are 50 mV bias, 0.25 nA current, before sweeping the bias voltage for this measurement. The dashed line is a fit to determine the cubic nonlinearity.

61

As the nonlinearity of the tunnel junction is exploited to separate the time-resolved signal from other currents, it is essential to have an accurate measure of the current-voltage (I-V) characteristic for quantitative interpretation of the picosecond data. A measurement of the I-V curve over the voltage range relevant to the present measurements is shown in Fig. 2.6(b). In these experiments we use Pt/Ir tips, Au lines, and tunnel under ambient conditions. The junction is stabilized at a tunnel conductance of 5 nS (50 mV bias, 0.25 nA current) prior to the measurement. The dashed line in the figure is a fit to the form $I = \beta(V + \gamma V^3)$, which describes the leading nonlinearity of the tunneling current through a metal- insulator-metal junction [18]. We find $\beta = 5.1$ nS, $\gamma = 0.75$ V^{-2} in this case, although spot measurements at different sites on the surface yield γ values varying between 0.5 and $1V^{-2}$. This nonlinearity has also been used in mixing and rectification experiments at optical and microwave frequencies [19, 20, 21].

A representative time-resolved tunneling signal is plotted in Fig. 2.7. The time axis represents the arrival time (controlled by a slow optical delay rail) of the laser pump pulse at switch 1 relative to that of the laser probe pulse at switch 2 (see Fig. 2.5.) Time zero corresponds to coincident arrival of the two optical pulses at their respective switches. Two voltage pulses actually propagate away from each switch in response to the absorption of a 2.8 ps optical pulse (one to the left, one to the right), but reflections of the pulses which initially propagate away from the STM tip have negligible effect in the present measurements. The cubic nonlinearity mixes the voltage pulses when they are coincident at the junction. The nonlinear component is the time-resolved signal, and is integrated by a conventional current amplifier (the individual transients contributing to the signal cannot be resolved; they are orders of magnitude beyond the frequency bandwidth of the current amplifier.) Lock-in detection is used to separate this component from the quiescent tunnel current. The time-resolved portion of the tunneling signal is modulated (by optically chopping the

62
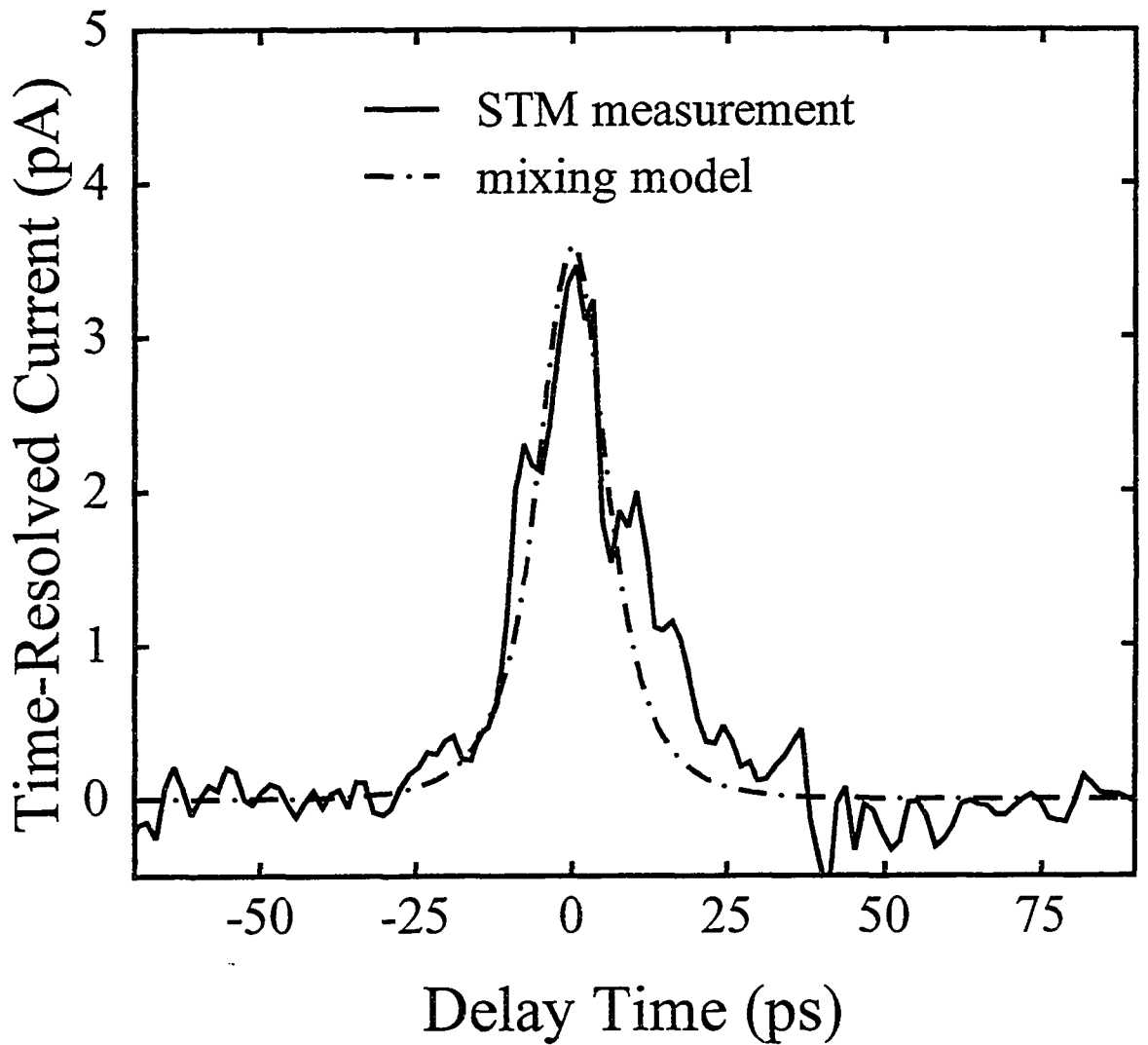
Figure 2.7: Time-resolved tunneling current (solid line), measured using 50 mV DC tunnel bias, 0.5 nA quiescent tunnel current, and 50 V photoconductive switch bias. The dashed-dot line is the mixing model signal using the parameters deduced from Fig. 2.6. The fit to the measured current yields 0.7 V for the amplitude of each voltage pulse.

laser beams) at a frequency (1.9 kHz) which is beyond the bandwidth of the STM feedback control loop and thus does not affect the DC tunneling conditions.

The solid line in Fig. 2.7 shows the measured signal with a DC tunneling bias and current of 50 mV and 0.5 nA, respectively, corresponding to a tunnel conductance of 10 nS. Both photoconductive switches were biased at 50 V relative to the line. The expected time- resolved signal can also be determined from a combination of the electrical correlation measurement and the I-V characteristic of Fig. 2.6(b). The result is shown by the dashed- dot line in Fig. 2.7. The only free parameter in this determination is the actual voltage pulse amplitude at the tunnel junction. Assuming the amplitude of both voltage pulses to be the same, a fit to the peak current yields 0.7 V for the pulse amplitude. The contribution from electrical reflections as seen in Fig. 2.6(a) has been ignored in this fit. Note that although transient displacement currents can be large, they do not contribute to the integrated signal. We have confirmed that this is true in the presence of the nonlinear tunneling conductance by numerical simulation of a lumped circuit element model.

The dependence of the peak amplitude of the time-resolved signal on the STM DC tunneling current is shown in Fig. 2.8. The proportionality of the transient currents to the DC current indicates the same dependence on the tunneling conductance, and in particular shows how the time-resolved signal vanishes as the tunneling barrier becomes large. The slope of this line has a sensitive (cubic) dependence on the amplitude of the voltage pulses used in the measurements, and is also proportional to the nonlinearity γ. Some scatter in the data may be caused by local variations of γ as the tip drifts during the course of the measurements. In addition, γ could depend systematically on the linear conductance, although we do not see evidence for this in the data.
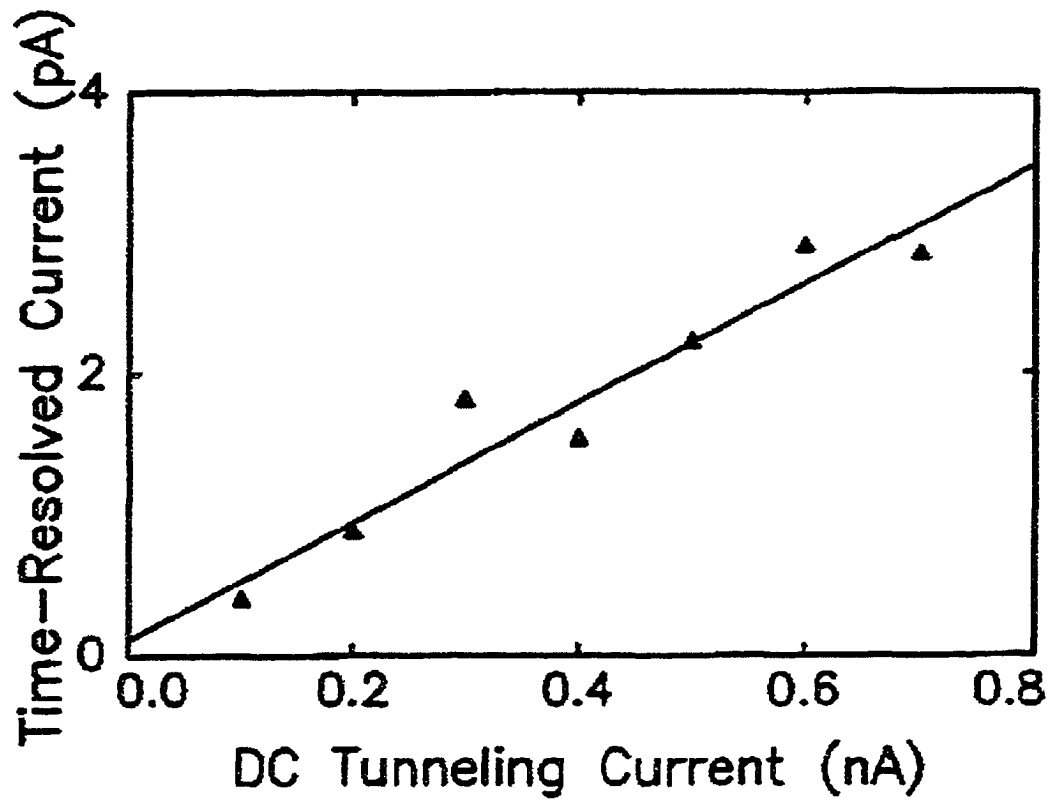
Figure 2.8: Peak amplitude of the time-resolved signal as a function of quiescent tunneling current. The abscissa is proportional to the linear tunneling conductance β (the bias voltage is fixed at 50 mV.)

Unlike the PG-STM measurements, in which the signal timing is governed by the electrical propagation time between the two photoconductive switches, the configuration of the present JM-STM experiment allows us to vary the signal timing independently and thereby confirm its tunnel junction origin. This is accomplished by comparing time- resolved tunneling signals measured at different positions along the transmission line. Fig. 2.9 shows two such measurements (symbols), along with the corresponding two-switch electrical correlation measurements (dotted lines) recorded on the same time axis. When the STM addresses the line at position (B) (see Fig. 2.5), to the right of switch 2, we find the signal shown by the open circles in the figure. The relative timing for electrical pulse coincidence at the tunnel junction is the same as that for the switch correlation measurement in this case. However, if the tip is placed at position (A) mid-way between the two switches, coincidence at the STM tip, and hence the time-resolved STM signal, should occur *before* the switch correlation signal, as is in fact observed (filled circles in Fig. 2.9). The relative time shift equals the electrical propagation time along the distance separating the two switches (5 mm at roughly 8 ps/mm). By causality, this rules out any possibility that other nonlinear interactions (between the switches, for example) play a role in generating the observed time-resolved signals.

In summary, we have presented new measurements establishing improved time-resolution in picosecond scanning tunneling microscopy using the junction mixing method. The electrical pulse width alone still determines the time-resolution in these experiments. Continued improvement is anticipated using still faster photo-switches and improved electrical geometries.

References

[1] S. Weiss, D. F. Ogletree, D. Botkin, M. Salmeron, and D. S. Chemla. *Appl. Phys. Lett.*, 63:2567, 1993.

66
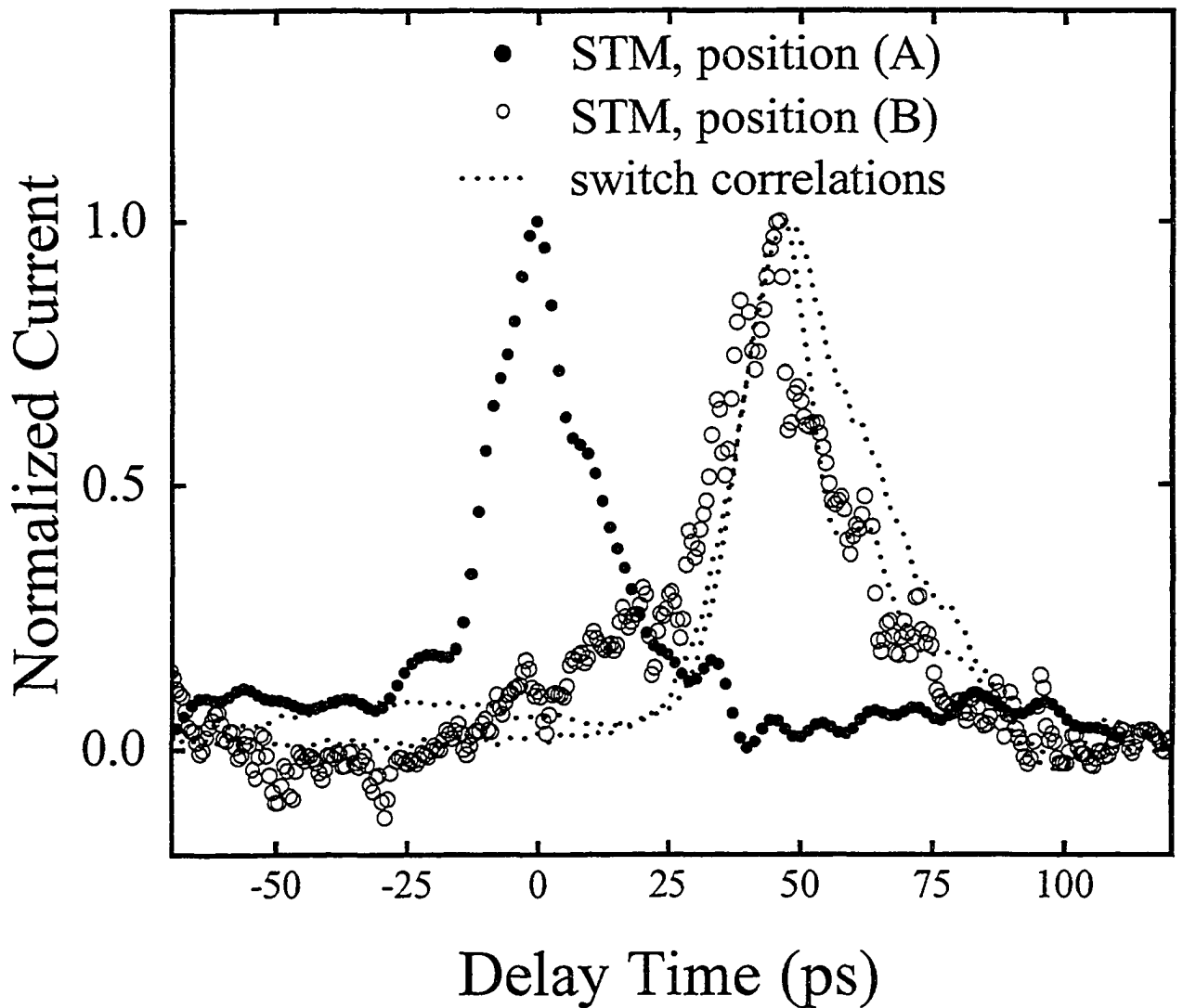
Figure 2.9: Time-resolved tunneling signals measured for different tip positions along the line, plotted as a function of probe pulse delay. Filled circles - position (A); open circles - position (B). Time zero corresponds to simultaneous arrival, at their respective switches, of the laser pump and probe pulses. The corresponding two-switch electrical correlation measurements are shown by the dotted lines. Separate electrical correlation measurements were made for each STM position because the switch characteristics degraded slowly with use.

67

[2] R. H. M. Groeneveld, Th. Rasing, L. M. F. Kaufmann, E. Smalbrugge, J. H. Wolter, M. R. Melloch, and H van Kempen. *J. Vac. Sci. Tech. B*, 14:861, 1996.

[3] M. R. Freeman and Geoff Nunes, Jr. *Appl. Phys. Lett.*, 63:2633, 1993.

[4] Geoff Nunes, Jr. and M. R. Freeman. *Science*, 262:1029, 1993.

[5] David H. Auston. *IEEE J. Quantum Electron.*, QE-19:639, 1983.

[6] A. Y. Elezzabi, J. Meyer, and M. K. Y. Hughes. *Appl. Phys. Lett.*, 66:402, 1995.

[7] David C. Fortin. STM from planning to scanning. Technical report, University of Alberta, 1995.

[8] C. Julian Chen. *Introduction to Scanning Tunneling Microscopy*. Oxford University Press, New York, 1993.

[9] M. B. Johnson, T. C. McGill, and N. G. Paulter. *Appl. Phys. Lett.*, 54:2424, 1989.

[10] Rickard E. Matick. *Transmission lines for digital and communication networks*. McGraw-Hill, New York, 1969.

[11] G. M. Steeves, A. Y. Elezzabi, and M. R. Freeman. *Appl. Phys. Lett.*, 70:1909, 1997.

[12] K. Takeuchi and Y. Kasahara. *Appl. Phys. Lett.*, 63:3548, 1993.

[13] D. Botkin, J. Glass, D.S. Chemla, D.F. Ogletree, M. Salmeron, and S. Weiss. *Appl. Phys. Lett*, 69:1321, 1996.

[14] R.H.M. Groeneveld and H. van Kempen. *Appl. Phys. Lett.*, 69:2294, 1996.

[15] G. Chui and J. M. Halbout. *US patent*, No. 5,019,707.

[16] T. Hesjedal, E. Chilla, and H.-J. Frohlich. *Appl. Phys. Lett.*, 69:354, 1996.

[17] M. Lambsdorff, J. Kuhl, J. Rosenzweig, A. Axmann, and Jo. Schneider. *Appl. Phys. Lett.*, 58:1881, 1991.

[18] J. G. Simmons. *J. Appl. Phys.*, 34:238, 1963.

[19] G. P. Kochanski. *Phys. Rev. Lett.*, 62:2285, 1989.

[20] R. Moller, U. Albrecht, J. Bonenberg, B. Koslowski, P. Leiderer, and K. Dransfeld. *J. Vac. Sci. Technol. B*, 9:506, 1991.

[21] C. Sammet, M. Volcker, W. Krieger, and H. Walther. *J. Appl. Phys.*, 78:6477, 1995.

Chapter 3

Nanometer-scale imaging with an ultrafast scanning tunneling microscope

3.1 Context

As the "Advances in picosecond scanning tunneling microscopy via junction mixing" [1] paper was being prepared for publication there were two significant developments in the field which were to stimulate the direction of subsequent experiments. The first was the publication of "Advances in ultrafast scanning tunneling microscopy" [2] by Weiss et al.. This publication reported 900 fs temporal resolution with inferred 10 nm spatial resolution using the photo-gated technique. These results suggested that the photo-gated technique was the fastest TR-STM technique in the world motivating us to examine the speed limitations of our junction mixing technique. The second development was much more significant, the publication by Groeneveld and van Kempen of "The capacitive origin of the picosecond electrical transients detected by a photoconductively gated scanning tunneling microscope" [3]. In this seminal work, Groeneveldt and van Kempen developed an accurate model of the relevant circuits involved in PG-STM. One critical feature of this model was the incorporation of the repetitive pump/probe pulses which contribute to charging effects over time scales larger than the duty cycle of the lasers used in earlier experiments. With this model, Groeneveldt and van Kempen concluded that the

70

photo-gated technique measured a signal which was fundamentally capacitive in origin! This reclassified PG-STM as a capacitive microscopy implying that it lacked ultimate STM spatial resolution in the time-resolved signal.

These results stressed the need for us to improve the speed of our transmission line structures in further time-resolved experiments, but more importantly they focused our attention on the issue of combined temporal-spatial resolution. Many groups attempting to use the PG-STM technique focused primarily on ultrafast time resolution, assuming that STM spatial resolution would necessarily follow. The Groeneveldt, van Kempen paper showed that in the case of PG-STM this was not so. Further efforts to establish JM-STM should aspire to improve time resolution while demonstrating the combined spatio-temporal resolution of the technique.

With these requirements in mind a new experiment was developed which would test the ability of the junction mixing technique to show spatio-temporal resolution. In past experiments the STM would tunnel into a transmission line while electrical pump/probe pulses were launched into the tunnel junction. The spatial extent of these electrical pulses is on the order of millimeters too large for the STM to resolve. To achieve spatial resolution in the time-resolved signal it would be necessary to scan the STM over a surface anomaly which would alter the time-resolved signal. If the time-resolved signal changed over the same length scale as the size of the anomaly, then this length scale would determine the resolution of the time-resolved signal. With this in mind, an experiment was developed, which would pattern μm sized dots of differing material onto the gold transmission line. By choosing the dot material for high I/V contrast with respect to gold, the time-resolved signal mixed in the tunnel junction between the STM tip tunneling into the gold transmission line versus this other material would also show contrast. By scanning the STM tip between the gold transmission line and the dot, we hoped to see a significant contrast in time-

71
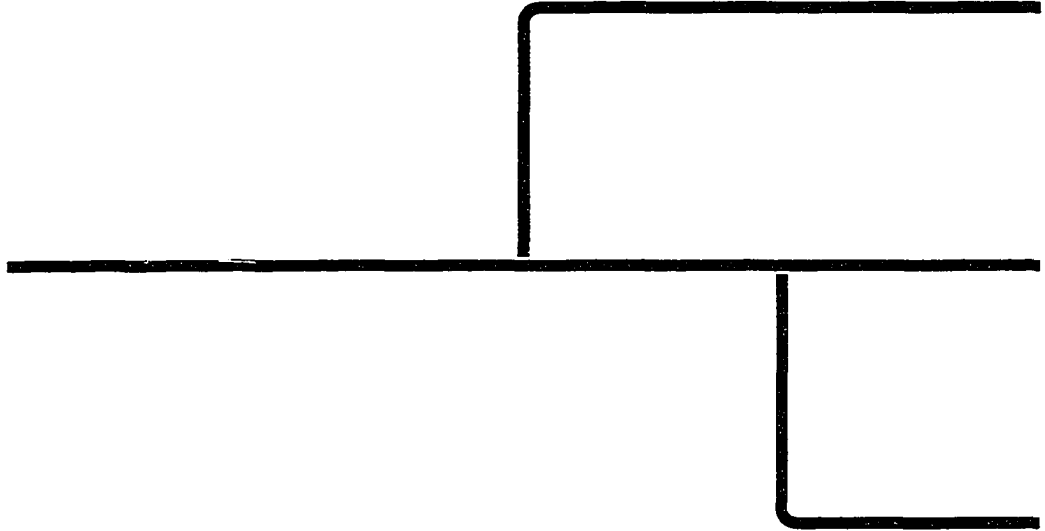
Figure 3.1: Transmission line structure generated by the stmtrl.dwg mask. Note that there are interdigitated fingers between both vertical line segments and the main horizontal transmission line

resolved signal, even though the DC tunneling current would remain unchanged in the transition.

At the outset of this work, it was necessary to create two complimentary masks for producing the transmission line substrates. One mask would be used to photolithographically define the basic transmission line structure. The first mask is a modified version of the mask used in Ref. [1]. The basic unit in the mask is shown in Figure 3.1.

This structure is 2 cm long(along the central transmission line) and 1 cm wide. The mask was designed using Autocad(file : stmtrl.dwg) and produced by Adtek Photomask. The mask was a chromium mask on a soda lime glass substrate, the minimum feature size used in this mask was 2 μm so a quartz substrate was not necessary. The mask was generated optically. Gaps between the vertical bias leads and the transmission line have been replaced by interdigitated fingers as in Ref. [4]

72
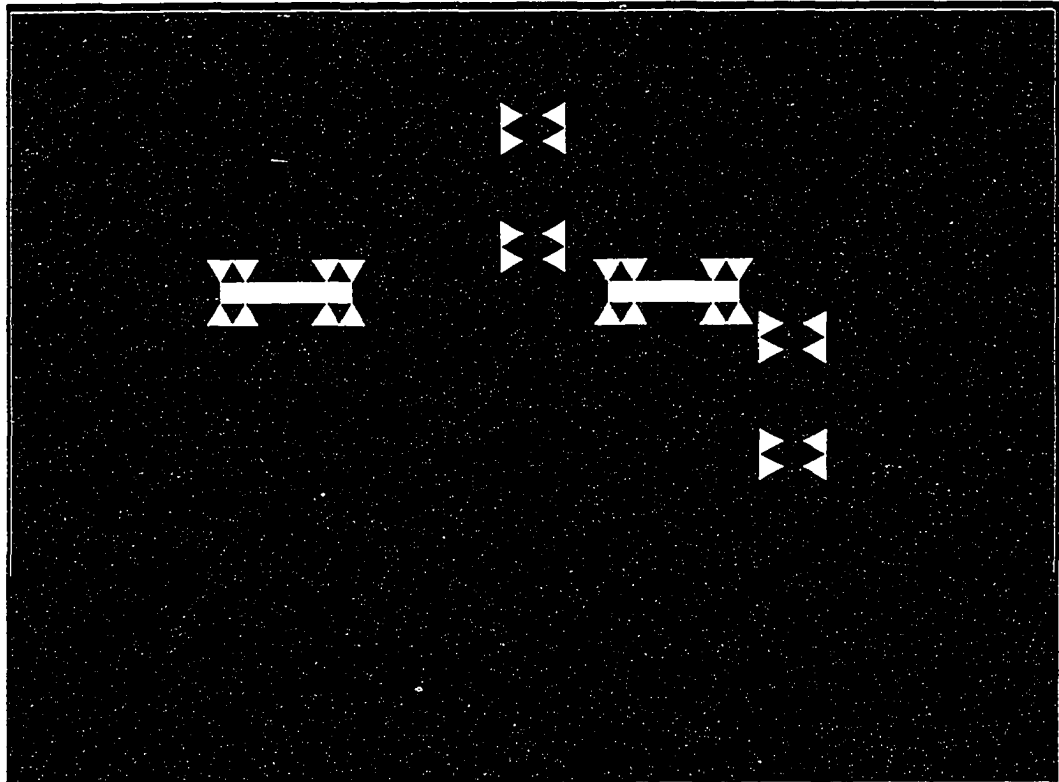
Figure 3.2: The complementary mask to that shown in Figure 3.1 where the sets of transparent triangles are used to align the mask over the transmission line structure and the clear rectangles represent a large array of $2\mu m$ square dots separated by $3\mu m$.

73
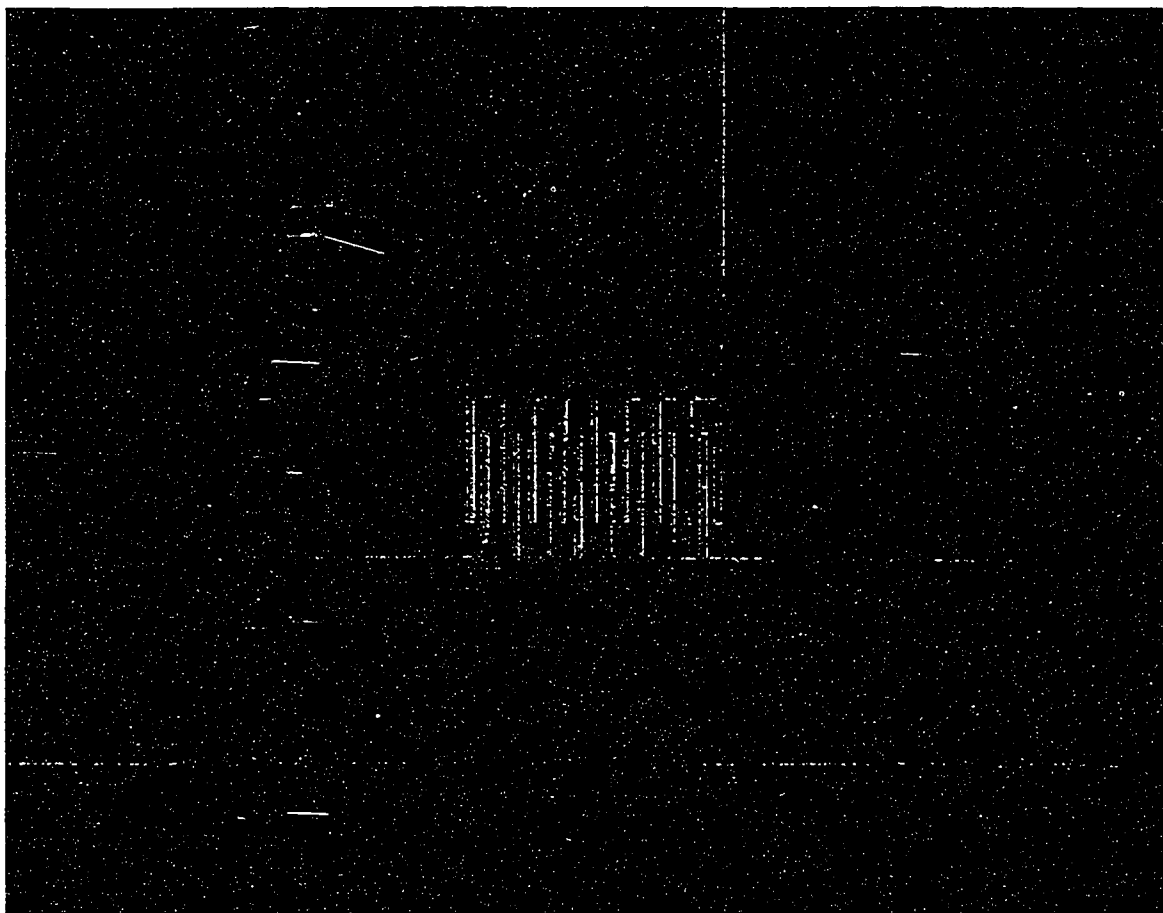
Figure 3.3: SEM image of the 5 μm interdigitated fingers between the 200μm main horizontal transmission line and the vertical line segments, referred to in the caption of Figure 3.1.

and the vertical leads were rounded to reduce electrical reflections in the structure. An SEM image of the interdigitated fingers is shown in Figure 3.3.

The second, complimentary mask, shown in Figure 3.2. was also created using Autocad(file : stmsq-b1.dwg [1]) and consisted of pairs of triangular alignment marks and over 80,000 2 μm^2 squares per transmission line(40,000 dots per patch on the transmission line). In creating our structures the first mask was used to pattern a gold transmission line structure onto our ion implanted GaAs substrate(implant dose was $1 \times 10^{-15} cm^{-2}$ at 200 keV) using standard photolithography. Once this was done, photoresist was spun onto the patterned substrate and the second mask was aligned.

---

[1]The autocad file contains the alignment marks for one transmission line structure and one set of four dots, the dot pattern must be stepped and repeated to fill the space between horizontal alignment triangles and the whole file must be stepped and repeated to create a mask paired with the one created from stmtrl.dwg

74

The mask was aligned such that the vertical bias leads of the transmission line were positioned between the vertical pairs of triangles. This allows positioning of the second mask in the horizontal direction. By lining the horizontal transmission line of the patterned substrate between the horizontal pairs of triangles, vertical alignment is achieved. The long horizontal rectangles shown in Figure 3.2 are filled with the 2 μm^2 dots, so that the second mask will produce huge arrays of dots in the photoresist on the patterned substrate. Once the photoresist is exposed and developed, there will be an array of holes in the resist above the transmission line. By depositing a film into the holes and over the photoresist and then removing the photoresist, a patterned array of dots will remain. This technique is known as liftoff, and the result of the procedure for patterning chromium dots onto a gold transmission line structure is shown in Figure 3.4.

To provide contrast in the time-resolved signal tunneling into gold versus into a dot it was necessary to carefully choose the material with which to fabricate the dots. We planned on sputtering this material into the photoresist holes, so we wanted to choose a material which was available and could easily be sputtered(note: It was subsequently learned that evaporation is a more effective method of deposition for liftoff, as it is more directional with poorer sidewall coverage of the holes, an asset in the subsequent photoresist etching process). Contrast in time-resolved signal could easily be achieved if there was contrast in the relevant domain of the I/V tunneling characteristics. I/V characteristics had been obtained for tunneling into gold transmission lines in ambient conditions, so we began acquiring I/V characteristics of other available metals for comparison with gold. Experiments using titanium quickly demonstrated significant contrast with gold. For a comparison of I/V characteristics see Figure 3.9. Because of this striking contrast titanium dots were the first to be fabricated and tested.

Initial STM attempts to image the titanium dots were hampered by the size of the titanium dots and their spacing(2 μm dots spaced 3 μm apart). Efforts were

75
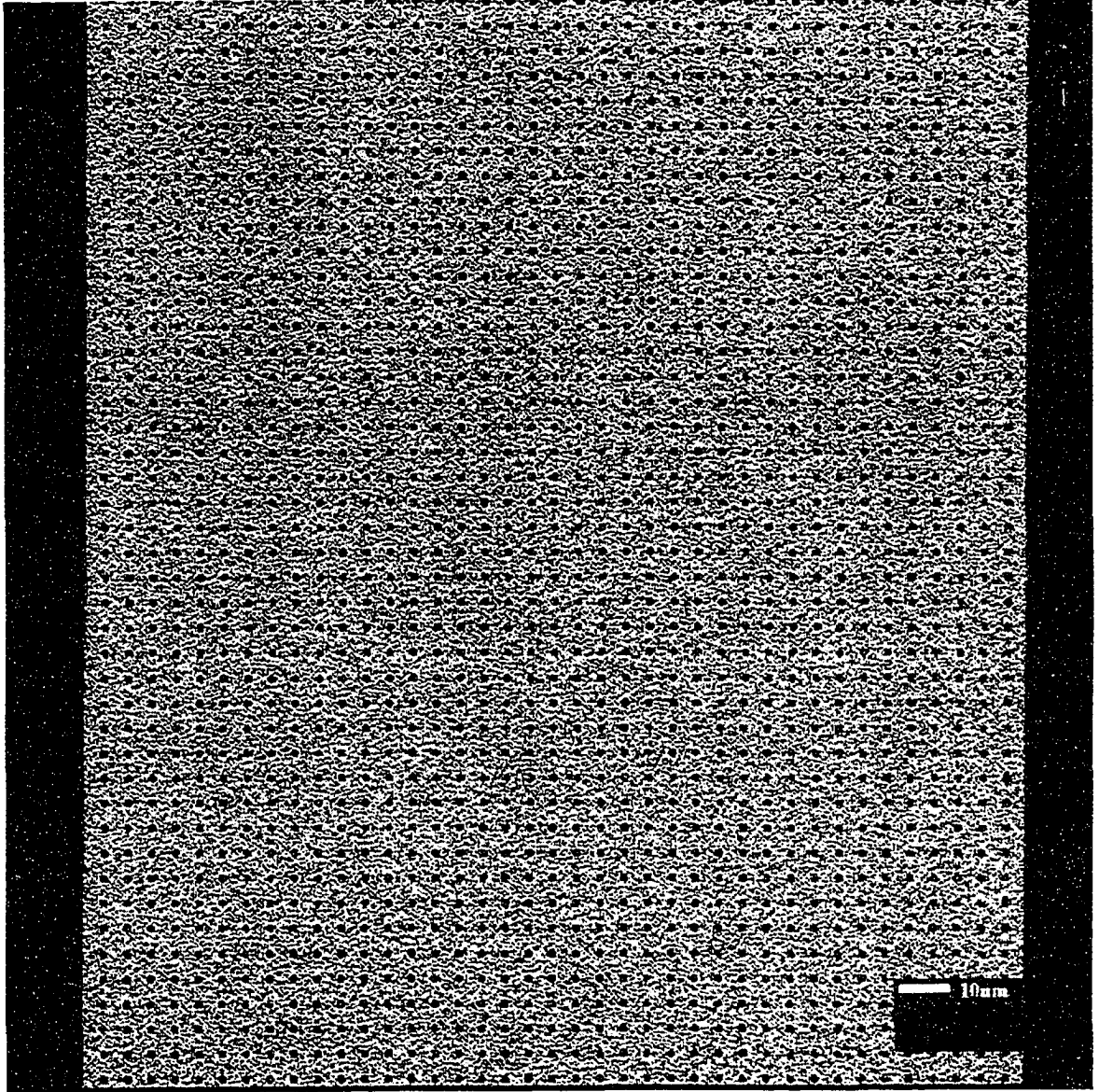
Figure 3.4: An array of $2\mu m$ chromium dots, patterned onto a gold transmission line. The edge of the gold transmission line, and the underlying GaAs substrate can be seen on either side of this SEM image.

76

made to minimize the size of the dots and using optically fabricated masks, 2 μm^2 dots were at the technological limit. E-beam masks were another option, but the write time to produce multiple arrays of hundreds of thousands of dots would make an e-beam mask prohibitively expensive. The scan range of our STM was about 5 μm^2 but any tilt of the sample would cause the microscope to move out of the range of its feedback electronics. Because of this problem, software was developed which would identify sample tilt in an initial small area scan, and compensate for this tilt in subsequent larger scans. Non-linearities of piezo displacement with applied voltage were also identified and corrected for using this software. [2] Once this software was implemented, titanium dots could be imaged. Many images were acquired such as is shown in Figure 3.11 (a). But through multiple scans the surface of the titanium dot appeared to be changing. A vivid demonstration of this is shown in Figure 3.5 and Figure 3.6.

Figure 3.5 shows a 2.76 μm STM topographic image of a titanium dot patterned onto a gold transmission line (mr050922.d97). Between that figure and Figure 3.6, the STM scan range was decreased to 0.92 μm and multiple scans were taken (mr050929.d97; mr050932.d97; mr050934.d97; mr050939.d97; mr050944.d97; mr050947.d97). The final 2.76 μm image (mr050950.d97) was then acquired exhibiting considerable changes in surface topology. All scans were done with a 35 mV bias voltage and STM current set to 0.5 nA. From Figure 3.6 it is clear to see the affected patch on the dot, appearing as a dip in surface topography, caused by a decrease in conductivity in that region. Since samples with titanium dots had been fabricated it was decided to proceed with these samples even though they oxidized through repeated scanning.

Initial time-resolved spatial images of the structures were created using the experimental setup shown in Figure 2.5 where the improved transmission line struc-

---

[2]The program "STM Scan w/N-Regression v3.4" is described on page 149 in A.3 of the Appendix.
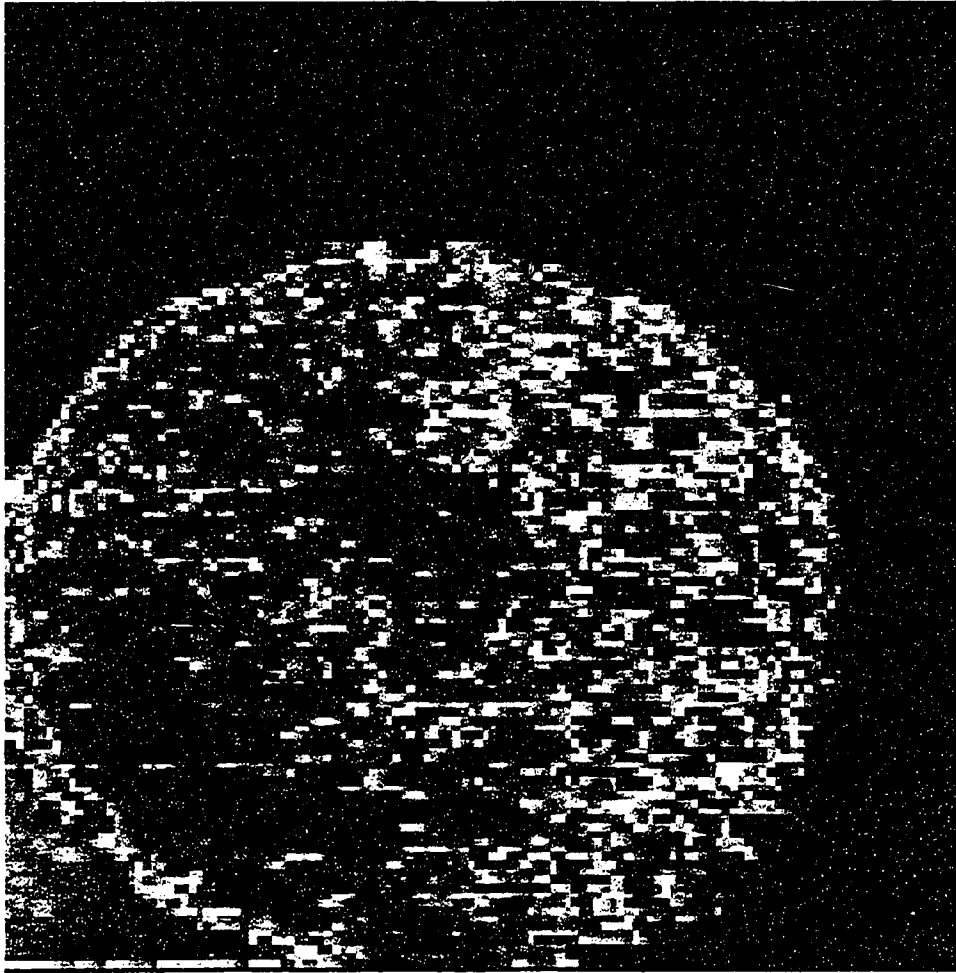
Figure 3.5: 2.76 μm by 2.76 μm, z range 50 nm scan of a 2μm titanium dot patterned onto a gold substrate. Tunneling performed at 35 mV bias voltage, 0.5 nA tunneling current.

78
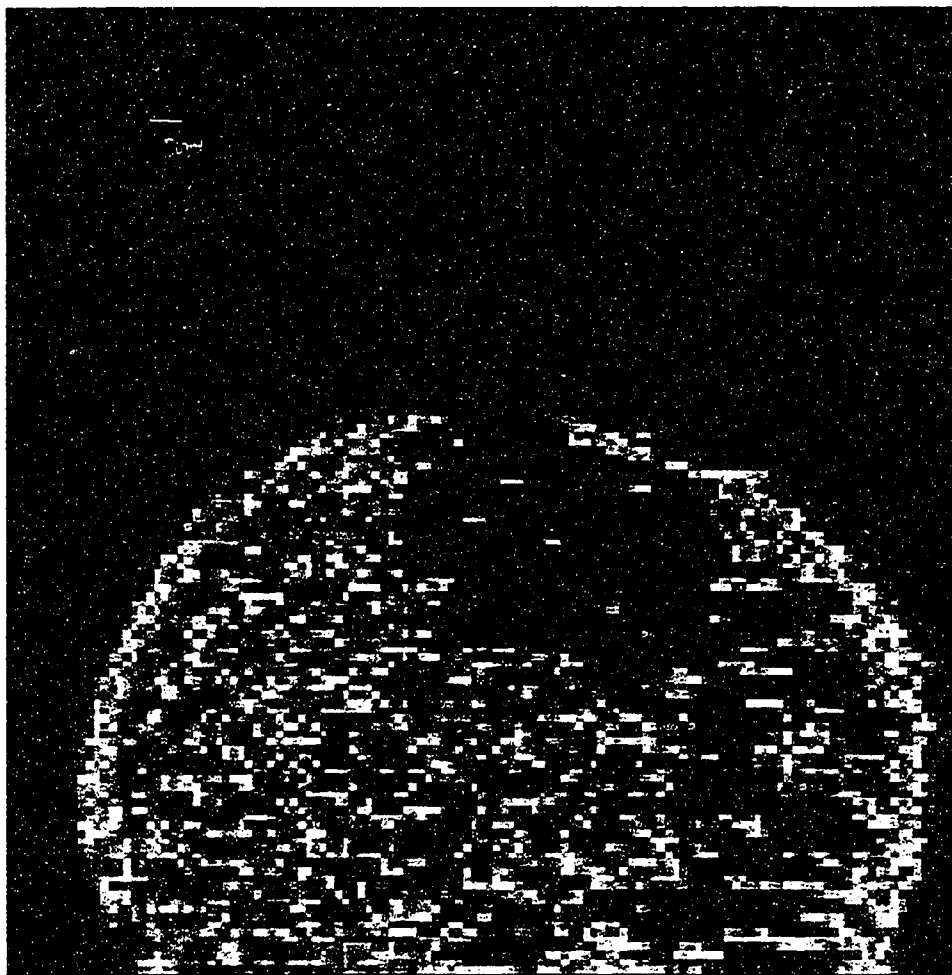
Figure 3.6: 2.76 μm by 2.76 μm, z range 50 nm scan of the same titanium dot shown in Figure 3.5 where a square section has been repeatedly scanned with the STM. Tunneling performed at 35 mV bias voltage, 0.5 nA tunneling current.

79
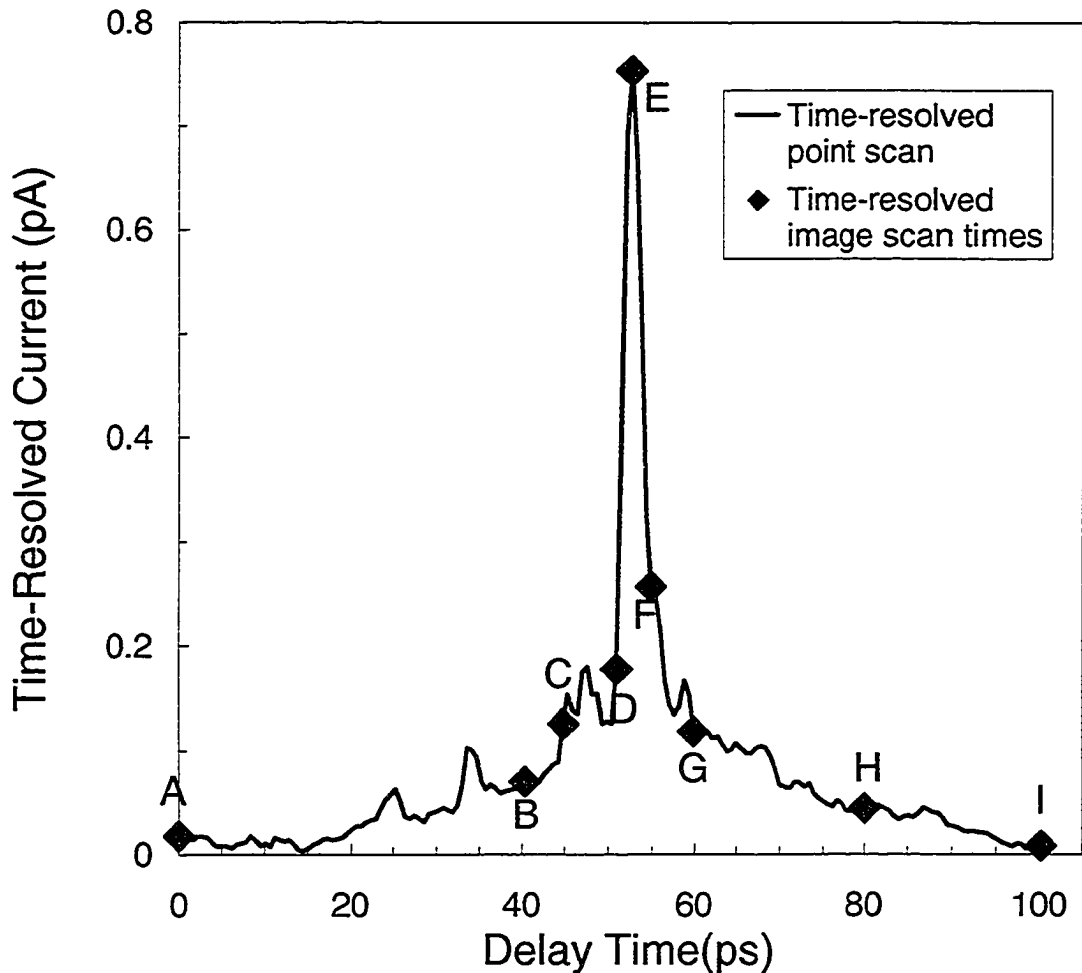
Figure 3.7: Time-resolved STM current measurement. This timing trace was used to map out the passing of pump/probe pulses past the tunnel junction of the STM. Points labelled A-I mark the times of subsequent time-resolved image scans shown in Figure 3.8.

tures described above were used. Laser pulses created pump and probe electrical pulses which were transmitted along the central gold transmission line towards the STM tunnel junction. Measuring the time-resolved current at a single point yielded the time-resolved current trace shown in Figure 3.7. Times were chosen from this trace(indicated by the diamond markers) at which to perform time-resolved image scans. Once these delay times were selected, the optical delay line was set to the correct offset and an image would be acquired. Images were taken as 64×64 grids of tunneling current, feedback signal(topography), and time-resolved current(as mea-

80

sured using a lock-in amplifier). The tunneling conditions were 0.5 nA current and -30 mV bias,[3] the photoconductive switches were biased to -30 V and the lock-in time constant was set to 100 ms. The scan program was set to wait 150 ms per point, which is quite fast and could result in some blurring of the time-resolved signal. The image frames for the times shown in Figure 3.7 are shown in Figure 3.8. The images in this figure represent the first STM movie!

3.2 Publication

G. M. Steeves, A. Y. Elezzabi and M. R. Freeman, *Appl. Phys. Lett.* **72**, 504(1998).

Ultrafast optical pump-probe techniques offer the possibility of studying many physical phenomena on picosecond and femtosecond time scales with a temporal resolution limited only by the duration of the laser pulse. The shortest laser pulses are now on atomic time scales [5], however atomic-scale spatial resolution still requires non-optical techniques such as scanning tunneling microscopy (STM). STM applications, on the other hand, have largely been restricted to the study of static surface properties (topography and electronic structure), revealing little information about the dynamics underlying the phenomena under investigation. An ultrafast STM, with temporal information added as an observable quantity, would be a valuable addition to the arsenal of tools for studying nanometer-scale systems.

To address the need for such a device, two experimental schemes have been proposed and demonstrated as possible candidates for the operation of an ultrafast STM: photoconductively gated STM (PG-STM) [2, 6, 7] and junction mixing STM (JM-STM) [8, 9, 10, 1]. Even though subpicosecond temporal resolution was demonstrated with the PG-STM technique, a major concern is the demonstration of ultrafine spatial resolution. Recently, Groeneveld et al. [3] showed that PG-STM is really a (tunneling-stabilized) scanning *capacitance* microscopy, and cannot be expected to yield the fine

---

[3]we found that the titanium surface would not oxidize as quickly with negative bias voltages

81
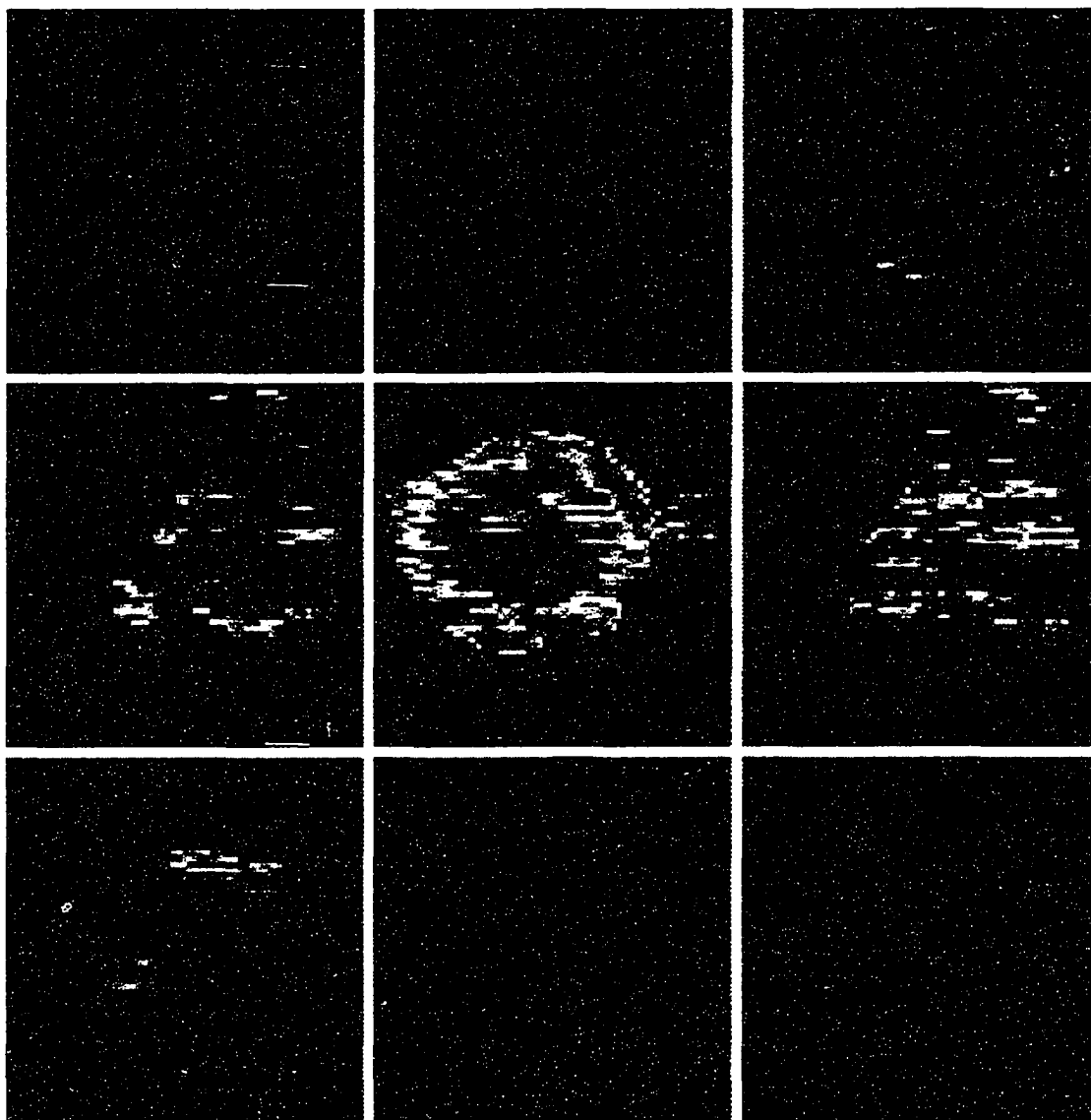
Figure 3.8: Time-resolved STM image scans, colour contrast represents contrast in time-resolved current between titanium and gold. The letters in the upper left corner of each scan correspond to pump/probe delay times in Figure 3.7.

82

lateral resolution of STM (although it still can have useful applications [11]). In JM-STM all the evidence points to a tunnel junction origin of the signal, but a final and unambiguous confirmation can only be obtained through a demonstration of the spatial resolution. This paper describes a proof of principle experiment indicating that atomic resolution should be possible in ultrafast STM.

The STM tip-metal sample tunneling current-voltage $(I-V)$ characteristics are similar enough for present purposes to those of a planar metal-insulator-metal junction. The time-dependent STM tunnel junction current-voltage relation can be expressed as [12],

$$I(t) \propto \beta[V(t) + \gamma V^3(t)] + 0[V^5(t)], \tag{3.1}$$

where $I(t)$ is the tunneling current, $V(t)$ is the tunneling voltage, β is the linear tunneling conductance, and γ depends on the electronic structure. Mixing of ultrafast electrical transients is employed in order to perform measurements on picosecond time scales. The mixing allows the measurement of ultrahigh frequencies (up to THz), far above normal STM bandwidth. In the junction mixing STM (JM-STM) technique, one effectively has two time-dependent biases, $V_1(t)$ and $V_2(t)$, at the tunnel junction, where one is the signal of interest and the other an electrical "probe pulse". Due to the non-linear term in equation 3.1, the resultant tunneling current amplitude $I(V_1(t) + V_2(t))$ is greater than the sum of tunneling currents of the two individual voltage pulse amplitudes, $I(V_1(t)) + I(V_2(t))$. The time-integrated STM tunneling current depends on the degree of the temporal overlap of $V_1(t)$ and $V_2(t)$. When the two pulses arrive simultaneously at the tunnel junction, the detected signal is larger than if they arrive at different times. By varying the delay between the pump and probe pulse and recording the time-integrated current from the STM, we obtain a correlated signal which can be deconvolved with the electrical pulses to obtain the temporal response of the system [8, 9, 10, 1].

From Eq. 3.1 it can be seen that the excess current amplitude is proportional to γ. A direct test of spatial resolution in the method can thus be performed by preparing a test surface having electronic structure contrast, created by patterning metal surfaces with distinct $I - V$ non-linearities. By measuring the time-resolved signal across an edge between the two distinct surfaces, we can estimate the spatial resolution of the time-resolved measurements. The observed signal step will represent an upper bound on the ultimate resolution of the technique, as it may also be limited by the edge definition of the sample itself.

For the present tests, we developed a structure consisting of titanium dots on a gold surface. Figure 3.9 illustrates the $I - V$ curves for both gold and titanium films measured at a fixed linear tunneling conductance $\beta = 23$ nS. The measurements are carried out with the STM operating under ambient conditions. The values of γ can be determined by fitting the experimental data to equation 3.1, yielding $\gamma = 1.3V^{-2}$ and $44V^{-2}$ for the Au and Ti surfaces, respectively. The ratio of the γ's is large, making the two surfaces an attractive choice because good contrast is expected in the time-resolved signal.

The details of experimental setup are described in Ref. [1]. The primary component is a high-speed transmission line, which is shown schematically in Figure 3.10. The structure is designed to reduce the dispersion of the picosecond pulses and to enhance the amount of the photogenerated current. The structure consists of three 100 nm thick, 200 μm wide Au lines spaced 5 mm apart on a semiconductor substrate. These lines are fabricated photolithographically on an H^+ ion-implanted GaAs semi-insulating substrate (dosage of $1 \times 10^{-15}cm^{-2}$ at 200 keV). A pair of 2 μm gap inter-digitated GaAs photoconductive switches are fabricated on each side of the central Au transmission line. Using the ion dosage of $1 \times 10^{-15}cm^{-2}$, the expected carrier lifetime of the photoconductive switches is of order 1 ps. However, the switches seem

84
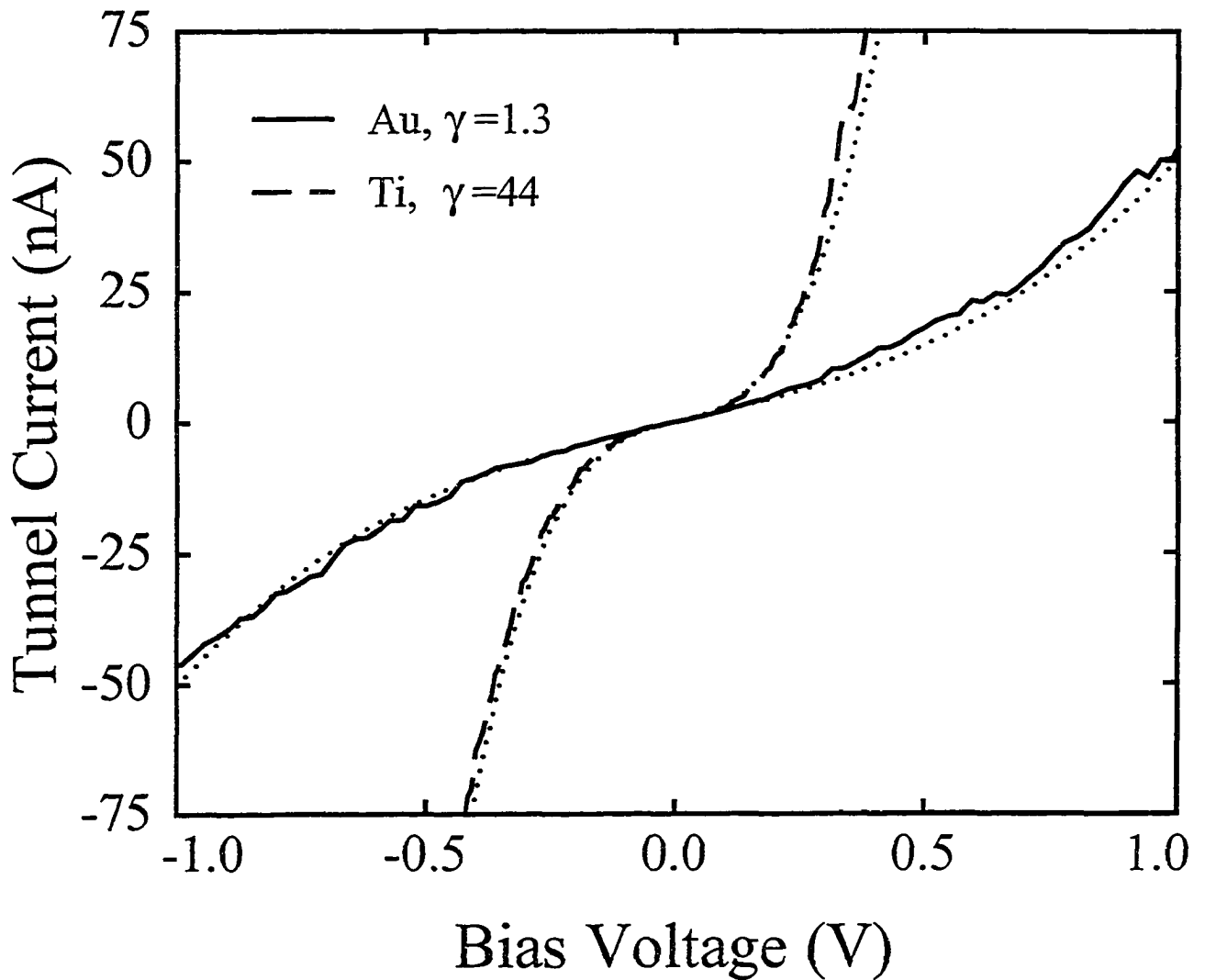
Figure 3.9: Measured current-voltage characteristics of the STM (Pt-Ir tip, ambient operation) for both gold and titanium thin film surfaces. The quiescent tunneling parameters are 30 mV and 0.5 nA, prior to the bias voltage sweeps.

AU TRANSMISSION LINE

TI MICRO DOTS

PHOTOCONDUCTIVE
SWITCH
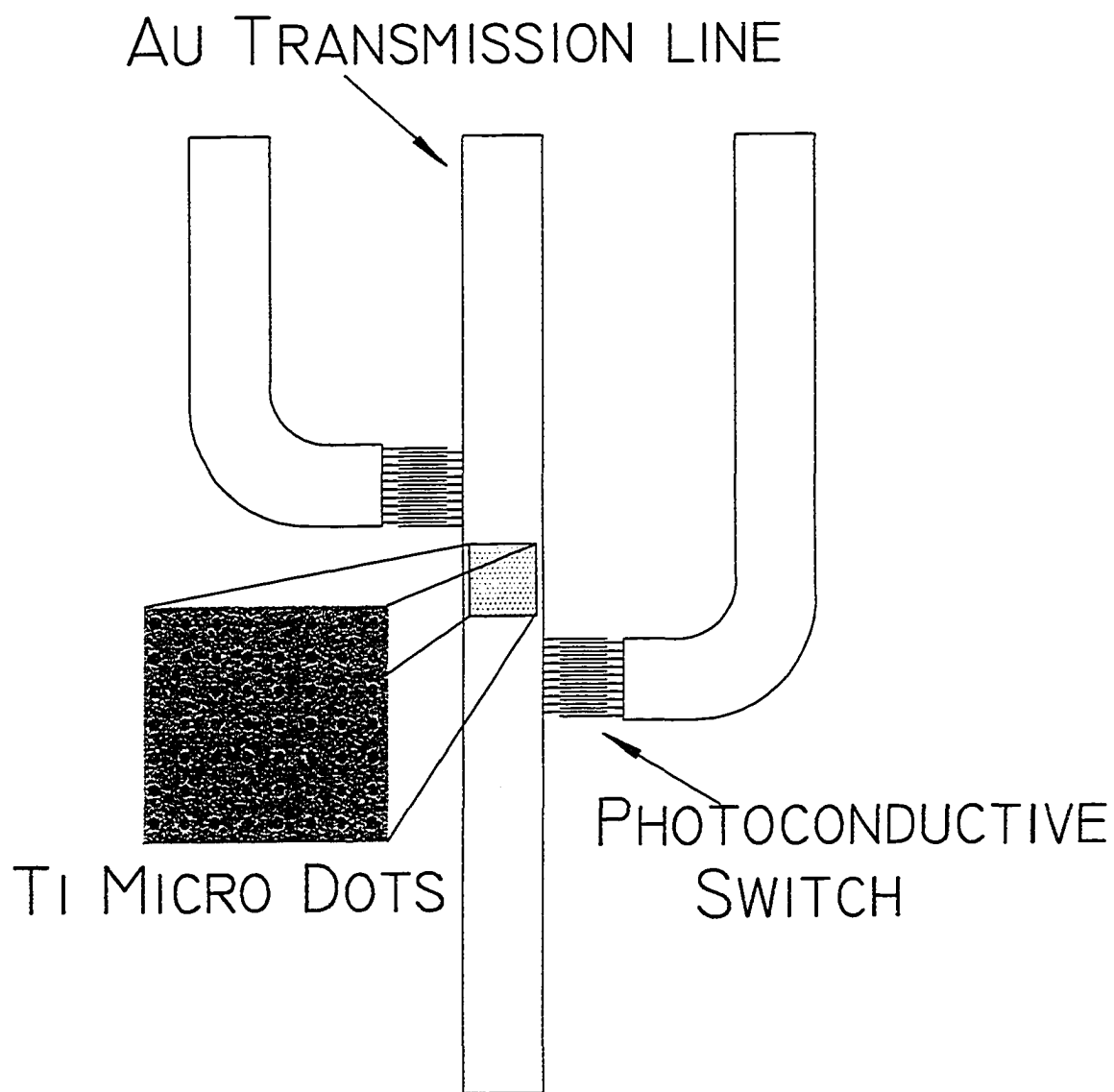
Figure 3.10: Schematic illustration of the high-speed Au transmission line and the interdigitated photoconductive switches. A scanning electron micrograph shows the Ti dot pattern atop the transmission line on an expanded scale.

86
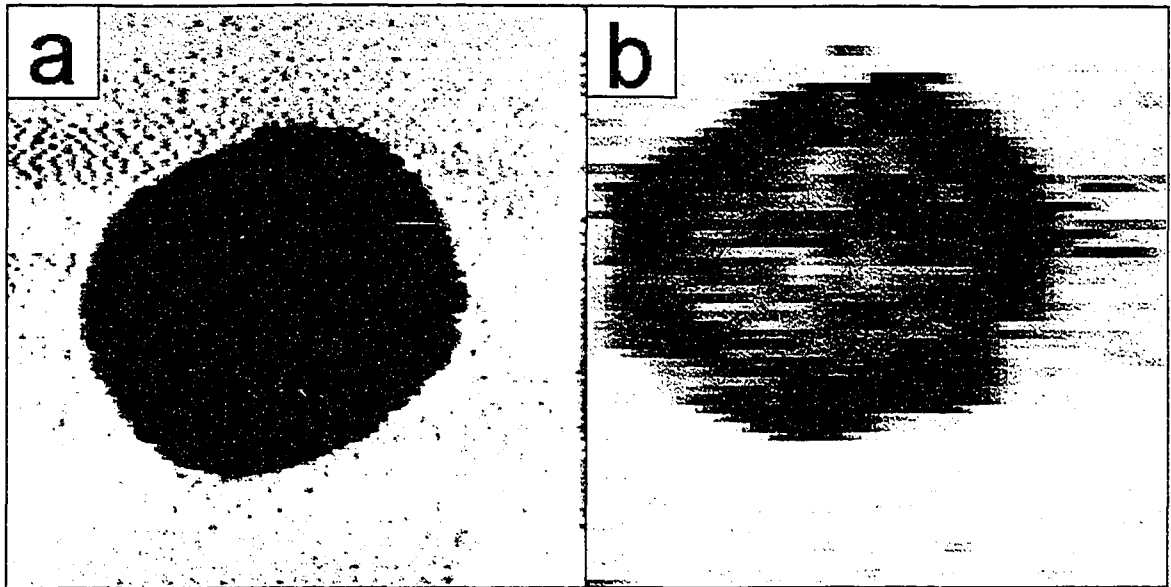
Figure 3.11: (a) A topographic STM image of a typical 3 μm × $3\mu m$ Ti dot used in the measurements. (b) A time-resolved STM image of another Ti dot taken at 0 ps.

to age quite rapidly and during the measurements reported here the electrical pulse width was approximately 20 ps. In order to test the spatial resolution of the STM, any array of 20 nm thick Ti micro-dots (nominally 3 μm squares) are patterned by photolithography and lift-off along the central Au transmission line.

Figure 3.11(a) shows a topographic STM image of a Ti dot, acquired at a constant tunneling current of 0.5 nA. After locating a dot through normal scanning, the STM is switched to time-resolved mode through pulsed illumination of the photoconductive switches. The optical delay line is scanned to determine the exact probe-pulse time delay position for maximal electrical pulse overlap at the tunnel junction for this tip location along the transmission line. This delay line position is labeled as time '0 ps' and is used as a time-reference point throughout the experiment. Figure 3.11(b) shows a coarse spatial scan of the time-resolved signal in the vicinity of a Ti dot at 0 ps. The Ti dot structure is observed with good contrast, as anticipated. The lock-in time constant was 300 ms for this 64×64 pixel image, which took 25 minutes to acquire.
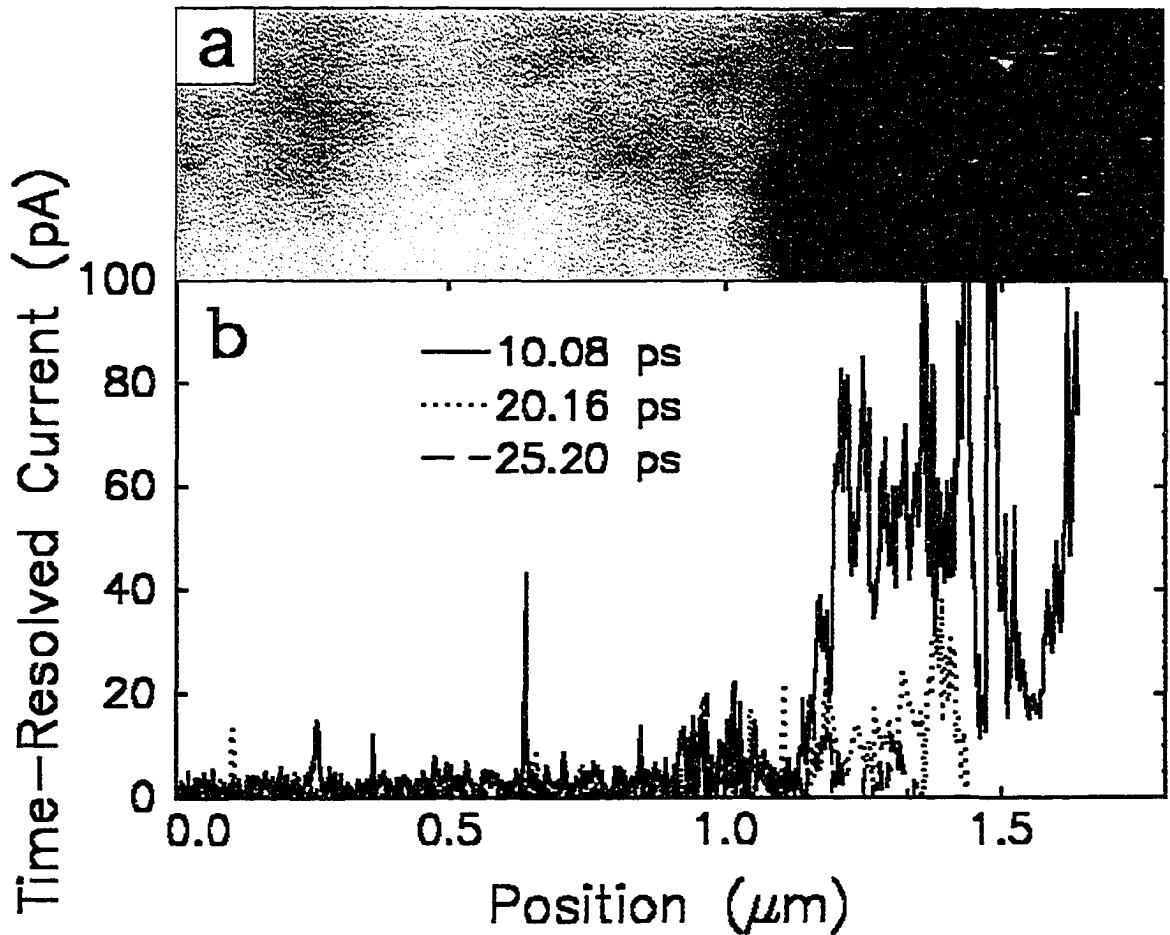
Figure 3.12: Higher resolution views of a Au/Ti edge. (a) topographic (b) time-resolved at probe delays of 10, 20, and 25 ps.

Higher resolution scans of the step edge are shown in Figure 3.12. Another topographic scan is shown in panel (a), accompanied in panel (b) by line-scans of the time-resolved signal taken across the central part of the topographic image. A series of spatial scan traces are shown at delay times of 10, 20, and 25 ps. As the probe electrical pulse is delayed relative to the pump, the measured signal amplitude or image strength decreases until the signal disappears when there is no longer significant pulse overlap at the tunnel junction.

Finally, by focusing the microscope on the step edge at $t = 0$ as shown in Figure 3.13, we can obtain a bound on the spatial resolution in time-resolved mode of 10 nm. We do not expect with such a structure to be able to place a limit on resolution

88
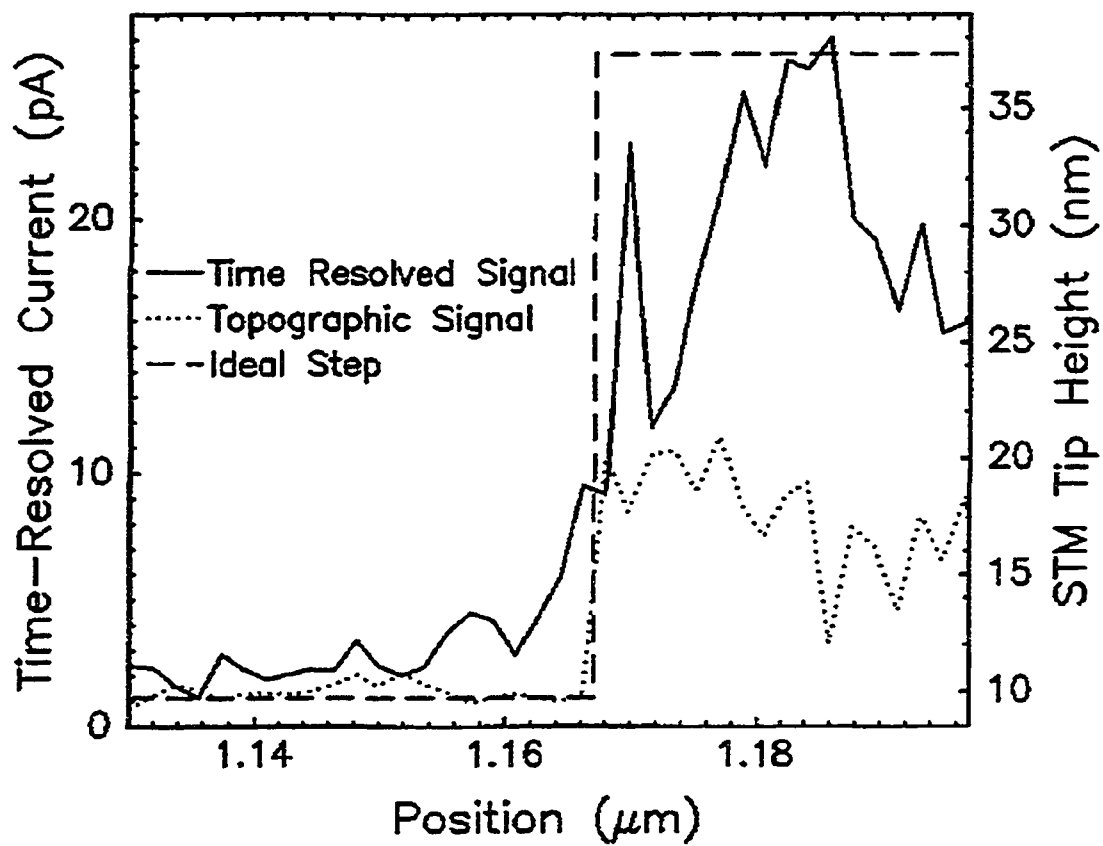
Figure 3.13: Zoom-in on the time-resolved signal at the step-edge at t = 0 ps.

89

much better than the 20 nm thickness of the Ti dot, owing to the lithographic definition of the edge. This observation of the edge boundary of the Ti structure at our expected limit of resolution reinforces the conclusion that the tunneling signal alone is time-resolved in these experiments. The geometrical capacitance between the STM tip and the sample does not play a role in limiting or degrading the spatial resolution in the operation of a JM-STM [8, 9, 10, 1].

In summary, we have presented experimental results that demonstrate the spatio-temporal operation of a JM-STM. In particular, picosecond time-domain measurements of electronic structure have been obtained with a fine spatial resolution of 10 nm. This demonstration of nanometer-scale imaging in ultrafast STM is another significant step towards the ultimate goal of atomic resolution on ultrafast time scales

References

[1] G. M. Steeves, A. Y. Elezzabi, and M. R. Freeman. *Appl. Phys. Lett.*, 70:1909, 1997.

[2] D. Botkin, J. Glass, D.S. Chemla, D.F. Ogletree, M. Salmeron, and S. Weiss. *Appl. Phys. Lett*, 69:1321, 1996.

[3] R.H.M. Groeneveld and H. van Kempen. *Appl. Phys. Lett.*, 69:2294, 1996.

[4] A. G. Foyt, F. J. Leonberger, and R. C. Williamson. *Appl. Phys. Lett.*, 40:447, 1982.

[5] A. Baltuska, Z. Wei, M. S. Pshenichnikov, and D. Wiersma. *Opt. Lett.*, 22:102, 1997.

[6] R. H. M. Groeneveld, Th. Rasing, L. M. F. Kaufmann, E. Smalbrugge, J. H. Wolter, M. R. Melloch, and H van Kempen. *J. Vac. Sci. Tech. B*, 14:861, 1996.

[7] U. D. Keil, J. R. Jensen, and J. M. Hvam. *Appl. Phys. Lett.*, 70:2625, 1997.

[8] Geoff Nunes, Jr. and M. R. Freeman. *Science*, 262:1029, 1993.

[9] M. R. Freeman and Geoff Nunes, Jr. *Appl. Phys. Lett.*, 63:2633, 1993.

[10] M. R. Freeman and Nunes G., Jr. *Appl. Surf. Sci.*, 107:238, 1996.

[11] J. R. Jensen, U. D. Keil, and J. M. Hvam. *Appl. Phys. Lett.*, 70:2762, 1997.

[12] J. G. Simmons. *J. Appl. Phys.*, 34:238, 1963.

Chapter 4

Circuit Analysis of an Ultrafast Junction Mixing Scanning Tunneling Microscope

4.1 Context

The "Nanometer-scale imaging with an ultrafast scanning tunneling microscope" [1] was well received. Attention was drawn to this work through an article in Physics World [2]. Many groups continued to use the Photo-gated technique as it had garnered some inertia, regardless of its inferior spatial resolution. In order to further understand the limitations on the junction mixing technique we endeavored to build a simple circuit element model of the STM tunnel junction. This model was based on the circuit illustrated in Figure 4.2. Details of this model and current calculations from it will now be given.

The basic equation of interest solves the tunneling current equation for detected current through the tunnel junction of the STM. Initially we introduce a time-varying voltage on the transmission line $V(t)$ and the current $I(t)$ measured at the output of the microscope. The current component passing through the capacitor is $I_c(t)$ and through the nonlinear tunnel resistance $R_t(V)$ (see equation 1.27) is $I_r(t)$. Referring to Figure 4.2 we see that charge on the transmission line can dissipate by flowing through the effective resistance of the tunnel junction, charge can also store in the

capacitor formed between STM tip and sample. From these conditions one can write the equation:

$$V(t) - I_r(t)R_t - ZI(t) = 0 \qquad (4.1)$$

and :

$$V(t) - \frac{Q_c}{C_t} - ZI(t) = 0 \qquad (4.2)$$

where $V(t)$ represents two pulses on the transmission line, $I_r(t)$ is the current through the tunneling resistance R_t, $I(t)$ is the total current and Z is the line impedance. When we differentiate 4.2 with respect to time we get:

$$\frac{dV(t)}{dt} - \frac{I_c}{C_t} - Z\frac{dI(t)}{dt} = 0 \qquad (4.3)$$

since $I_c + I_r = I(t)$ we can substitute equation 4.1 into equation 4.3 yielding:

$$\frac{dV(t)}{dt} - Z\frac{dI(t)}{dt} - \frac{I(t)}{C_t} + \frac{V(t)}{R_tC_t} - Z\frac{I(t)}{R_tC_t} = 0 \qquad (4.4)$$

or in terms of the tunneling current:

$$\frac{dI(t)}{dt} = \frac{1}{Z}\frac{dV(t)}{dt} - \frac{1}{Z}\frac{I(t)}{C_t} - \frac{I(t)}{R_tC_t} + \frac{1}{Z}\frac{V(t)}{R_tC_t} \qquad (4.5)$$

This is the derived equation for the time dependent tunneling current (equation 4.16). [1]

Solving this equation for $I(t)$ will give the transient current contribution caused by the transient voltage $V(t)$ traveling down the transmission line. Integrating $I(t)$ over the duty cycle of the laser will give the net current contribution measured by the

---

[1] The model shown in Figure 4.2 treats the transmission line as an impedance Z in series with the STM tip. In Appendix C a different treatment of the transmission line is explored.

lock-in amplifier. $V(t)$ is given by adding two voltage pulses together where the time separation between each voltage pulse is t_0. The form of one of the voltage pulses is given by equation 4.17:

$$V_1(t) = V_0 \int_{-\infty}^{t} \sec h^2 \left(\frac{\tau}{t_p}\right) \exp\left(\frac{\tau - t}{t_c}\right) d\tau \qquad (4.6)$$

where V_0 is the amplitude of the voltage pulse and $t_0 = 0$. This equation can be solved analytically with a solution in terms of hypergeometric functions[2]:

$$_2\mathcal{F}_1\left\{1, 2; 2 + \frac{1}{t_p}; \frac{1}{e^{-t}+1}\right\} \times \frac{\sec h^2 \frac{t}{2}}{1 + \frac{1}{t_p}} \qquad (4.7)$$

A series of electrical pulses for different pulse-widths can been seen in Figure 4.1. Summing two such pulses with different relative arrival times at the tunnel junction gives us our function $V(t)$. In order to evaluate $I(t)$ we still need to calculate the geometrical tip/sample capacitance C. Using a finite element model based on the method of images, Dr. R. A. Said was able to calculate the tip sample capacitance for a model STM tip at tip/sample separations from $21 \to 2$ nm. Details of this calculation can be found in Dr. Said's thesis [3]. Extension of this calculation down to Å length scales was not possible as the element size used in the calculation was 2 nm. In order to calculate the capacitance at Å separations the Said model was fit with a 2 capacitor system where the bulk of the STM tip was treated as a single parallel plate capacitor, and the apex of the tip as another parallel plate capacitor. This model was fit to the Said data and then extended down to 2 Å tip/sample separation as shown in Figure 4.3. From the fit it was clear that a value of 33 fF would suffice to capture the geometrical capacitance of the tip/sample system. The effect of varying this capacitance by small fractions is negligible and the effect of large variations in capacitance is shown in Figure 4.5.

Once the capacitance and the voltage pulse $V(t)$ are known we can calculate the current pulse $I(t)$. The current pulse was calculated by Bob Teshima using the

---

[2]In mathematica this is expressed as: Hypergeometric2F1[1,2,2+1/pulsewidth,1/(Exp[-t]+1)]*(Sech[t/2]*Sech[t/2])/(1+1/pulsewidth)

94
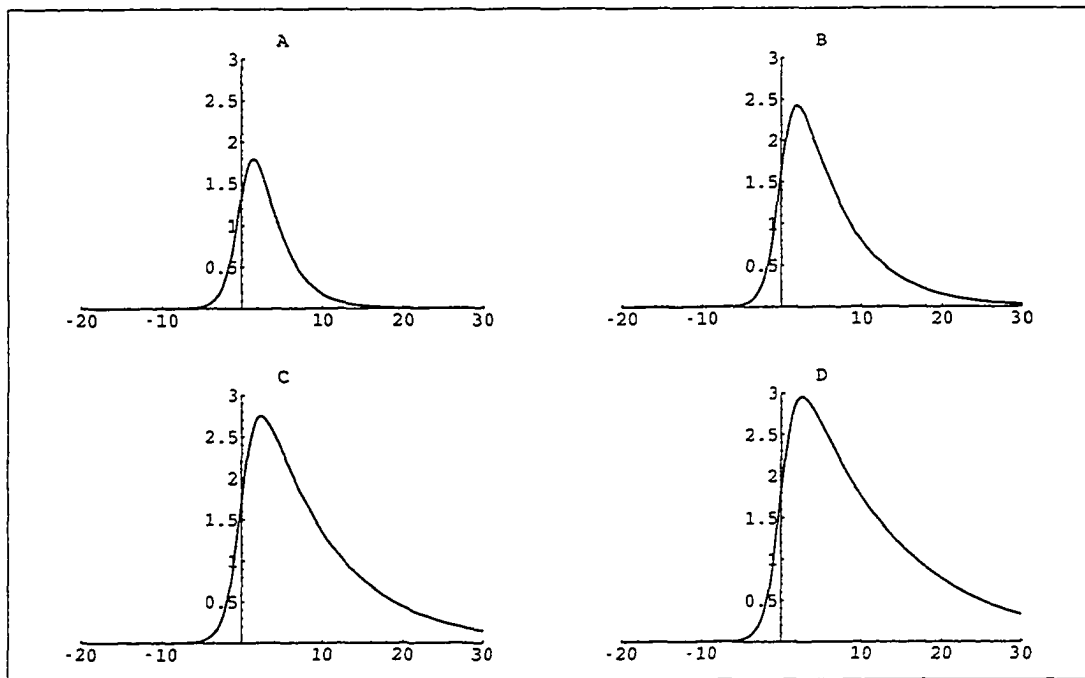
Figure 4.1: Electrical pulses with pulse widths(due to carrier recombination) a) 3 ps; b) 6 ps; c) 9 ps; d) 12 ps.

95

following approach. First it was rewritten in the form:

$$\frac{dI(t)}{dt} = \frac{1}{Z}\frac{dV(t)}{dt} - \frac{I(t)}{ZC_t} + \frac{V(t) - I(t)Z}{R_t ZC_t} \tag{4.8}$$

$$= \frac{1}{Z}\frac{dV(t)}{dt} - \frac{I(t)}{ZC_t} + \beta\left(\frac{(V(t) - I(t)Z) + \gamma(V(t) - I(t)Z)^3}{ZC_t}\right) \tag{4.9}$$

$$= y_0(t) + \beta y_1(t) \tag{4.10}$$

where $y_0(t)$ and $y_1(t)$ represent two components of the tunneling current. The AC component of the current is $y_0(t)$ and integrates to zero as no DC current can flow through a capacitor. The integral of the second component $y_1(t)$ is what we will concern ourself with. The factor β was removed from $y_1(t)$ so that it will be more comparable to $y_0(t)$ in magnitude and any comparative computations between the two will be less susceptible to errors. The differential equation for $y_1(t)$ is:

$$\frac{dy_1}{dt} = \frac{1}{Z}\frac{dV(t)}{dt} - \frac{y_1}{ZC_t} \tag{4.11}$$

Substituting $f_0 = V(t) - y_1 Z$ we get:

$$\frac{df_0}{dt} = \frac{V(t) - f_0}{ZC_t} \tag{4.12}$$

which can be solved in terms of hypergeometric functions. The equation for the integrated current which we are interested in can be expressed in terms of $V(t)$ and f_0 as:

$$\int_{-\infty}^{\infty} y_1(t) = \int_{-\infty}^{\infty} V(t)dt + \gamma \int_{-\infty}^{\infty} f_0^2(t)V(t)dt \tag{4.13}$$

This equation was solved by substituting the hypergeometric function solutions for $V(t)$ and then numerically integrating the right hand side of equation 4.13, using a 4th order Runge-Kutta solver. The limits of integration in equation 4.13 were chosen

96

far enough from the current pulse that its amplitude was negligible. By multiplying the integral by β we can recover the total charge transferred to the STM tip. This charge is acquired over the duty cycle of the laser, giving us a net contribution to the tunneling current. A Fortran program was written by Bob Teshima to evaluate the integrated current for different input parameters.

4.2 Publication

G. M. Steeves, A. Y. Elezzabi, R. Teshima, R. A. Said, and M. R. Freeman, *IEEE J. Quantum Electron.* **34**, 1415(1998).

Time-resolved scanning tunneling microscopy (TR-STM) will enable the study of dynamics in nanostructures on picosecond to femtosecond time scales. Scanning tunneling microscopes are used in atomic resolution studies of surface and electronic structure. These studies are often performed on materials found in semiconductor devices. With TR-STM, the ultrafast electrical dynamics of surfaces and devices can also be examined in a non-invasive fashion. For example, electron transport might be studied directly in single electron transistors or across a Coulomb blockade structure. Many techniques to add ultrafast time resolution to an STM have been proposed [4, 5, 6, 7, 8, 9, 10, 11]. Previous work has indicated that direct modulation of the STM tunnel junction may be the only way to maintain excellent spatial resolution in a time-resolved experiment. Two methods to directly modulate the junction have been proposed; varying the tip sample separation [5, 9] and electrically modulating the junction [4, 12, 13]. Of these techniques, electrical modulation is the only one, having the necessary speed for sub-picosecond time resolution. The electrical modulation of the STM tunnel junction for TR-STM is known as junction mixing scanning tunneling microscopy(JM-STM). Currently, JM-STM is the only time-resolved technique with demonstrated nanometer spatial resolution combined with picosecond temporal resolution [13].
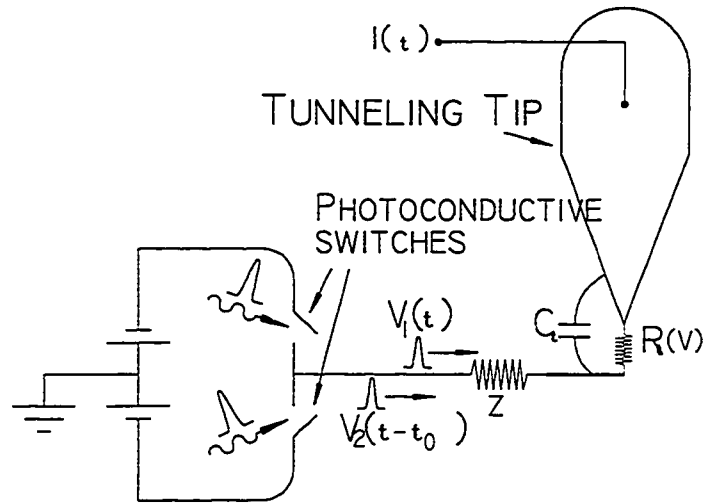
Figure 4.2: Equivalent JM-STM lumped RC circuit.

In an effort to further characterize the ultrafast operation of the JM-STM, a circuit model has been developed. Following the analysis of Groeneveld and van Kempen for another implementation of ultrafast STM [2], the JM-STM experiment is modeled as a lumped element RC circuit excited with ultrafast transient electrical pulses. With this circuit model we attempt to predict the ultrafast operation of the JM-STM, and support our predictions with previous experimental results.

The basic circuit is illustrated in Figure 4.2 [3]; it consists of two ultrafast photoconductive switches connected in parallel to each other and in series with a high-speed transmission line which has an impedance, Z. The switches are biased to a voltage V_0 and are triggered by laser pulses to launch the time-dependent electrical pulses $V_1(t)$ and $V_2(t - t_0)$. Coupled to the transmission line is the RC part of the circuit that describes the STM tunnel junction. The tunnel junction impedance is modeled as a non-linear resistance, $R_t(V)$. A vital parameter to the model calculation is the magnitude of the geometrical capacitance between the tip and the microstrip line.

---

[3]The published work presented here, originally included a different version of this figure. In the publication, an additional impedance Z, passing current to ground, was included on the transmission line after the STM tip. The calculations presented in this chapter and in the publication did not include this additional impedance. The affect of this impedance has been explored in Appendix C.

The magnitude of this capacitance is difficult to measure directly since it is typically in the fF range [2]. Most calculated values of the capacitance break down in the tunneling region where they diverge for small tip/sample separation. It is not clear exactly how capacitance will scale as the tip/sample separation approaches zero in a normal tunneling experiment (S. Kurokawa and A. Sakai have examined this problem in great detail [14, 15]). To approach this problem, the method of images was used to calculate the capacitance for a range of tip/sample separations down to 2 nm. These results were fit and then extrapolated into the tunneling regime by approximating the tip as 2 parallel plate capacitors with different separations and effective areas. The STM tip geometry used in the initial image calculation resembles the experimental STM tip geometry and is shown in the inset of Figure 4.3. The capacitance C_t is evaluated by calculating the induced surface charge distribution due to the applied electric potential.

The electrostatic potential for a surface charge of density $\sigma(\vec{r_0})$ over a ground plane can be expressed in terms of the static integral equation

$$\phi(\vec{r}) = \left(\frac{1}{4\pi\epsilon_0}\right) \int \int_S \sigma(\vec{r_0}) \left[\frac{1}{|\vec{r} - \vec{r_0}|} - \frac{1}{|\vec{r} - \vec{r_0}'|}\right] dS \qquad (4.14)$$

where $\phi(\vec{r})$ is the potential at distance $\vec{r}$ from the origin, $\vec{r_0}$ is a point on the conducting surface, ϵ_0 is the permittivity of free space and dS is the surface element. The ground plane is replaced by an image of the real charge distribution located at $\vec{r_0}'$ and the moment method [16] is used to solve the integral equation. Once the surface charge distribution is calculated, the capacitance is evaluated as the ratio between the induced charge on one of the two surfaces and their potential difference.

The solid points in Figure 4.3 show the results of these capacitance calculations evaluated at a variable tip height range between 2 - 21 nm where the minimum separation is limited by the element size used in the calculation. To extend this down

99
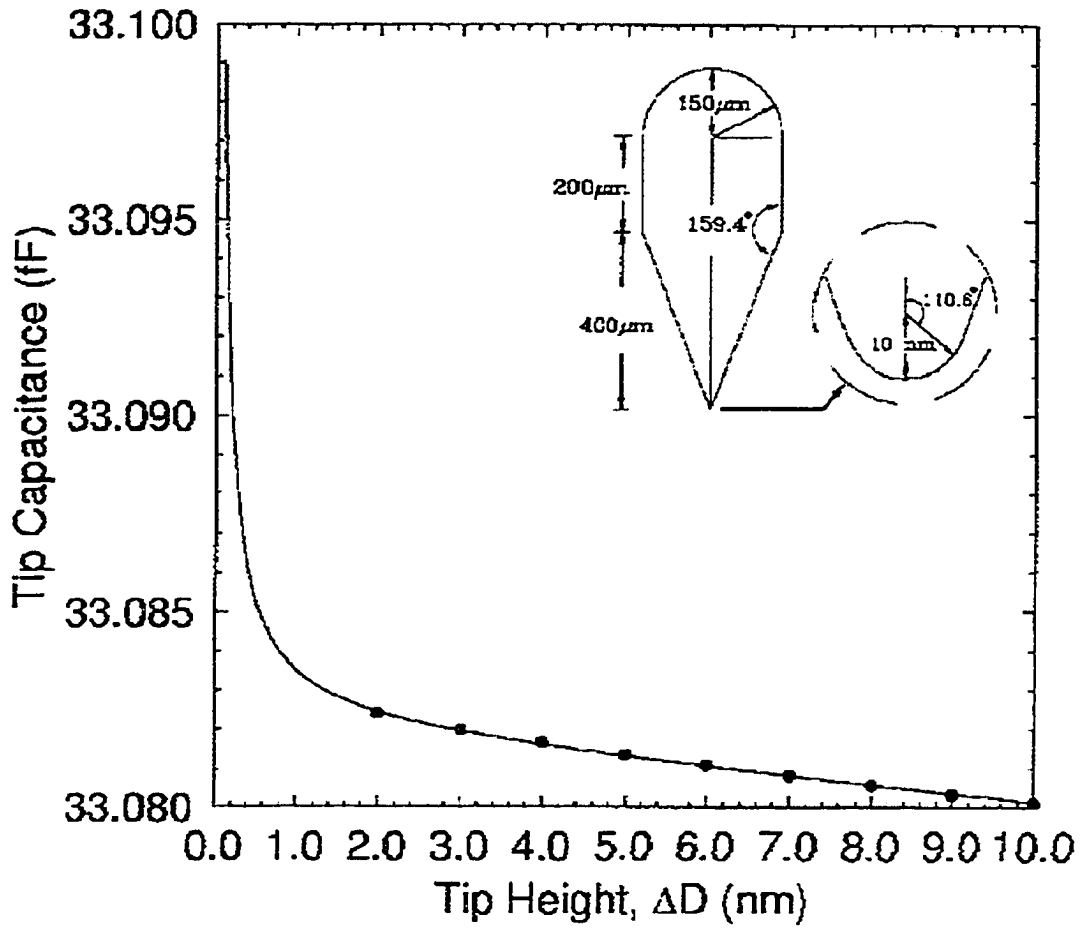
Figure 4.3: Calculated tip-transmission line capacitance as a function of STM tip height above the transmission line. Inset schematically shows the tip geometry used in the calculations.

100

to separations of fractions of a nanometer, used in tunneling, the calculated points
are fit to the expansion:

$$C = \frac{\epsilon_0 A_1}{D}\left(1 - \frac{\Delta D}{D} + \cdots\right) + \frac{\epsilon_0 A_2}{\Delta D} \tag{4.15}$$

The shank and taper of the probe behave as a parallel plate of effective area A_1 at
a distance D to the sample. The probe tip has an effective area A_2 and $\Delta D (\ll D)$ is
the tip sample separation. The fit shown by the solid line in Figure 4.3 corresponds
to parameters $A_1 = (776.271 \mu m)^2$, $A_2 = (13.8874 nm)^2$ and $D = 161.281 \mu m$. Over
a height range from 0.2 to 20 nm the capacitance only changes by one part in 10^3,
so we treat it as a constant with value 33 fF. This result also shows that changes
in capacitance as the tip scans over the surface will have negligible influence on the
time-resolved signal from topographic variations.

The pulse induced tunneling current $I(t)$, developed on the STM tip, is calculated
by integrating the following differential equation:

$$\frac{dI(t)}{dt} = \frac{1}{Z}\frac{dV(t)}{dt} - I(t)\left(\frac{1}{ZC_t} + \frac{1}{R_t C_t}\right) + \frac{V(t)}{R_t Z C_t} \tag{4.16}$$

where $V(t) = V_1(t) + V_2(t - t_0)$ is the sum of the voltage pulses delivered by the two
ultrafast photoconductive switches and t_0 is the delay time. The time dependence of
each voltage pulse can be evaluated from a convolution between the excitation laser
pulse temporal shape and the temporal response of the photoconductive switch:

$$V_1(t) = V_0 \int_{-\infty}^{t} \sec h^2\left(\frac{\tau}{t_p}\right)\exp\left(\frac{\tau - t}{t_c}\right)d\tau \tag{4.17}$$

and

$$V_2(t - t_0) = V_0 \int_{-\infty}^{t - t_0} \sec h^2\left(\frac{\tau}{t_p}\right)\exp\left(\frac{\tau - (t - t_0)}{t_c}\right)d\tau \tag{4.18}$$

101
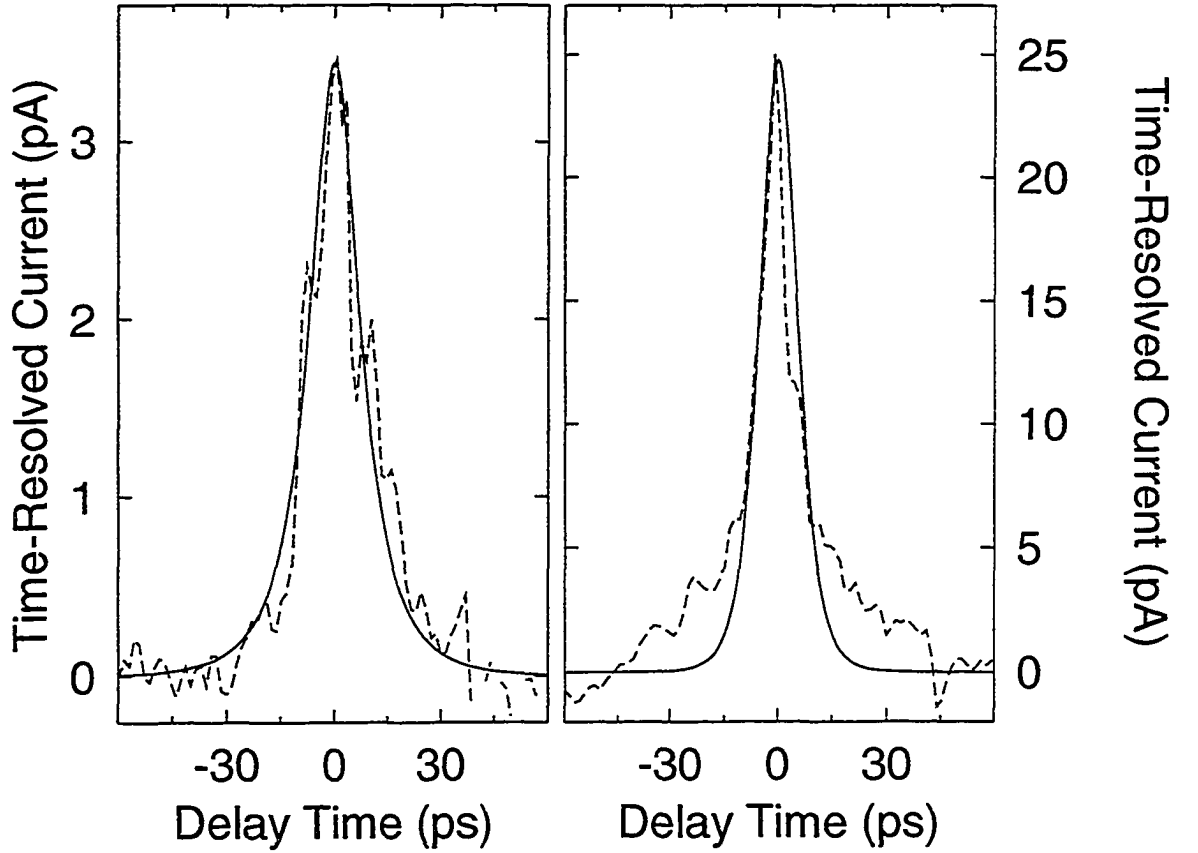
Figure 4.4: Time-resolved tunneling currents. Experimental data is indicated by dashed lines, model calculations are represented by solid lines. Left panel shows data for a 10 ps voltage pulse, right panel shows data from a faster 4ps pulse.

where t_c is the electro-optic switch carrier recombination time, t_p is the laser excitation pulse width. The tunnel junction non-linear resistance is given by:

$$R_t(V) = \frac{1}{\beta(1 + \gamma(V(t) - I(t)Z)^2)} \tag{4.19}$$

where, β and γ are the linear and non-linear tunneling conductances of the tunnel junction, respectively and Z is the line impedance. The excitation laser pulses illuminate the photoconductive switch gaps at times $t = 0$, and $t = t_0$.

Comparisons of the circuit model with experimental results are shown in Figure 4.4. For the left panel, calculations are performed using a $V_0 = 0.49V$ voltage pulse and the 10 ps JM-STM experimental conditions presented in reference [12] ($\beta = 5.1$ nS, $\gamma = 0.75V^{-2}$ for the Au surface, $Z = 68\Omega$, $C_t = 33$ fF, $t_c = 10$ ps , and $t_p = 2.8$ ps).

102

We have numerically integrated equation 4.16 over the time interval -100 ps $< t < 100$ ps to calculate the pulse induced current. Since our experimental apparatus measures a time- resolved signal which is averaged over the duty cycle of the laser, it is necessary to scale the pulse induced current in a comparable manner. The model calculation and the experimental result are in excellent agreement. To further test the model, we have used new samples with faster photoconductive switches to push the temporal response of the STM to the limit of our laser pulse width (2.8 ps). By using the measured values of $\beta = 23$ nS, $\gamma = 1.3V^{-2}$, $t_c = 4.5$ ps , and $t_p = 2.8$ ps, and a capacitance $C_t = 33$ fF, we repeated the calculation for a $V_0 = 0.561$ V voltage pulse along a transmission line with impedance $Z = 68\Omega$. Again, the calculated and measured 4.5 ps JM-STM response (9-ps correlation width) are in good agreement(right panel). The difference in amplitudes between the right and left panels is due to the different Au surface conditions used in experiments (an unfortunate consequence of ambient tunneling) and the different pump/probe pulse widths. The discrepancy in the curve tail between the model and the experiment is attributed to the non-ideal electrical pulse shape in the measurements from reflections and dispersion.

Considering the effect of C_t on the output of the model (i.e. variations of the tip-sample geometry) we performed the same calculations over a wide capacitance range, between 0.1 and 110 fF. Figure 4.5 illustrates the time-resolved waveforms as a function of pulse separation time, calculated using 200 fs laser pulse widths and a switch carrier recombination time of 1 ps. For $C_t < 1$ fF the effect of C_t on $I(t)$ is quite small and the time-resolved signal is essentially independent of capacitance. Inset in Figure 4.5, is a plot of the correlation pulse width (FWHM) as it varies with capacitance for a 1 ps pulse. This plot is roughly linear in our region of interest (33 fF).
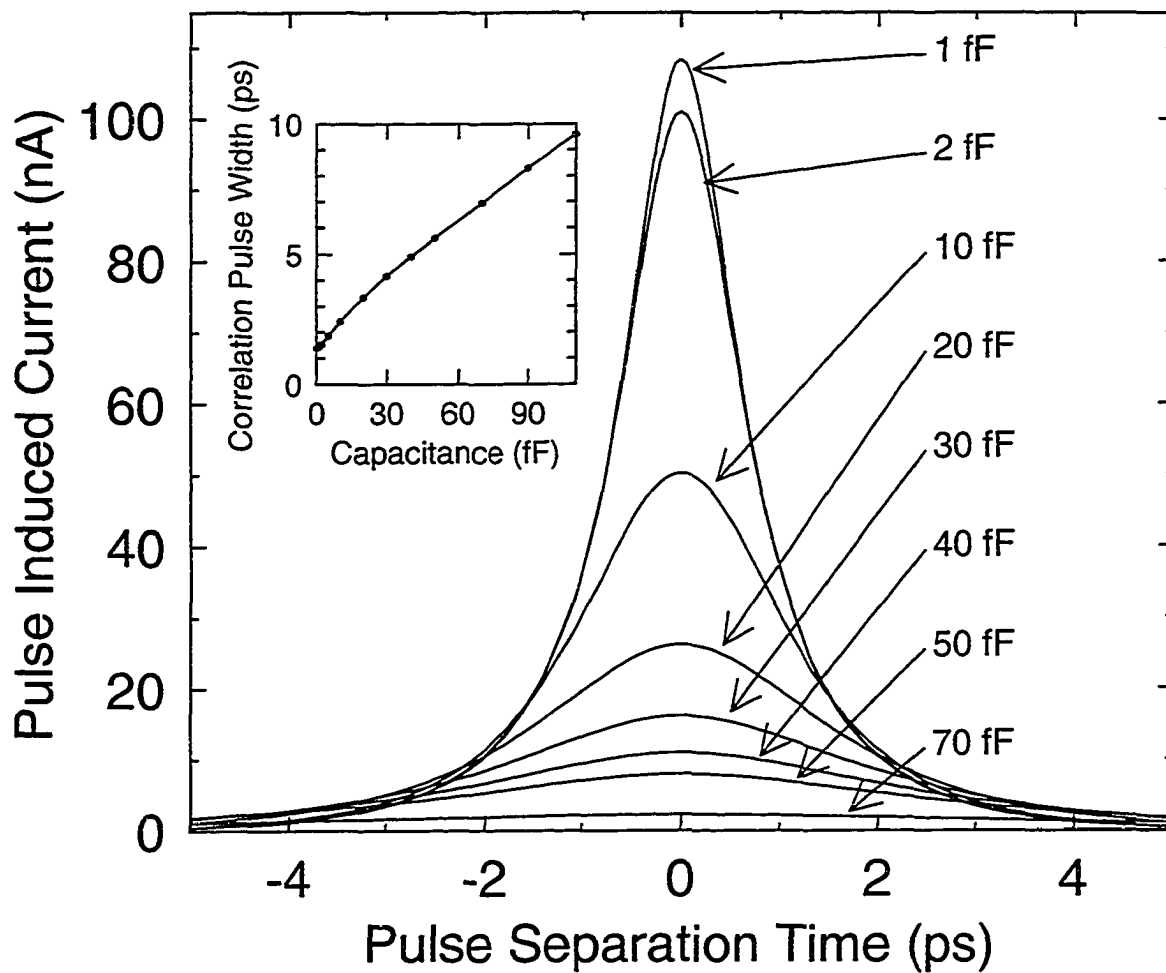
Figure 4.5: Tunneling junction current time-resolved signals for different tip-transmission line capacitance. Inset shows the width of the correlation pulses as the capacitance is varied. Model parameters are: $\beta = 23$ nS, $\gamma = 1.3V^{-2}$, $V_0 = 1$ V, $t_c = 1$ ps, and $t_p = 200$ fs.

104
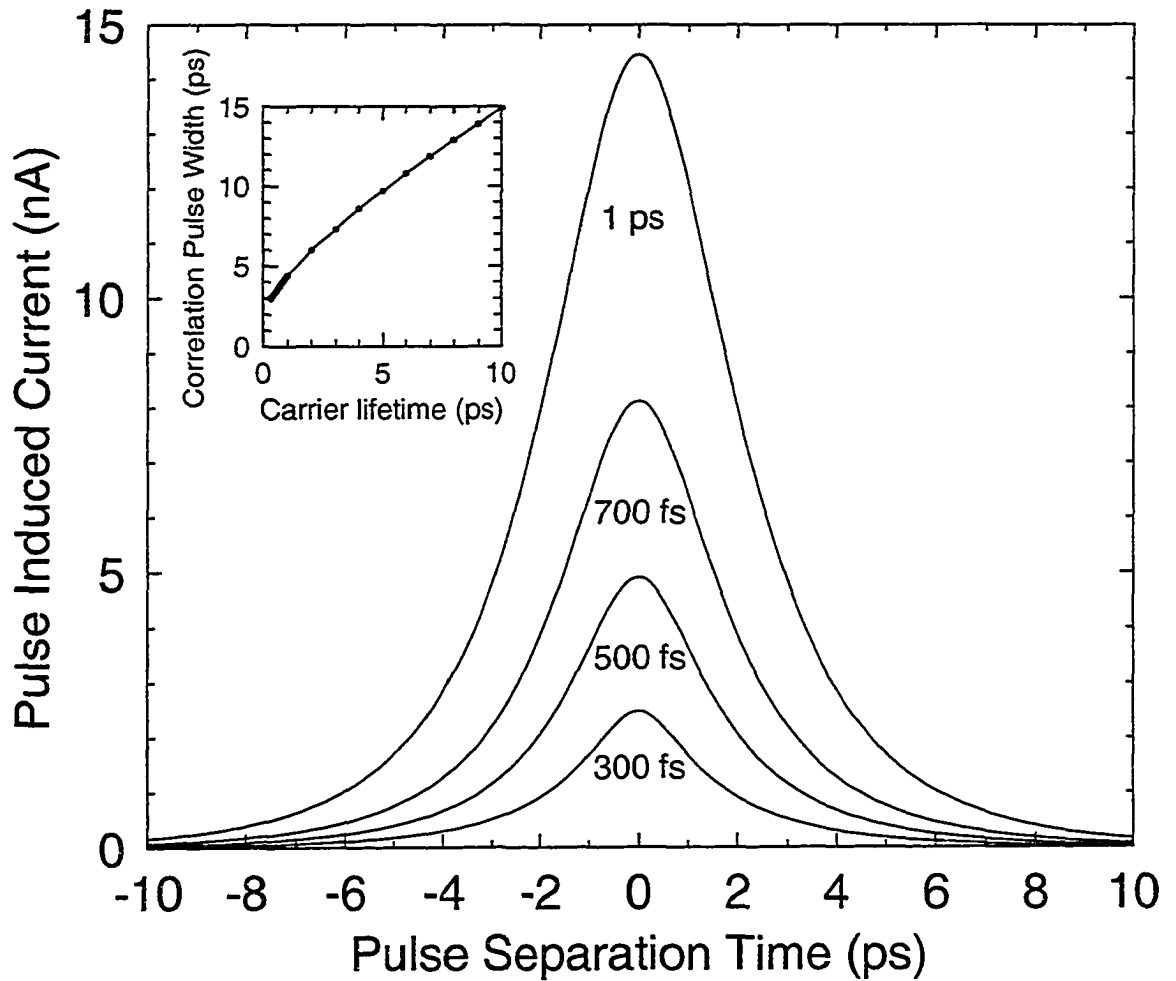
Figure 4.6: Calculated time-resolved tunneling current for various electrical excitation pulses. Inset shows the width of the correlation pulses as the width of the voltage pulse along the transmission line is varied. Model parameters are: $\beta = 23$ nS, $\gamma = 1.3V^{-2}$, $V_0 = 1$ V, $C_t = 33$ fF, and $t_p = 200$ fs.

Of interest is the performance of the JM-STM in the femtosecond range. Simulations were carried out for various switch carrier recombination times (300 fs to 10 ps). Figure 4.6 shows the results from the calculations and the inset shows the dependence of the correlation pulse width(FWHM) as the carrier recombination time is varied.

The capacitance is fixed at 33 fF. For carrier recombination times under 1 ps, the correlation pulse width falls off quite slowly making it difficult to push the time resolution further without first reducing the tip-sample capacitance below 33 fF.

105

The lumped-element circuit model described above seems sufficient to describe the operation of a JM-STM in the picosecond time regime. The validity of the model itself must also be considered more closely if we are to move into the femtosecond domain. As measurement speeds increase, the wavelengths of pump and probe electrical pulses become comparable to the characteristic length scales of tip/sample interactions, at this point the lumped-element model will not perform well.

In summary, we have presented a simple circuit model describing the ultrafast operation of a JM-STM. Using the laser and electrical pulse parameters and the experimentally determined values for β and γ, we found the results of the model are in very good agreement with experiment. The effect of increasing the capacitance between tip and sample was to reduce the magnitude of the pulse induced current while increasing the width of the time-resolved pulse. By investigating the effect of shorter voltage pulses we see that JM-STM, at pulse widths less than 1 ps, can be achieved only when the capacitance between tip and sample is reduced below 33 fF. The limitations in response time of the JM-STM are caused by the capacitive loading of the tip which reduces the effective voltage across the tunnel junction resistor $R_t(V)$. To better understand the operation of a JM-STM in the femtosecond regime a more complete electromagnetic model should be developed.

References

[1] G. M. Steeves, A. Y. Elezzabi, R. Teshima, R. A. Said, and M. R. Freeman. *IEEE J. Quantum Electron.*, 34:1415, 1998.

[2] R.H.M. Groeneveld and H. van Kempen. *Appl. Phys. Lett.*, 69:2294, 1996.

[3] Ra'a A. Said. *Scanning Force Potentiometry Techniques for Semiconductor Circuit Characterization.* PhD thesis, University of Manitoba, 1995.

[4] Geoff Nunes, Jr. and M. R. Freeman. *Science*, 262:1029, 1993.

[5] M. R. Freeman and Geoff Nunes, Jr. *Appl. Phys. Lett.*, 63:2633, 1993.

[6] S. Weiss, D. F. Ogletree, D. Botkin, M. Salmeron, and D. S. Chemla. *Appl. Phys. Lett.*, 63:2567, 1993.

[7] S. Weiss, D. Botkin, D. F. Ogletree, M. Salmeron, and D. S. Chemla. *Phys. Status Solidi B*, 188:343, 1995.

[8] R. H. M. Groeneveld, Th. Rasing, L. M. F. Kaufmann, E. Smalbrugge, J. H. Wolter, M. R. Melloch, and H van Kempen. *J. Vac. Sci. Tech. B*, 14:861, 1996.

[9] T. Hesjedal, E. Chilla, and H.-J. Frohlich. *Appl. Phys. Lett.*, 69:354, 1996.

[10] W. Pfeiffer, F. Sattler, S. Vogler, G. Gerber, J. Y. Grand, and R. Moller. *Appl. Phys. B*, 64:265, 1997.

[11] G. Chui and J. M. Halbout. *US patent*, No. 5,019,707.

[12] G. M. Steeves, A. Y. Elezzabi, and M. R. Freeman. *Appl. Phys. Lett.*, 70:1909, 1997.

[13] G. M. Steeves, A. Y. Elezzabi, and M. R. Freeman. *Appl. Phys. Lett.*, 72:504, 1998.

[14] S. Kurokawa and A. Sakai. *Sci. Rep. RITU*, 44:173, 1997.

[15] S. Kurokawa and A. Sakai. *accepted for publication in J. Appl. Phys.*, 83, 1998.

[16] R. F. Harrington. *Field Computation by Moment Method.* Macmillan, New York, 1968.

Chapter 5

Design and Development of a Low Temperature High Vacuum STM with Optical Access

5.1 Introduction

Following the development of the junction mixing time-resolved STM technique, efforts began to demonstrate this technique on one of the real world problems that triggered interest in the method, nonequilibrium superconductivity. The proposed system of study was the superconducting vortex state in $NbSe_2$. Imaging of the vortex state using an STM was first accomplished by Hess et al. [1] as shown in Figure 1.4. The goal here is to image vortex state dynamics using JM-STM, by transiently suppressing superconductivity using ultra-fast optical pulses. This goal has not yet been met. In order to image the vortex state, it was necessary to develop a new ultrafast, low temperature, high vacuum STM system. The design, development, and implementation of this system will now be discussed.

The initial microscope design was based on a microscope constructed by Dhirani, Fisher and Guyot-Sionnest [2]. The design and development process has been ongoing. All elements incorporated into what is currently the "final" design have been modified and refined on a continuing basis as required. For this discussion we will focus on 3 key factors in microscope design; the mechanical and electrical designs of the microscope,

Reproduced with permission of the copyright owner. Further reproduction prohibited without permission.

including the vibration isolation system and the entire electrical system down to the power supplies for all necessary STM electronics; and the environment of the tunneling head-shell of the microscope, specifically the vacuum system developed to allow the microscope to function at cryogenic temperatures and with optical access for pump/probe or laser ablation experiments. For each of these topics, the operational requirements will be outlined as they were predicted and discovered experimentally.

5.2 Mechanical Design

The mechanical design of the STM was driven by the need to eliminate vibrational coupling to the tunnel junction of the microscope. This consideration led us to choose very specific materials for the construction of the microscope, along with an elaborate vibration isolation system. The overall vibration isolation objective is to decouple the head shell from all environmental vibrations. Since this objective cannot be met in a terrestrial environment we attempt to isolate the head shell from all vibrations greater than 1 Hz. If this can be done, the next requirement is to design the STM head shell to be very rigid, such that oscillations below 1 Hz will move the entire head shell in unison, allowing no relative motion between STM tip and sample. In this way we can achieve the stability necessary for atomic resolution.

Figure 5.1 illustrates the main features of the present vibration isolation system. Resting on the floor of a basement laboratory are cylindrical steel legs filled with 100 lbs of sand each. Resting on top of the sand in each leg is a top plate. These plates support a pneumatic table. The pneumatic table supports a series of 4, 200 lb steel plates and each plate is separated by pads of ISODAMP C-1002 blue vinyl damping material [1]. The center of each plate has been cut out to allow the STM to be lowered through the plates until the top of the microscope rests on the top of the uppermost plate. The microscope hangs from the top of the plates into a liquid

---

[1] EAR Specialty Composites (877)327-4332

109
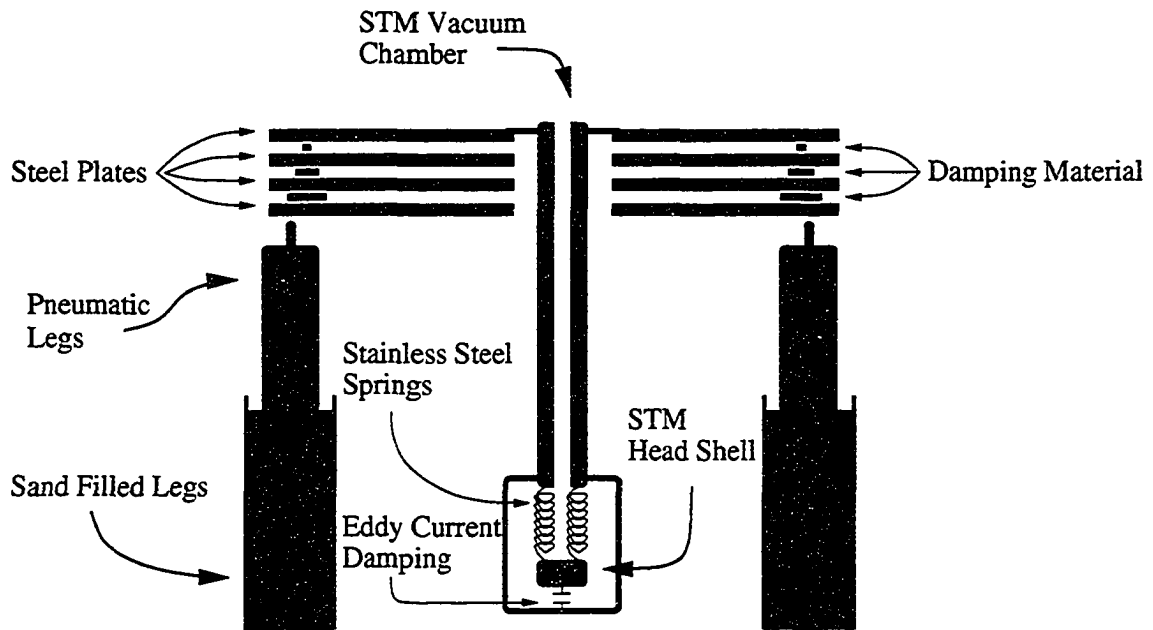
Figure 5.1: STM vibration isolation system.

helium dewar. Vibrations in the helium dewar are decoupled from the microscope and plates, through a flexible 60 section edge welded bellows. The head shell of the microscope hangs from the body of the microscope from three pretensioned stainless steel springs, and eddy current damping is used between the hanging head shell and the vacuum can (surrounding the head shell) to dissipate head shell motion. From the calculations of Nagaya [3] the damping force between a copper block of thickness t and area $b \times d$ next to a cylindrical magnet with field B and area πa^2 is:

$$F_x = -C_0 \left(\frac{B^2 \pi a^2 t}{\rho} \right) v_x, \qquad (5.1)$$

where v_x is the relative velocity between the copper block and the magnet, and ρ is the resistivity of the copper. C_0 is a dimensionless geometrical constant which is given in [3] for various ratios of a, b and d. In the case where $b, d \gg a$ the constant becomes $C_0 = 0.5$. Stainless steel springs were chosen as they are non-magnetic and could be pretensioned more than beryllium copper springs(a more common spring material for non-magnetic applications).

110

This vibration isolation system developed through a number of iterations with support from references such as Chen's textbook [4]. Initial low temperature STM designs consisted of the microscope head shell hanging on beryllium copper springs from a short 10" platform which rested on the bottom of the cryostat. Trials with this configuration were unsuccessful as the boiling of liquid nitrogen in the cryostat caused sufficient vibrations to disrupt STM measurement. In order to achieve better decoupling from these vibrations, the 1 stage decoupling system was replaced with a 2 stage system which was suspended from the top of the cryostat. This system had a set of springs suspending a copper weight from which 3 more springs hung to support the STM head shell. The intermediate copper weight sported 3 permanent magnets around its exterior. A copper ring, friction mounted within the column of the cryostat damped the motion of the copper weight through the eddy current damping mechanism. This isolation system was much better than its predecessor but still insufficient for stable tunneling. The problem was that the microscope was still directly coupled to the cryostat as it was hanging from the top of the cryostat. These factors forced us to consider an isolation system in which the microscope was decoupled from both mechanical resonances in the building and from boiling induced oscillations in the cryostat. Hence we settled on the current scheme of hanging the microscope from a vibration isolation table, into the cryostat.

The rigid STM head shell was constructed using a heavy ($\approx$ 700 grams) oxygen free high conductivity(OFHC) copper puck. Copper was used due to its density, electrical and thermal conductivity and compatibility with high vacuum applications. An L-shaped bracket is screwed onto the top of the puck to support the STM tip assembly and a circular cut out on the top of the puck accommodates the STM approach assembly. This modular design allows us to easily replace or modify the approach and scanning assemblies without re-machining the head-shell. The tip and approach assembly are fixed to the head shell using set screws, machined along one

111
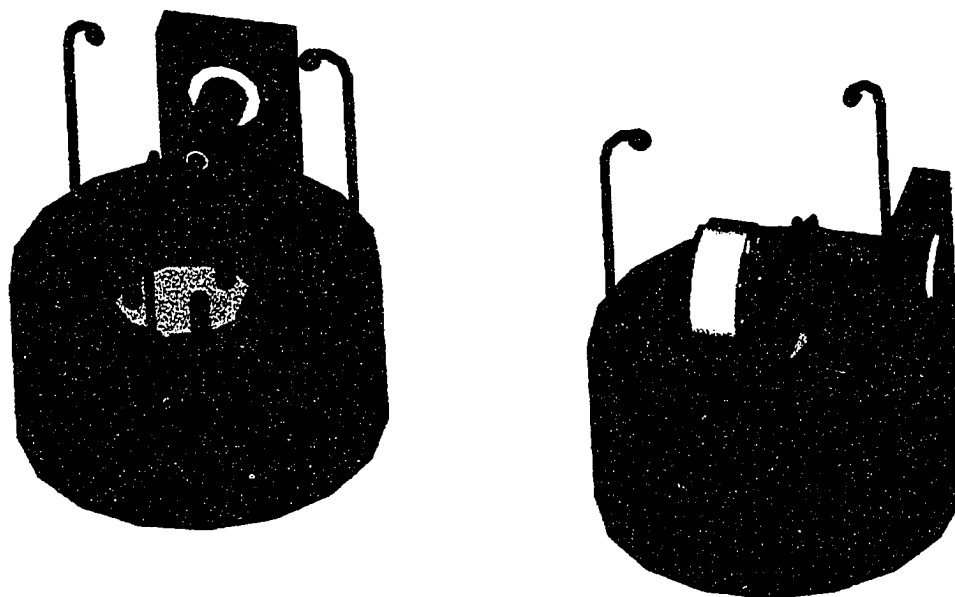
Figure 5.2: STM head shell(2 views): OFHC copper mass, tip assembly, approach assembly and the sample sled(in right view only).

edge to eliminate trapped air pockets. An array of tapped holes was machined into the copper puck to allow wiring and other devices such as a low temperature thermometer to be fastened down to the head-shell. The copper puck, tip assembly and approach assembly are shown in Figure 5.2.

The approach assembly can be seen in the left view of Figure 5.2. This assembly consists of a white macor disc with 3 short piezo tubes($\frac{1}{8}$" OD) glued into the disc. Macor is a machinable ceramic material produced by Dow Corning, which is very rigid and an excellent electrical insulator. The tops of the piezo tubes are capped with ruby balls, to provide a hard smooth surface for the sample sled to rest on. The whole assembly is fixed into the copper puck by means of 2 set screws. The base of the sample sled is made of polished sapphire for its hardness and smooth surface. The

rising edge of a sawtooth voltage waveform, applied to the supporting piezos causes them to all bend relative to the STM tip. This in turn moves the sled relative to the tip as the sled is fixed to the ruby balls by a static frictional force. On the sharp falling edge of the sawtooth waveform, the support piezos snap back to their initial position. This fast snap back leaves the sample sled in its displaced position as the kinetic frictional force is insufficient to bind the sled to its support. This approach mechanism is akin to the old parlor tricks with glasses and a table cloth.

Typically the base piezos have gold electrodes, sectioned axially into four quadrants. A positive sawtooth voltage would be applied to one side of the piezo and the inverse negative waveform applied to the opposing electrode. As each piezo has 4 sections, the sled can be translated towards or away from the tip assembly as well as in both directions laterally. Sapphire bumpers are shown on either side of the sled to protect against lateral drifts during an approach, and to keep the sled from falling off the puck during routine handling. Front and back stops are also incorporated onto the puck using threaded steel rod. This support system provided a rigid mount for the sled. In order to further improve the frictional coupling between sled and puck gold weights were added to the sled to weigh it down. Gold was used as space was limited and the density of gold(twice that of lead) allowed us to maximize sled mass. The original use of this tripod approach mechanism utilized a magnetic clamp between sled and puck to increase mechanical coupling. The present microscope could accommodate such a clamp, but the desire to keep the microscope non-magnetic was a higher priority.

The sled consists of a macor disc glued to a large sapphire window(using TRA-BOND's BA-2151 adhesive, [2] the best adhesive we have found for bonding sapphire to ceramics). A 1.22 Tesla neodymium iron boron magnet is embedded into the macor disc to provide a permanent biasing field to create vortices in our superconducting $NbSe_2$ samples. Gold plated electrical connectors are also glued into the macor to

---

[2]TRA-BOND (800)872-2661

113

provide electrical connections to the sample of interest. All wiring to the sled is done using 46 gauge(0.0024" diameter green insulation surrounding a 0.0016" copper core) wire to minimize mechanical coupling to the sample. The upright macor piece of the sled is large enough to accommodate $7 \times 7 \times 0.5$ mm wafers so that patterned transmission line structures can be mounted next to the sample on the sled, for time-resolved measurements.

The STM tip assembly is shown from 2 views in Figure 5.2 and in pieces in Figure 5.3. A cylindrical macor tube is mounted into the copper L-bracket on the copper puck. At the back end of this macor tube we glue the main STM scanning piezo tube($\frac{1}{4}$" OD). Care must be taken when gluing so that glue is applied to individual piezo sections and the macor, never bridging 2 sections. A maximum potential of 900 V could be applied between two adjacent piezo sections and the torr seal glue will break down. Macor is an excellent insulator which we have never seen break down. The inner and outer surfaces of the tube are gold coated(to achieve maximum piezo mechanical response per applied volt use a thinner conducting material). The outer surface is sectioned into 5 pieces as shown on the right in Figure 5.4. Original low temperature microscopes were developed using tubes sectioned as shown on the left, but as the response of a piezo tube decreases by a factor of 6 at liquid helium temperatures the voltages necessary to achieve acceptable scan ranges exceeded the depoling limit of the piezo tubes. Depoling can occur if the potential difference between adjacent surfaces of the piezo tube exceed a threshold value. The critical potential does depend on how the piezo tube was originally made. Typical depoling fields are on the order of $5 \rightarrow 10$ Volts/mil of wall thickness against the pole direction or about 20 V/mil with the poling direction(where 1 mil $= \frac{1}{1000}$ inch). At low temperatures this depoling field is expected to scale inversely with d_{31} so that we can use 6 times higher voltage at liquid helium temperatures. When scanning a tube sectioned as shown on the left, the scan voltages can swing between $-450 \rightarrow 450$ V and

114
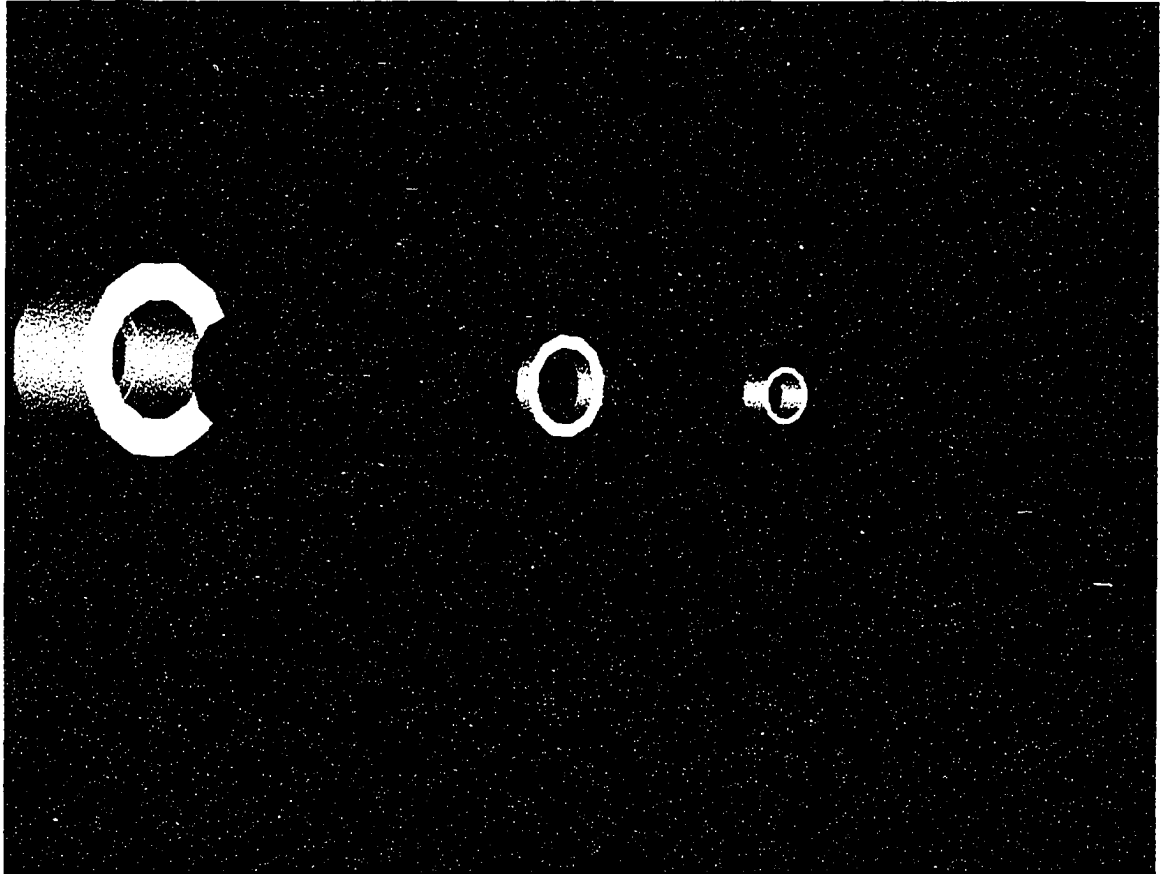
Figure 5.3: Exploded view of STM tip assembly.

115
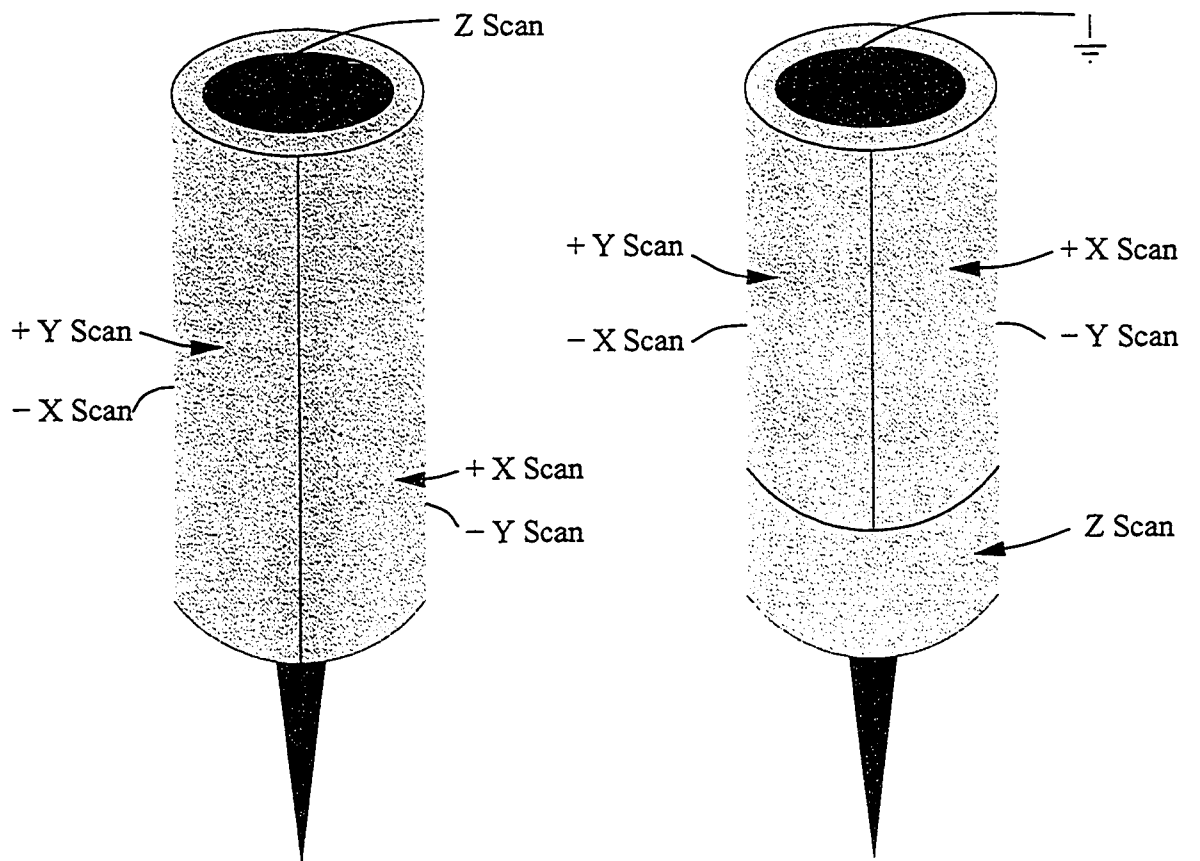
Figure 5.4: Tube scanner sectioning arrangements.

116

the feedback voltage(for a rough or tilted surface) could span over that same range. This could potentially produce potential differences of 900 V between the inner and outer piezo surface. The configuration shown on the right eliminates this possibility as the center of the piezo is kept at ground and the biggest potential across the tube is limited to the maximum output of the high-voltage supply, 450 Volts. Keeping the central conducting surface of the piezo tube grounded also provides shielding for the electrical connections to the STM tip, which run through the center of the piezo.

Close inspection of the STM tip assembly illustration in Figure 5.2 shows the STM tip inserted(friction fit) into a copper sleeve. This copper sleeve is soldered to the STM tip lead which runs the length of the piezo tube and out the back to an anchor point on the copper puck. Surrounding this copper sleeve is a macor sleeve, which insulates the tip from the outer conical tip shield. The outer tip shield is made of copper and serves to shield the STM tip from stray electric fields from the piezo. The shape of the shield was dictated by the need for optical access onto the STM sample. The shield is electrically grounded to the same potential as the braid which shields the STM tip lead in a co-axial cable right up to the current pre-amplifier outside the microscope. This outer copper shield is insulated from the voltages on the piezo tube using another macor insulating sleeve. The last curious feature of the STM head shell are the three hooks(resembling light posts) which attach the head shell to its support springs. The support springs are fastened to the tops of the hooks, and are bonded with a small dab of glue such that when the springs move there is no rubbing between the springs and the hooks.

Mechanical resonances are the main source of noise in the microscope. The microscope is not yet entirely rigid enough: we still need to increase one fundamental resonant frequency of the microscope above the response of the electronics.

117

5.3 Electrical Systems

Examination of the STM electronics system is motivated by the desire to eliminate crosstalk from the piezo electronics, so that stray voltages do not induce any mechanical response from the STM feedback system including the bias voltage, STM tip lead. Many of the noise reduction techniques implemented in the microscope design were modeled after techniques outlined in "Noise Reduction Techniques in Electronic Systems" by Henry W. Ott [5] and "Grounding and Shielding Techniques in Instrumentation" by Ralph Morrison [6]. Noise reduction efforts began with the power supply for whole STM system. The 120V 60 Hz line voltage is heavily filtered and then isolated from the building ground. Building grounds are often quite noisy and when used as signal shields can introduce significant noise onto small current signals. A separate ground, just north of the lab, was used solely for the experiments presented here. [3] This separate ground is brought into the lab and connected to a large copper block, which acts as the single point(star) ground for all the electronics, and shielding of the STM. Using this separate ground for the electronics keeps ground noise from interfering with sensitive current measurements. Using a single point ground for shielding should reduce the risk of forming ground loops in the wiring. The essential element of a properly shielded wire is a fixed ground at one end of the wire and a floating unterminated end of the shield. If the other end of the shield is accidentally grounded, changing magnetic flux through the shield loop induces currents which can couple to the inner signal carrying wire(the dreaded ground loop).

The electronics necessary to control the STM were a PC, and RHK Technology electronics including a SPM 100 digital STM feedback controller, an IVP 300 2 stage current pre-amp and an HVA 900 high-voltage amplifier. These devices were all powered through the cleaned isolated 120 V power supply. The SPM 100 supplies

---

[3]Care should be taken when operating devices in close proximity which are referenced to different ground points. Should lightning strike near one ground, it could arc across the lab to the other ground.
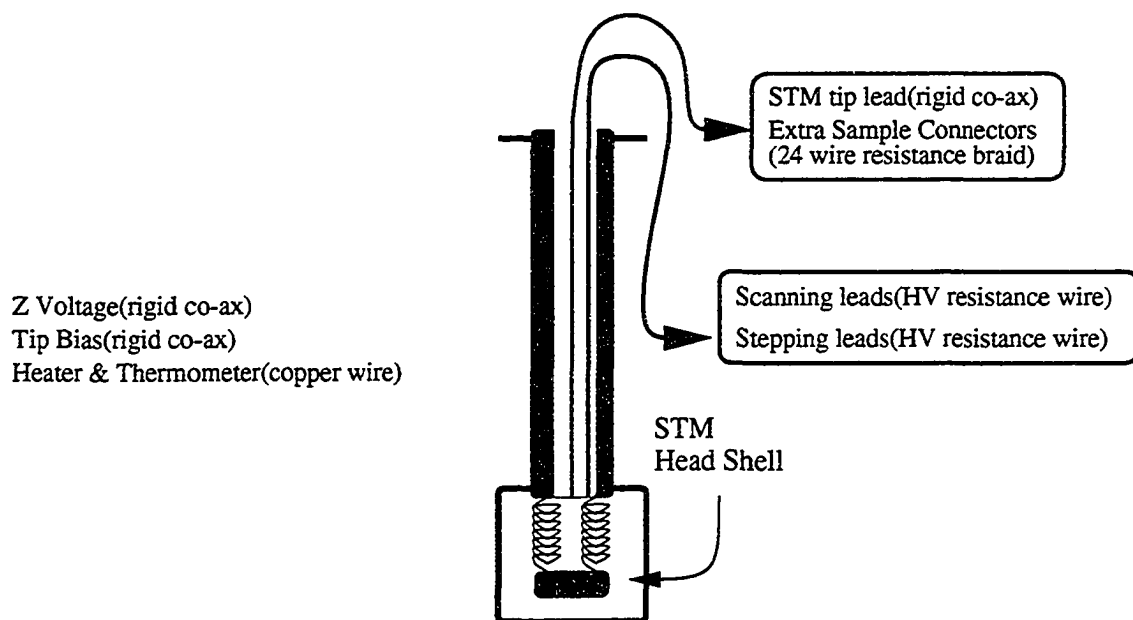
Figure 5.5: Wiring layout for each vacuum tube of the STM

the STM bias voltage, the course approach sawtooth voltage pulses, the STM X-Y scanning voltages and the Z control voltage. The IVP 300 amplifies the STM tunneling current by $10^9 A/V$ and feeds the amplified signal into the SPM 100. The HVA 900 can be used to optionally amplify the high voltage outputs of the SPM 100 for the low temperature operation of the microscope where high voltages are required as piezo response is reduced. Low noise co-axial cable is used for all the external cabling between the SPM 100, the HVA 900 and the microscope to reduce tribo-electric noise. Wiring between the IVP 300 and the SPM 100 is provided by a specially shielded cable, and the first stage of the IVP 300 is rigidly attached to the top of the microscope. This positions the first stage of the pre-amp as close to the STM head shell as possible while providing maximum shielding and rigidity to minimize tribo-electric noise.

Wiring from the top of the microscope up to the head shell is outlined in Figure 5.5. All wiring is either through rigid co-ax cables or twisted pairs to provide additional shielding. The wiring is brought through the body of the microscope to the head shell

119

via three stainless steel tubes. These tubes help to electrically isolate different groups of wires. The wiring in each tube was chosen to isolate the most sensitive signals from active and less sensitive lines. The STM tip lead is completely isolated from the STM bias lead, and especially from the feedback voltage signal. This ensures that the only coupling between tip current signal and the feedback voltage occurs at the tunnel junction of the microscope. The only additional voltage lines accompanying the tip lead are for optional bias voltages on the STM sample. If used these lines would only carry DC voltages. The semi-rigid co-axial cable used to shield the tip, feedback voltage, and the primary bias voltage is based on miniature stainless steel tubes. This helps to eliminate tribo-electric voltages which would add noise to the system. Wiring connections between the bottom of the three electrical conduit tubes and the head shell are made using three connectors. With the exception of the solid co-ax, the same types of wire used in the conduit tubes are continued through the last stage connectors down to the head shell. The flexibility of wiring used in the last connectors is sufficient that mechanical oscillations transmitted through the wiring cannot drive the head shell. The solid co-ax tubes are replaced, in the connector, with thin stainless steel co-axial cables, coiled into springs, to minimize mechanical coupling to the head shell. Grounding for all the co-ax cable shields is connected at the single point copper block and subsequently isolated until the shields terminate at the head shell. Furthermore, every unused electrical line in the microscope is grounded to add shielding wherever possible. Care must also be taken to ensure that unused piezo connections are grounded and that all piezo voltages are properly referenced to a common ground to ensure no drift in piezo position for either the scanner or stepper piezos.

Further optimization of the electrical system would include pairing every single signal line with a twisted ground line, shortening every signal line as much as possible, and incorporating a low temperature current pre-amp into the body of the micro-

scope(as close as possible to the head shell). Tests have shown that high voltage discharges such as the firing of the excimer laser(30 kV) in close proximity can introduce noise spikes in the STM current signal. Further improvements to the STM shielding system would have the entire microscope enclosed in an RF shielded room.

5.4 Vacuum Systems

The head shell of the STM is enclosed in a vacuum can with optical access. Many STM experiments were performed with the STM headshell immersed directly into liquid helium but continuous tunneling was hampered by paramagnetic solid oxygen present in our liquid helium supply and condensed from the atmosphere. Because the superconducting vortex state of $NbSe_2$ is being studied it is necessary to mount our samples on small permanent magnets. These magnets slowly attract solid oxygen which ends up coating the sample under study. This result motivated the development of an STM with a vacuum can to isolate the tip and sample from the liquid helium environment.

This can is mounted to the base of the body of the microscope using a compressed lead wire. A 2" diameter stainless steel pipe runs the length of the microscope and allows the vacuum can to be evacuated through a turbo-pump at the top of the microscope, resting on the 4 steel plates. Backing the turbo pump is a dry scroll pump. This pump was chosen to avoid the possibility that pump oil could be cryo-pumped back into the microscope if the turbo pump ceased to function. Also available in this pump system is a fixed volume at the top of the microscope. This fixed volume(about 1 liter) can be connected to the STM vacuum can, to inject helium as a thermal exchange gas, when the microscope is inserted into a bath of liquid helium during low temperature use. This system constitutes the "clean vacuum" side of the microscope. The turbo-pump system is only used on this side of the vacuum system, to evacuate to around 10^{-8} torr. This clean vacuum system can be baked

out from top to bottom, although care must be taken with the vacuum can so as not to damage the seals of the sapphire windows which give optical access for the STM tip and sample.

All the wiring from the top of the microscope down to the top of the vacuum can runs in the "dirty vacuum" side of the microscope. This side of the vacuum system cannot be baked out. It contains the three shielded stainless steel tubes which contain all the STM wiring. It also contains a small stainless steel tube for fiber optics as may be needed in certain experiments. The dirty vacuum system is pumped out using our Veeco MS-17 leak detector to pressures around 10^{-5} torr. By separating the microscope into clean and dirty vacuum systems, we greatly expand the available surface area we can bake out. It is always a wise idea to pump out the dirty vacuum side of the microscope to reduce the pressure gradient across seals between dirty and clean vacuum cavities. It is also necessary to prevent significant amounts of condensation accumulating in the dirty vacuum side of the microscope when it is at low temperatures. This condensation can potentially plug vacuum lines, with disastrous consequences. With this configuration we expect to achieve low temperature partial pressures of less than 10^{-10} torr for all species other than helium, with a helium vapor pressure of a few hundred milli-torr acting as the thermal exchange gas.

5.5 STM investigations on NbSe$_2$

Time-resolved imaging of NbSe$_2$'s superconducting energy gap has been the motivation for the design of the microscope which has now been outlined. Though this has not yet been accomplished many topographic and spectroscopic scans have been performed on NbSe$_2$ at room temperature and at low temperature. Some of these results will now be presented to show the limited successes of the microscopes developed to study this material.

122

$NbSe_2$ can be grown in crystal form through the process of chemical vapor transport [7, 8]. In this procedure one measures out the correct ratio of reagents(185.2 mg of Nb and 314.8 mg of Se to make 500 mg of $NbSe_2$), and places these reagents into a glass tube capped at one end(tube was 22 cm long and had a 1 cm ID). In addition to the niobium and selenium a small amount of iodine($\approx$ 86 mg) was added as a vapor transport agent to help promote crystal growth [9]. The glass tube is then sealed under vacuum and placed in an oven with all reagents at one end of the tube. The oven has a non-uniform heating profile so that a thermal gradient can be formed. The high temperature end of the oven was heated to 800°C while the low temperature end was heated to 725°C. The glass tube was placed in the oven such that the reagents were at the 800°C end of the oven. The oven was cycled as follows with the sample inside it:

- 2 day warm up from room temperature to T_{high} = 800°C and T_{low} = 725°C.

- 5 day bake at T_{high} = 800°C and T_{low} = 725°C.

- 1 day cool down, back to room temperature.

Many different structural phases(polymorphs) exist for $NbSe_2$ [10] so to confirm that we had grown the correct crystal phase(2H phase), a powder x-ray diffraction pattern was taken, and compared with the theoretical structure calculated from the referenced structure. The theoretical and measured powder diffraction patterns are shown in panels (a) and (b) of Figure 5.6. The excellent agreement between the predicted x-ray diffraction pattern and the observation lead us to conclude that we had produced the correct structural phase of the material.

STM topographic scans of the surface of $NbSe_2$ have revealed two distinct surface types. The first surface type, seen in small area high resolution scans, is characterized by small grains of material, 5→10 nm in size as seen in Figure 5.7 and Figure 5.8. This sort of crystal growth was also visible in TEM micrographs over similar length

123
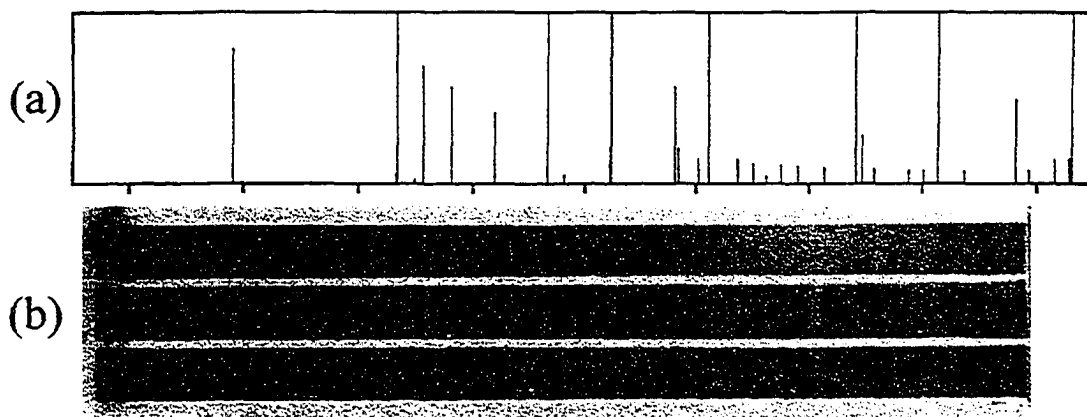
Figure 5.6: (a) NbSe$_2$ Calculated Phase. The length of the vertical lines indicates the intensity of the measured spectral lines. Lines extending all the way to the top of the figure are calibration lines for a powdered Si calibration sample. (b)NbSe$_2$ Measured Phase. The top trace is the Si calibration sample, while the lower two traces are for the NbSe$_2$ samples.

scales. TEM electron diffraction revealed that these grains are monocrystalline. The surface structure observed in these figures was seen in a minority of the NbSe$_2$ samples studied.

The majority of surface topographies bore a stronger resemblance to that shown in Figure 5.9. In NbSe$_2$, intralayer forces between atoms are at least 100× greater than interlayer forces. This results in a material which can be easily peeled, exposing clean inert surfaces ideal for STM study. These last figures show the freshly peeled plane structure expected for NbSe$_2$.

In addition to topography on NbSe$_2$ we are also interested in performing I/V and I/Z spectroscopy. I/V spectroscopy both above and below the transition temperature should show marked differences due to superconductivity. Below T$_C$=7.2 K for NbSe$_2$ a δ = 1.1 meV energy gap begins to open which can be imaged using I/V spectroscopy. In addition to the 1.1 meV gap, a ±34 mV charge density wave discontinuity is present below ≈ 33K. Figure 5.10 shows 3 preliminary spectroscopic scans of the same NbSe$_2$ surface. If one were tunneling with a metallic tip into a metallic sample, the $\frac{\partial I}{\partial V}$ scans would appear as straight horizontal lines in this figure. The sharp dip in conductivity

124
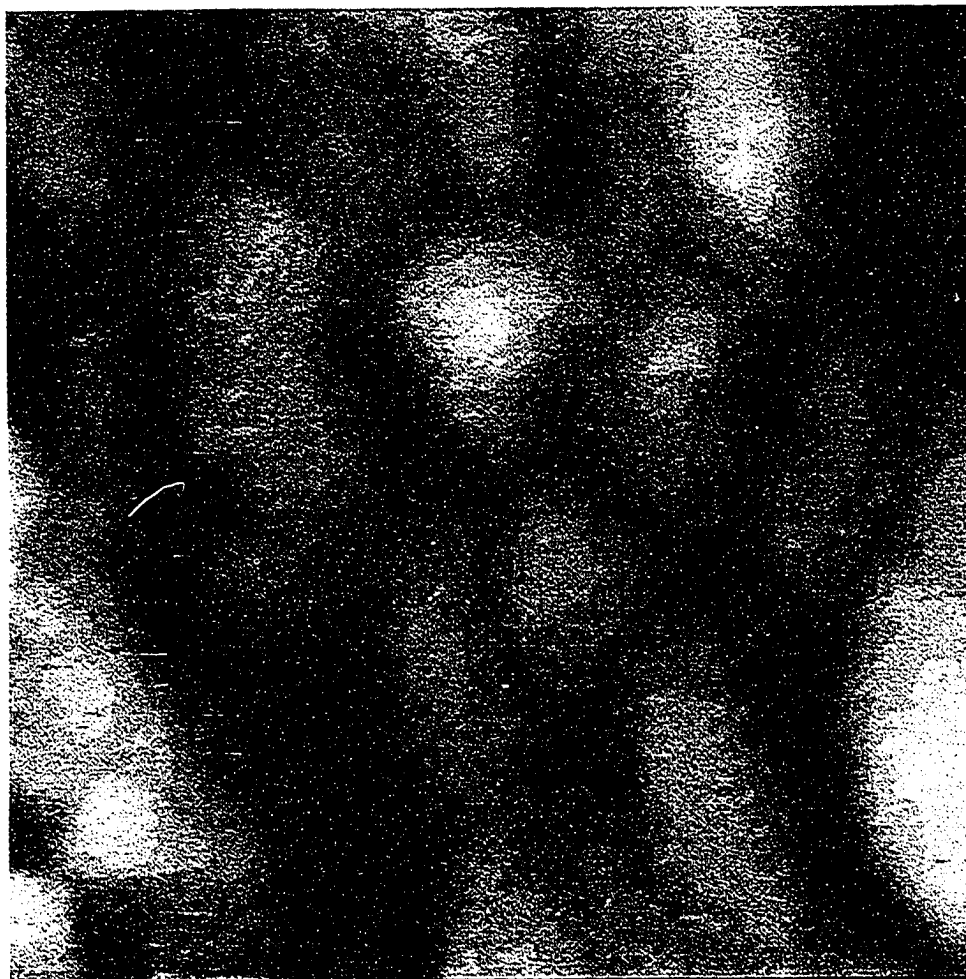
Figure 5.7: 40 nm by 40 nm, z range 1.1 nm scan of an NbSe$_2$ surface at room temperature. Tunneling was performed at 30 mV bias voltage, 0.5 nA tunneling current.

125

Figure 5.8: 80 nm by 80 nm, z range 2.9 nm scan of an $NbSe_2$ surface at room temperature. Tunneling was performed at 30 mV bias voltage, 0.5 nA tunneling current.

126
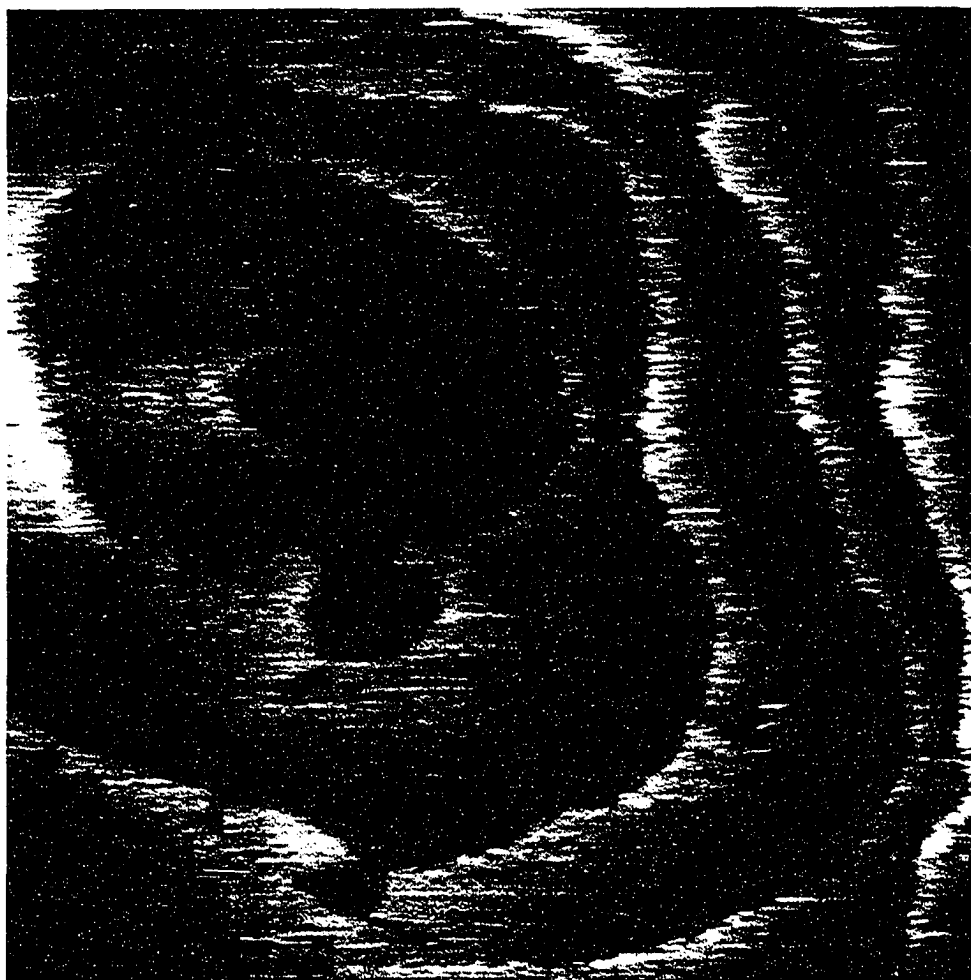
1.00 V at 100 pA
165 nm by 165 nm, z range 5.35 nm

Figure 5.9: Terraced surface of $NbSe_2$ showing 4 Åsteps. Step edges appear bright due to overshoot in the feedback system.

127

at 0 V bias is due to the formation of Cooper pairs at the Fermi energy, suppressing the density of states. The overall parabolic shape of each curve is due to the charge density wave state. Close examination of the width of the gap in Figure 5.10 reveals that the width is 4.4 meV. The width of the gap in Figure 5.10 should be $2\Delta = 2.2$ meV but the observed width is twice that value. This can be explained if one suspects that the STM tip has become contaminated with $NbSe_2$, which is quite possible in this instance as the STM tip did crash before this I/V scan was taken. Further I/V scans will be required to understand whether the ripple oscillations in Figure 5.10 are real or an artifact. I/V measurements taken as the sample temperature rose above T_C lacked the superconducting gap structure shown here.

Whenever spatial and spectroscopic images are acquired using STM it is necessary to assess the conditions of tunneling by performing I/Z spectroscopy and measuring the effective work function of the tunnel barrier. Figure 5.11 shows a typical I/Z spectra acquired while tunneling into $NbSe_2$ at liquid helium temperatures. Fitting the current in Figure 5.11 with an exponentially decaying function allows us to calculate the effective work function ϕ from the decay constant. If the exponential fit is of the form $I = I_0 e^{-2\kappa z}$ where I_0 is the initial current, z is the tip height and κ is the decay constant. Then the work function ϕ can be related to κ by:

$$\kappa = 0.51\sqrt{\phi(eV)}\text{Å}^{-1} \qquad (5.2)$$

Using this equation gives a value for $\phi = 2.5$ eV tunneling into $NbSe_2$, comparable to the 2 eV work function measured by Hess [1].

The preliminary results presented here are part of an ongoing effort to first reproduce some of the static vortex imaging results of Hess et al. [1] as an initial step in investigations into time-resolved vortex dynamics. An experimental proposal to do will now be briefly outlined. STM tunneling between a metallic tip and a supercon-

128
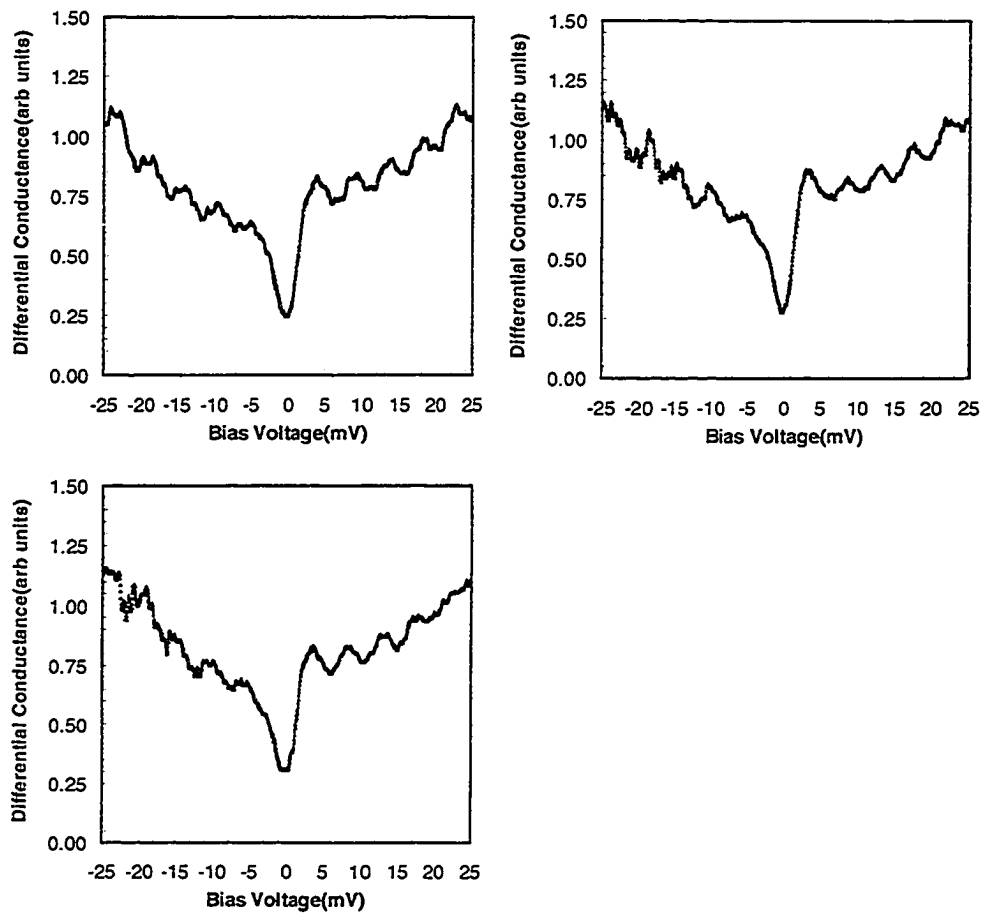
Figure 5.10: 3 separate spectroscopic scans of the differential conductance of NbSe$_2$ over the range of ± 25 meV.

I/Z tunneling into Niobium Diselenide at 4.2 K
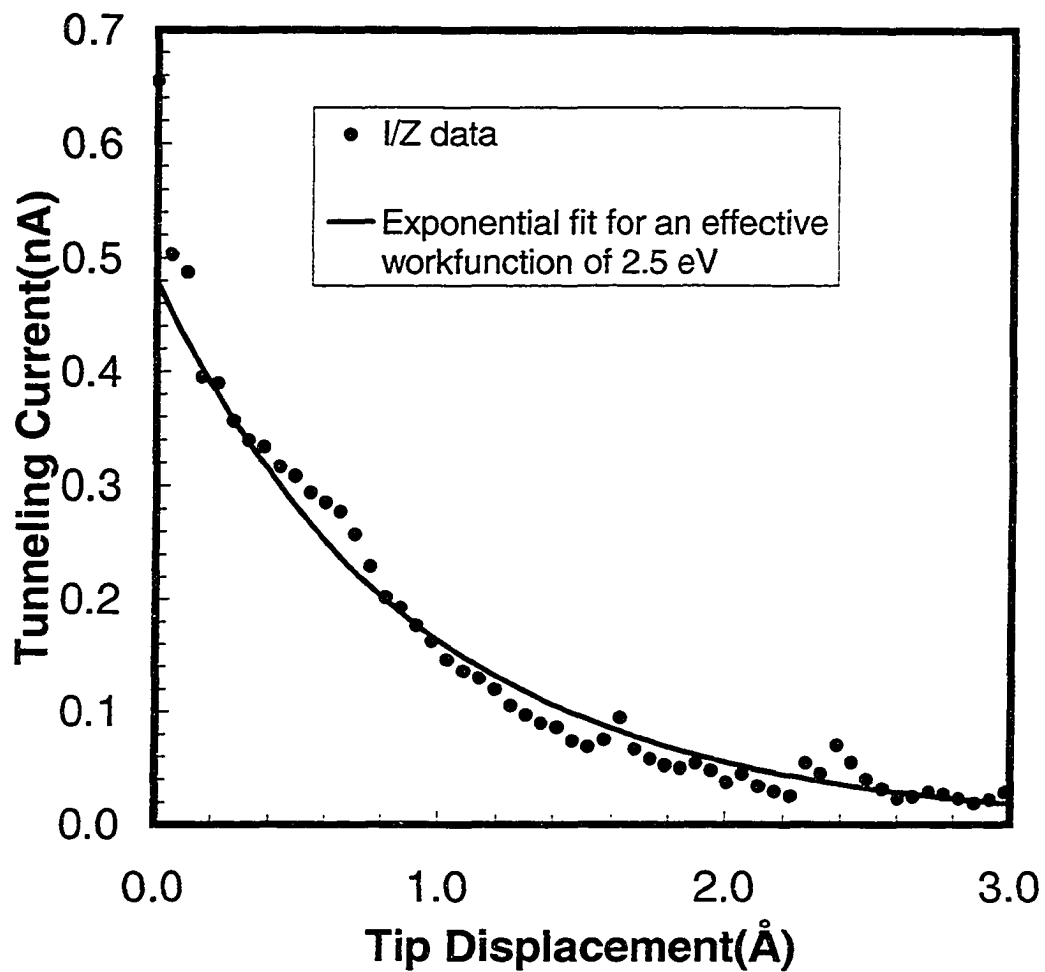
Figure 5.11: I/Z tunneling into niobium diselenide at 4.2 K

130

ducting NbSe$_2$ sample will be established. The NbSe$_2$ sample will be mounted on the STM sample sled, shown in Figure 5.2. Beneath the sample a 1.2 Tesla neodymiumn iron boron magnet will create the vortex state in the NbSe$_2$ sample once it is cooled below T$_C$=7.2 K. The spacing between vortex cores is expected to be 489 Å/B$^{1/2}$ or 53.6 nm [11]. Imaging the vortex state will be one of the primary steps in the experiment. Another primary step is to determine whether Ti/Sapph illumination of the NbSe$_2$ surface affects its superconductivity as observed by Testardi [12] in thin Pb films. Testardi observed local heating of electrons above the lattice temperature which suppressed superconductivity in Pb. Optically heating electrons above T$_C$ in our NbSe$_2$ samples will be the pump in the pump/probe experiment. It may be possible to observe an effect in the DC I/V spectra, but by junction mixing STM it should be possible to directly image the I/V spectra as a laser pulse is incident on the tunnel junction and time-resolve the evolution of the LDOS from a superconducting state to a normal (hot electron) state and back to a superconducting state as the electron heat is transferred to the NbSe$_2$ lattice. By combining lattice imaging, with the time-resolved evolution of the LDOS, due to optical pumping the NbSe$_2$ surface, we will attempt to image the evolution of the vortex state due to optical pumping. The surface vortex state should vanish as hot electrons are produced on the surface due to optical pumping but the bulk vortex state should remain allowing vortices to reform in their same positions on the superconducting surface once the electrons have cooled and the surface state is restored.

To this point our attempts to image the vortex structure of NbSe$_2$ have met with limited success. Initially vibration isolation and electrical requirements have necessitated multiple redesigns of the microscope in an attempt to achieve stable low temperature STM tunneling into our samples. The latest efforts with an STM immersed in liquid helium were hampered by the nucleation of helium bubbles on the surfaces of the STM along with the unfortunate gettering of solid oxygen onto our sample surface

131

49.8 mV at 1.90 nA
50.9 nm by 50.9 nm, z range 8.85 nm

Figure 5.12: $NbSe_2$ surface with hole in the corner of the image. Small depressions in the flat plane topography are 4Ådeep.

and magnetic damping mechanisms. These problems have lead to the recent development of a high vacuum low temperature microscope which should eliminate the present experimental barriers. Other concerns for low temperature tunneling include the risk of condensation forming on the samples of interest as they are cooled.

To surmount this obstacle, experiments have begun to laser ablate our sample surfaces in situ at low temperatures. Results of such a laser ablation can be seen by comparing the surface shown in Figure 5.12 that of Figure 5.13. The stark

132

49.8 mV at 1.83 nA
50.9 nm by 50.9 nm, z range 40.1 nm

Figure 5.13: The same NbSe$_2$ sample shown in Figure 5.12 after focused illumination with a 20 mJ Excimer 308 nm laser pulse.

133

contrast between the surfaces before and after the laser pulse suggests a large amount of original surface has been removed, exposing a clean contaminant-free surface. This has not yet been confirmed as the present experiments were performed in ambient conditions and no change in the surface work function was observed.

Another factor which has hindered recent progress has been in the slow turn around times of the microscope when STM tips perform poorly. Currently STM tips are purchased commercially to ensure consistency. Once a tip is mounted into the microscope, the microscope is evacuated and cooled, a time consuming process, and then tunneling is attempted. If the tip is not in excellent condition it must be replaced. The warm up time for the microscope is quite long and many hours must pass before another tunneling attempt can be made. Recently however a new room temperature STM was purchased with the goal of allowing us to characterize our STM tips before they are mounted in the low temperature microscope. With this pre-characterization we hope to reduce the number of unsuccessful microscope cool downs increasing our tunneling efficiency.

A great deal of effort has gone into the design and construction of a high vacuum low temperature scanning tunneling microscope. The vibration isolation system consists of 4 stages, a stable sand based mount, supporting a pneumatic isolation system which itself supports a series of stacked steel plates. Hanging from this on stainless steel springs rests the microscope itself. This isolation system is sufficient in isolating our microscope from the mechanical vibrations of the building and the bubbling action of the cryostat. The electronics of the microscope have been carefully designed to eliminate and shield all sources of noise and cross talk which might interfere with the delicate current measurements which STM requires. The performance of the microscope has been continually improved over a number of years to the point that atomic scale resolution has been achieved and sub meV spectroscopic resolution has

also been demonstrated. It is unclear how close the current system is to being able to make the vortex imaging measurements we would like. All indications suggest that this should be achievable with the latest microscope which has been developed. Past experiences warrant cautious optimism that such measurements can be made in the not too distant future.

References

[1] H. F. Hess, R. B. Robinson, R. C. Dynes, J. M. Valles, Jr., and J. V. Waszczak. *Phys. Rev. Lett.*, 62:214, 1989.

[2] A. Dhirani, A. J. Fisher, and P. Guyot-Sionnest. *Rev. Sci. Instrum.*, 67:2953, 1996.

[3] K. Nagaya. *Transactions of the ASME: J. Dynam. Syst. Meas. Control.*, 106:52, 1984.

[4] C. Julian Chen. *Introduction to Scanning Tunneling Microscopy*. Oxford University Press, New York, 1993.

[5] Henry W. Ott. *Noise Reduction Techniques in Electronic Systems*. John Wiley & Sons, New York, 1976.

[6] Ralph Morrison. *Grounding and Shielding Techniques in Instrumentation*. John Wiley & Sons, New York, 1967.

[7] R. Kershaw, M. Vlasse, and A. Wold. *Inorg. Chem.*, 6(8):1599, 1967.

[8] R. M. A. Lieth, editor. *Preparation and Crystal Growth of Materials with Layered Structures*, volume 1 of *Physics and Chemistry of Materials with Layered Structures*. D. Reidel Publishing Company, Boston-U.S.A., 1977.

[9] Antony R. West. *Solid State Chemistry and its Applications*. Wiley, New York, 1984.

[10] F. Kadijk and F. Jellinek. *J. Less-Common Metals*, 23:437, 1971.

[11] H. F. Hess, R. B. Robinson, R. C. Dynes, J. M. Valles, Jr., and J. V. Waszczak. *J. Vac. Sci. Technol. A*, 8(1):450, 1990.

[12] L. R. Testardi. *Physical Review B*, 4(7):2189, 1971.

Chapter 6

Conclusions

Driven by the desire to study ultrafast phenomena on nanometer length scales several proposals were made to develop time-resolved scanning tunneling microscopy. The three most significant of these were the photo-gated STM approach of Weiss et al. [1] and Takeuchi and Kasahara [2], the distance modulation technique of Freeman and Nunes [3] and the junction mixing technique developed by the same authors [4].

PG-STM boasted excellent time and spatial resolution, but the basis for these claims was not sound. Citing vertical sensitivity as a measure of spatial resolution is misleading and it was later discovered that the time-resolved signal from the PG-STM was capacitively coupled from sample to tip [5]. This led to the conclusion that the true spatial resolution of PG-STM would be hundreds of nanometers at best.

Distance modulated STM does not have such limitations. Rapid changes in tip/sample separation are used to demodulate the fast response of a sample under investigation. This technique is quite general in its applications. So long as one can excite a sample repetitively such that the excitation can be detected by the STM the distance modulation technique should work. Transmission lines launching electrical pulses at the tunnel junction are not required. What is required is that the tip of the STM can be physically moved on very fast time scales. This technique has been demonstrated up to nanosecond time scales, but if faster time-resolution is required the distance

137

modulation technique will not suffice.

Junction mixing STM is suited for situations where ultrafast time resolution is required. This method for time-resolved STM employs no moving parts, instead relying on the non-linear electrical properties of the STM tunnel junction to demodulate ultra-fast sample response. For this technique to work an electrical probe pulse must be launched into the tunnel junction of the STM. The pulse may be launched from the STM tip or from a sample giving JM-STM flexibility to study samples non-invasively.

Working to develop JM-STM, three key experiments were presented in this thesis. The first work used a lithographically patterned transmission line structure to launch two electrical pulses into the tunnel junction. These pulses were successfully detected by the STM as it tunneled into the transmission line. The detection of a 10 ps time-resolved signal marked an order of magnitude improvement over previous JM-STM experiments [4]. By launching electrical pulses from either side of the STM tip this experiment was the first to confirm that non-linearities in the tunnel junction were the only source for this signal.

A direct demonstration of combined spatio-temporal resolution was the last hurdle in establishing JM-STM. By patterning an array of small titanium dots onto a transmission line structure combined spatio-temporal resolution could be demonstrated. Titanium provides I/V contrast with the gold of the transmission line, so the time-resolved signal will vary as the STM scans across the titanium gold interface(the edge of a titanium dot). Varying pump/probe delay times allowed an electrical probe pulse to sample the pumped transmission line sample. At every pump/probe interval an STM spatial and time-resolved scan was taken, creating the first ultrafast STM movie.

To confirm the interpretation of previous results and explore the limitation of the JM-STM technique a lumped element model was developed. Fits from this model to experiment contained only one fitting parameter, the size of the voltage pulses on the transmission line. Using this fitting parameter we find excellent agreement between the model and experimental data [1]. Extrapolating results from the model allows the prediction that JM-STM can be extended into the femtosecond time regime, limited by the geometrical tip/sample capacitance.

To demonstrate JM-STM on a physically interesting system a low temperature high vacuum STM was developed. This microscope provides the optical access and electrical connections required for JM-STM. Mechanical vibration isolation was met by hanging the microscope into a liquid helium dewar without allowing dewar vibrations to couple to the microscope. A high vacuum environment was provided using a turbo-pump backed by a dry scroll pump. Using this microscope I/V spectroscopy on $NbSe_2$ has revealed superconducting gap structure.

By combining our newly developed high vacuum low temperature STM with our reliable Ti/Sapph laser system, investigations into nonequilibrium superconductivity on $NbSe_2$ are poised to commence.

References

[1] S. Weiss, D. F. Ogletree, D. Botkin, M. Salmeron, and D. S. Chemla. *Appl. Phys. Lett.*, 63:2567, 1993.

[2] K. Takeuchi and Y. Kasahara. *Appl. Phys. Lett.*, 63:3548, 1993.

[3] M. R. Freeman and Geoff Nunes, Jr. *Appl. Phys. Lett.*, 63:2633, 1993.

[4] Geoff Nunes, Jr. and M. R. Freeman. *Science*, 262:1029, 1993.

---

[1]it should be noted that voltage pulse magnitudes agreed well with our estimates

[5] R.H.M. Groeneveld and H. van Kempen. *Appl. Phys. Lett.*, 69:2294, 1996.

Appendix A

Junction Mixing STM Control Software

A.1 Introduction

In order to control the microscopes used in this research it was necessary to write a great deal of controlling software. Software was required which would monitor and control the STM sample approach, scanning functions, spectroscopy functions and analysis. LabView was chosen as the development environment due to its ease of use and its rapid application development time.

LabView is an object oriented graphical programming environment which consists of modules, control structures and wiring to connect modules together. Modules are basically subroutines with a discrete number of input and output ports. Module input/output types are numerous, consisting of numerical, boolean and string constants or arrays. One of the strengths of LabView lies in the vast library of available modules and the simplicity with which they can be connected together. Connections between modules is accomplished through LabView's wiring tool. Wiring is typically made between the output of one module to the input of another. This is only possible if the output and input share a common data type (you could not wire a boolean array to a string input, only to another boolean array). To control the order and frequency with which modules are executed, LabView includes a basic set of control structures. In order to repeat an operation n times one could simply encircle the appropriate modules with a for loop. To do this you literally just drag a for loop over the modules and wire the number n to the input of the loop. LabView's control structures include for loops, sequence structures, while loops and case structures.

141

As one might expect for a development environment LabView includes extensive debugging features and profiling tools. Setting break points, pause points and a 'visual execution' mode showing program execution in slow motion along with the values passed from module to module are all features which simplify debugging. Profiling tools allow the user to time how long it takes for any given module or section of modules to execute. This execution time typically results from a combination of processing time, operating system time (where the operating system interrupts the operation of LabView to perform other tasks) and I/O time where LabView is sending or receiving data from a data acquisition card for example.

Data acquisition and experimental control functions are the best applications for LabView programs. LabView contains pre-built modules specifically designed for interfacing with data acquisition cards. This eliminates the need for the end user to learn the technical details of the specific data acquisition device. Using pre-built data acquisition modules a user could be sending and receiving data from computer to data acquisition card (DAQ) in mere minutes. Since these DAQ modules can be easily linked to other LabView modules such as a 2D-graphing module one could capture and plot 2D data in a very simple LabView program containing just 2 modules wired together. By adding one more module to output data to a digital to analog(DAC) converter one could create a simple scanning program which outputs voltages to control an actuator's position while simultaneously reading transducer values and plotting the values on a computer screen. All this with just 3 modules and about 2 minutes of programming!

Due to its ease of use LabView was chosen as the programming environment for developing the control and data acquisition tools for our STMs. There are 4 basic functions associated with a TR-STM system for which control programs were developed:

- STM sample approach

- STM topographic scanning

- STM I/V and I/Z spectroscopy scanning

- Optical delay line scanning

Details of each of these programs will now be addressed.

142

A.2   STM sample approach

In a typical STM system there are two approach mechanisms to bring the tip of the microscope into tunneling distance with the surface to be investigated. A coarse approach mechanism will bring the tip of the microscope close enough to the sample that the fine approach mechanism can establish tunneling. Coarse approach mechanisms used in this work include a stepper motor based approach and a linear stick slip approach. In the stepper motor approach a stepper motor is connected to a screw which drives the STM tip into the sample. The motion of the screw is de-amplified so that discrete motor steps are on the order of 8 nm. The coarse linear stick slip approach uses a 3 piezo tube base, which the sample rests on. By applying a slowly increasing voltage to the base piezo's the sample can be moved towards the tip. By rapidly reducing the applied voltage back to zero the piezo's will snap back to their initial position, but the sample will remain fixed. This is accomplished since the kinetic friction between the sample and base as the piezo's are snapped back, is less than the static friction between sample and piezo's as the sample is moved slowly forward. In both microscopes used in this work, the same fine approach mechanism is used. A five electrode piezo is used for fine tip/sample approach. The outer four electrodes control tip x/y deflection while the central z electrode controls the tip height above the sample.

The complete approach is accomplished as follows. A negative voltage is applied to the z electrode of the piezo tube to retract the tip. The coarse approach the moves the sample and tip one step closer together. If the tip has not encountered the surface the piezo tube is slowly extended up to its full length in an attempt to establish tunneling. This sequence is iterated until tip and sample are close enough that a measurable current is found.

Two main programs are used to control the STM tip approach. The first program found in the Gms.llb library is called 'Tip Approach' and is used to control the stepper motor approach of the room temperature STM. The front panel(user interface screen) of 'Tip Approach' is shown in Figure A.1. The functions of the controls on the front panel will now be outlined. For the program to run the 'On' switch must be in the up position. Once the program is running the stepper motor will advance in either the up or down direction by either a half or full step increment. For clarity up and down refer to the direction the screw attached to the stepper motor will move. If the 'Windings are On' button is not engaged the stepper motor will not move and

143
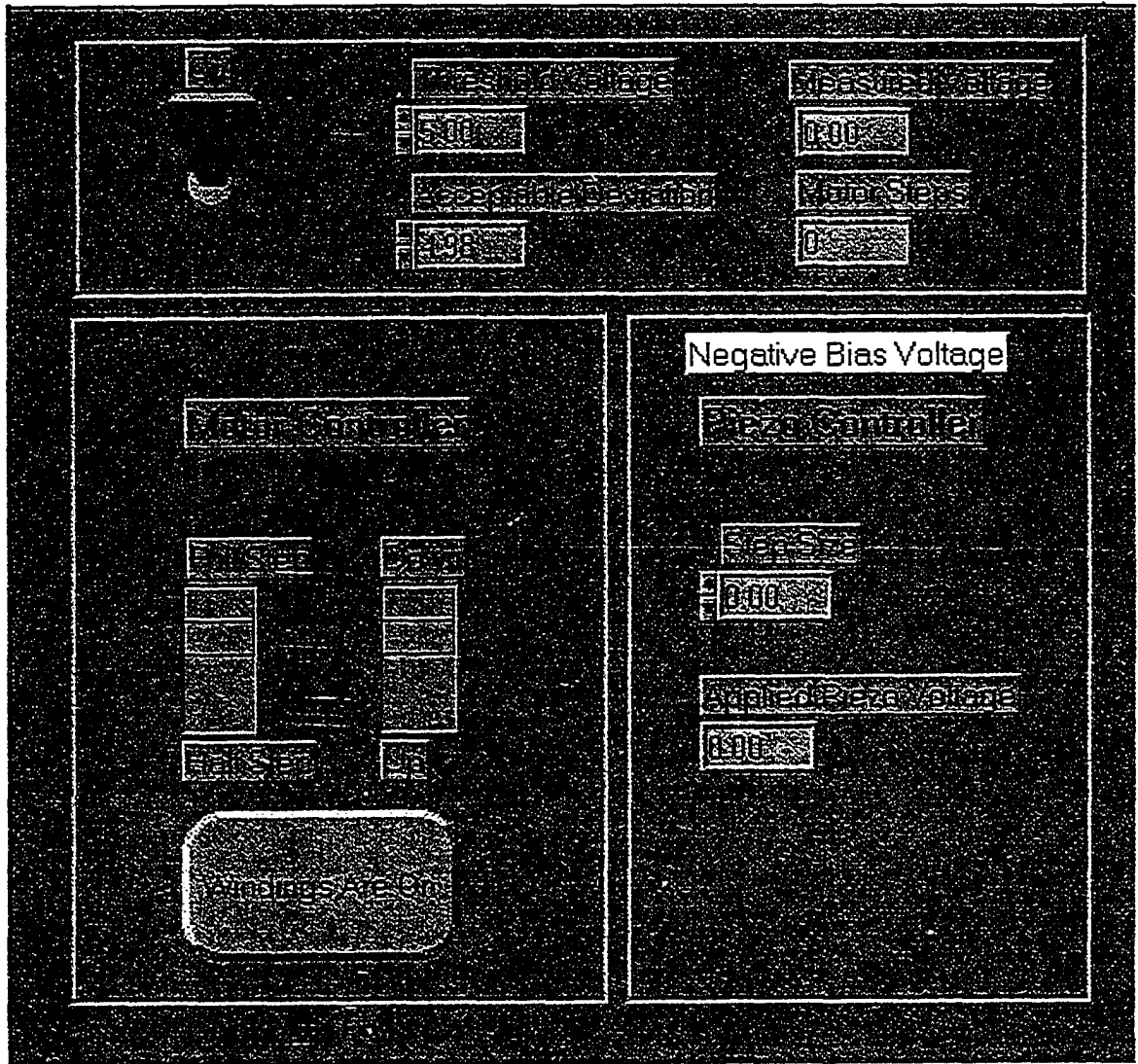
Figure A.1: User interface for the program 'Tip Approach' used to control the room temperature STM stepper motor approach.

144

the screw can be adjusted by hand. The piezo 'Step Size' is the increment in volts between 5 mV and 20 V that is used to move the piezo towards the surface after a coarse motor step is made. Initially the piezo will be fully retracted(at -10 V) and the motor will advance one step. Then the piezo will be incremented from -10 V to 10 V in 'Step Size' voltage increments. The motor coarse approach and piezo fine approach will continue until a voltage is read which is within the 'Acceptable Deviation' of the 'Threshold Voltage'. In typical STM scans a current of .5 nA was used, with a bias voltage of 50 mV a current pre-amp gain of 10^8 V/A. The homebuilt IBM feedback controller feedback set point is set to 4.24. When proper tunneling is established the current voltage converter would give a voltage of 50 mV and the 'Threshold Voltage' used for the approach is 5 V with an 'Acceptable Deviation' of 4.98 V. Under these circumstances any voltage above 20 mV will trigger the approach to stop. It should also be noted that the program takes the absolute value of the measured voltage so that the approach works with either positive or negative bias voltage polarity. If the tip does crash into the surface and the user wants to withdraw it quickly on can simply reverse the motor step direction, set the 'Threshold Voltage' to zero and the 'Acceptable Deviation' to 20 mV to pull the tip out of a crashed condition. Another idiosyncrasy to note is that if the piezo 'Step Size' is set to zero the piezo will not be stepped during the approach. This will speed up the tip approach immensely and is not a problem so long as the range of the STM feedback system is larger than the motor step size(STM feedback range can be increased by simply amplifying the output of the feedback controller using the high voltage power supply).

The approach program described above operates for the room temperature STM using a stepper motor as the coarse approach mechanism. The next program discussed is designed for the low temperature STM and controls a stick slip coarse approach. The front panel of 'Fast approach 1.1', found in the STM2_lib.llb library is shown in Figure A.2. The basic function of this program is to output a sawtooth waveform to drive the base piezo's such that the sample(resting on the base piezo's) will be ratcheted towards the sample. The 'Direction' switch controls the polarity of the voltage pulse. The pulse is output to both channels 0 and 1 of the DAQ and the polarity of output 0 is opposite that of channel 1. These voltages are applied to the front and back surfaces of the piezo's respectively. The amplitude of the sawtooth waveform is controlled by the 'Pulse Voltage' control and the 'Approach Mode' control sets the number of discrete steps in the rising edge of the waveform. The update rate sets the number of DAQ updates per second and should be set to 20 kHz. The 'Iterations' indicator keeps track of the total number of steps made in the approach.

145
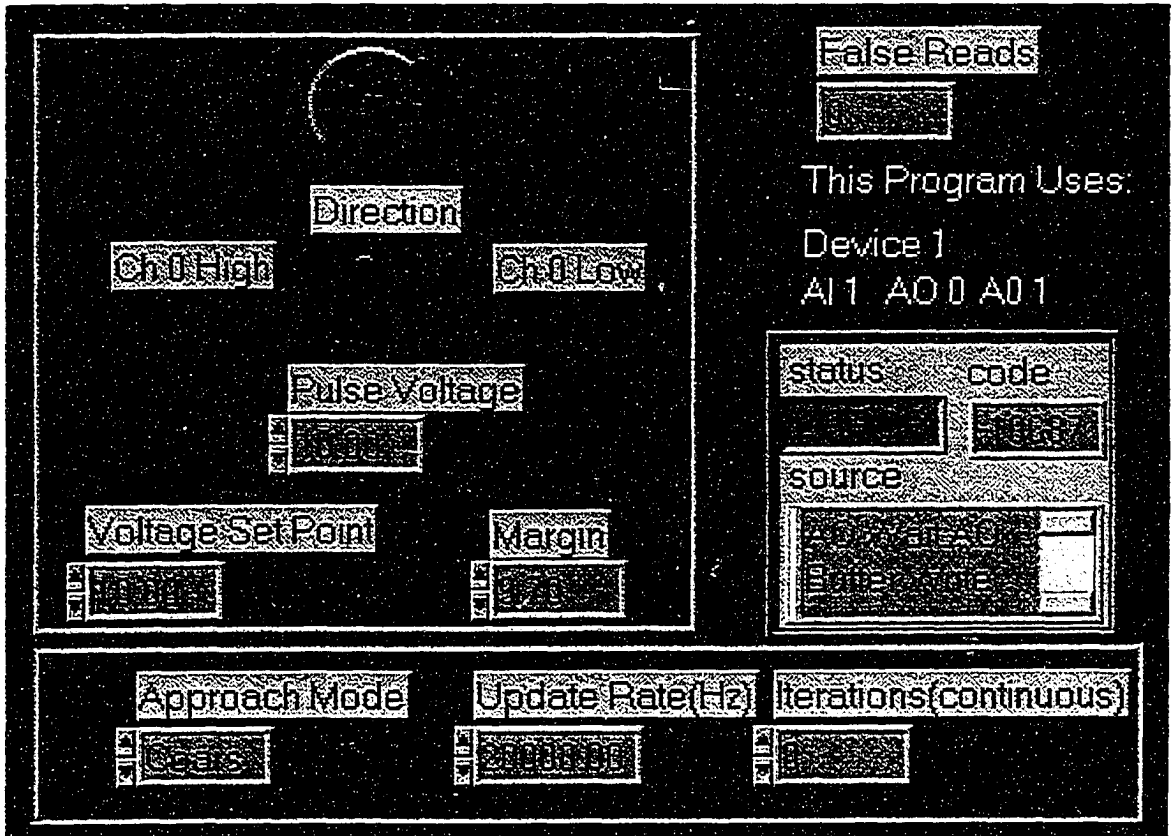
Figure A.2: User interface for the program 'Fast approach 1.1' used to control the low temperature STM stick slip approach.

146

The 'Voltage Set Point' and 'Margin' behave in the same way that they did in the 'Tip Approach' program. When the sample is approaching in this way capacitive coupling in the STM wiring can often led to pickup on the STM tip line. This pickup is amplified in the current to voltage converter and can trigger the approach mechanism to halt an approach. To compensate for this once the approach mechanism is stopped the tip voltage is again checked with respect to the 'Voltage Set Point'. If the voltage is not within the 'Margin' to the 'Voltage Set Point' then the approach is resumed and a 'False Read' is indicated in the indicator box. Once the tip approach has completed and the STM is tunneling it might be necessary to do single step coarse adjustments to the sample position. These can be accomplished by using the 'Manual Approach 1.1' program found in the STM2_lib.llb library. The front panel for this program is shown in Figure A.3. With this program the user can step the STM sample a single step towards or away from the tip using the inner left and right buttons in the 'Manual Approach Control Cluster'(pressing one of these buttons will send one sawtooth wave and move the sample by one increment. The outer left and right buttons can be held down to step the sample continuously in the desired direction. The scanner voltage control can be used to adjust the tip position. The 'Pulse Characteristics' cluster allows the user to adjust the shape and speed of the waveform(these settings should not have to be adjusted).

A.3   STM topographic scanning

Once the STM sample has been moved to within tunneling distance of the sample the user may want to perform topographic scans of the samples surface. In order to accomplish this the STM feedback, bias and high voltage electronics are configured so that the a fixed bias voltage is applied to the sample, the feedback electronics output a voltage to the high voltage supply which is amplified and sent to the STM piezo's such that a constant current from the current pre-amp is maintained. This configuration is known as constant current tunneling. If the tip of the microscope is moved over the surface of the sample the feedback electronics adjusts the height of the tip so that it remains a fixed height over the sample. By monitoring the feedback voltage one can track the topography of the surface. A simple topographic scanning program will simply raster scan the STM tip through a grid of positions over the surface. At each grid point the scanning program will input the feedback voltage signal in order to build a topographic image of the surface. Two STM scanning programs have been devolved for use with the room temperature and low temperature STMs. The properties of the two programs and their operation will now be discussed.

147
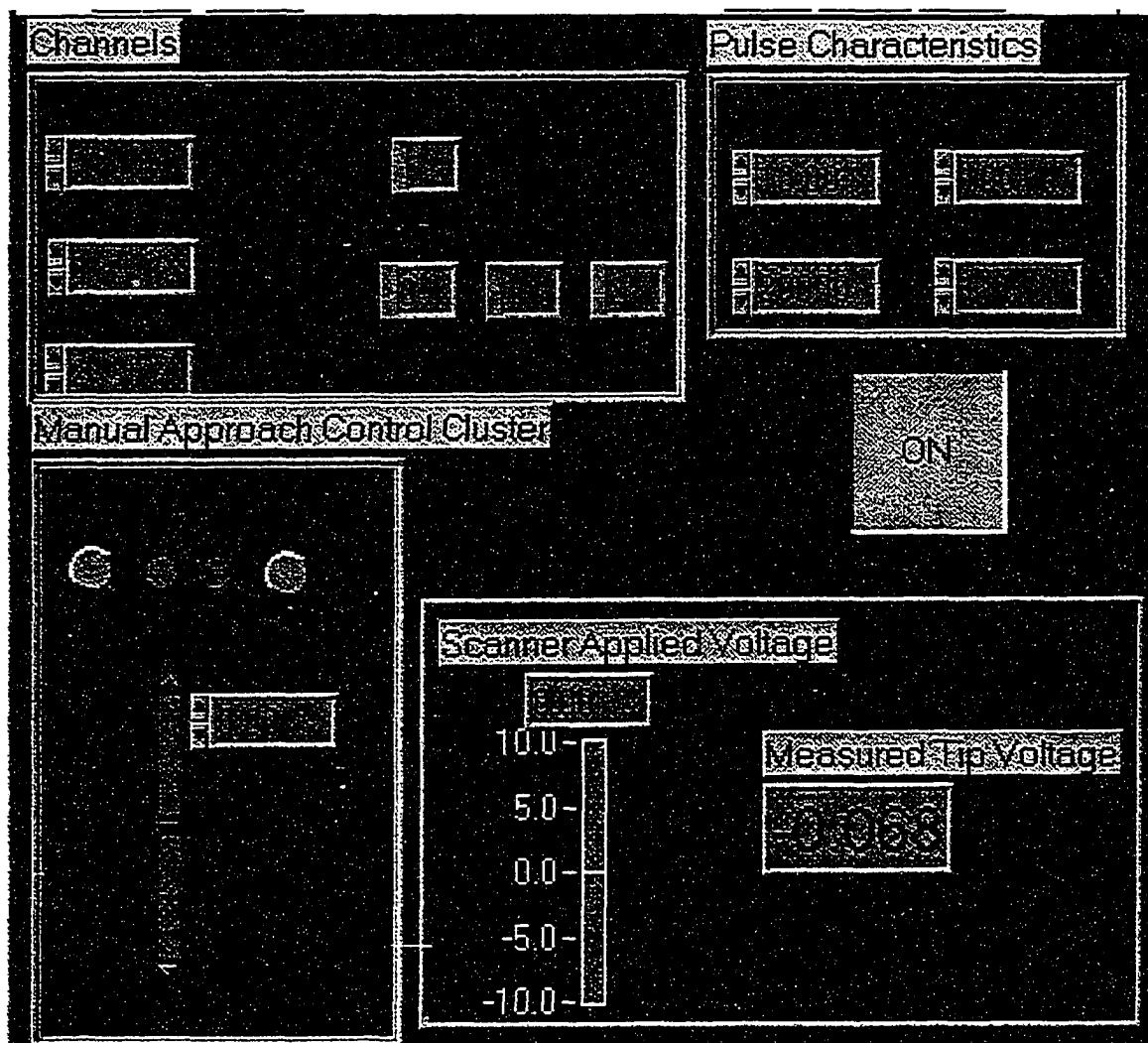
Figure A.3: User interface for the program 'Manual approach 1.1' used to step the low temperature STM stick slip approach.

148

The first scanning program to be discussed is called 'STM Scan w/N-Regression v3.4' found in the STM2_lib.llb library. The front panel of this program is shown in Figure A.4. The first controls to look at when setting up a scan are the primary and secondary scan amplitudes. These can be set between 0 V and 10 V and will set the amplitude of a bipolar scan. So a primary scan amplitude of 0.42 V will scan the tip in the primary direction over a voltage range of -0.42 V → 0.42 V. So long as the primary and secondary scan amplitudes are the same the topographic scan will be square but the user can set the secondary scan amplitude to whatever value is desired; zero for example will cause the controller to perform a line scan over the surface. Primary and secondary scan points control the grid spacing of points over the primary and secondary voltage ranges. Forward and backward delay times set how long the tip waits at each grid point before acquiring data in the forward and back, scan direction[1]. The X Offset and Y Offset controls are currently disabled. Currently this program allows the user to acquire up to 4 input values for every scan point in the forward scan direction and up to one input for the backwards scan direction. Acquiring data in the backward scan direction is useful in identifying AC pickup, examining piezo hysteresis and looking for true topography. AC pickup will often appear as tilted stripes through an STM image but the tilt of these stripes will be reverse in the backscan image. Piezo hysteresis will appear at the edges of the forward and back scans where the STM tip is being forced to change direction. True topographic images should look almost identical in the forward and back direction, but it must also be noted that any tip asymmetry(topographic or electrical) can cause image distortion between forward and back-scanned images. In a typical scan both STM tunneling current and feedback voltage will be monitored in the forward scan direction and feedback voltage can be monitored in the back scanning direction.

A unique feature of this scanning program is its ability to compensate for large variations in surface topography and nonlinearities in piezo response. This allows very large images to be taken, images up to $5\mu m^2$. This is accomplished by fitting the scanned surface with a set offset, a plane or an nth order polynomial of x and y. After a surface is scanned it can be fit with any one of these surfaces, where the surface type would be chosen to compensate for sample tilt or the parabolic behavior of the scanning piezo when scanned over large distances. After the surface

---

[1]When a scan begins, the tip is moved to the bottom/left quadrant of the scan area. It then scans one line forward, then back in the primary scan direction. It then increments in the secondary scan direction and does the next scan in the primary direction. This process it iterated until the scan is complete and the tip is in the upper/left quadrant of the scan range. Finally the tip is restored to the center of the scan range(0 V on the primary and secondary outputs).

149
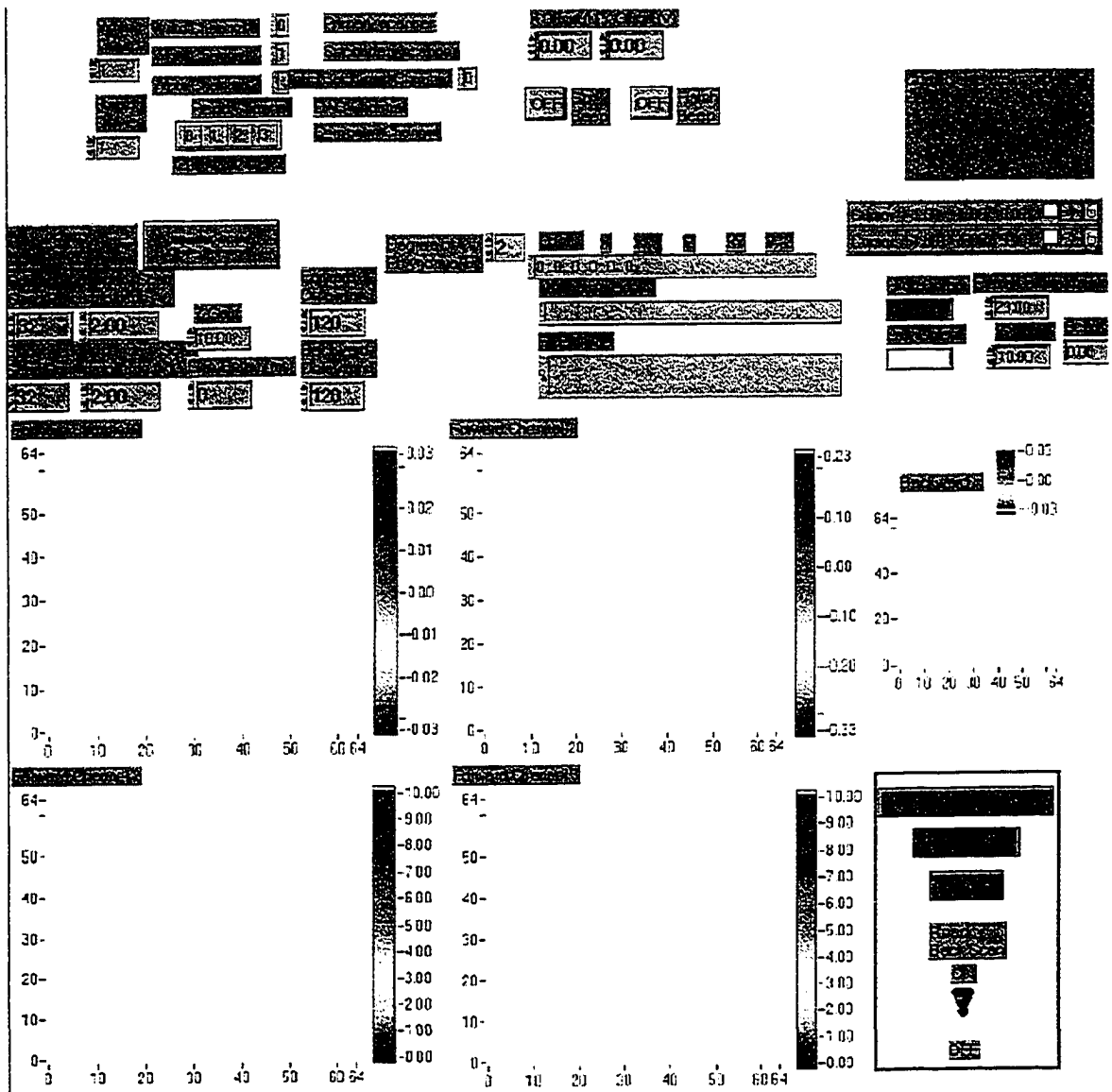
Figure A.4: User interface for the program 'STM Scan w/N-Regression v3.4' used for large slow STM scans.

is scanned and fit the fit parameters are displayed in the 'Measured Coeffs' box on the user interface. If these parameters are copied and pasted into the 'Coeffs' box directly above the measured values, the following surface scan will include an output compensating voltage to the z piezo so that the piezo will be adjusted for sample tilt and the natural parabolic motion of the tip. In this way we greatly reduce the feedback voltage range required to do large area surface scans. The 'Measured Coefficients' are effectively dimensionless, so that once they have been measured for a set scan range and scan points, one can change both these values and still scan along the same plane or surface. In practice one could scan a relatively small area, say 100 nm^2, calculate the sample tilt and then start scanning larger and larger areas adjusting the fitting parameters as the scan range is increased. A second order polynomial fit is suitable for large area scans.

In order to take advantage of the tilt and piezo compensation the scanning program must have access to 3 digital to analog output channels. Typical National Instruments DAQs(data acquisition cards) have only 2 analog outputs so 2 DAQs were used with this program. In order to synchronize outputs between the two boards a simple LabView module was used which updates the voltage value of each analog output sequentially one after another. This ensures that each channel is updated before each measured input value is taken. The disadvantage of this process is that scans are quite slow to acquire(taking about 2 minutes for a 128x128 point scan). Due to these concerns the program 'STM Scan w/N-Regression v3.4' should only be used where slow scans are acceptable and large scan areas are required. These two parameters don't really conflict though, since for large scans the tip velocity over the surface is quite large and should be limited to within the bandwidth of the feedback system. So for large scans, slow scans are in fact necessary(2 minutes for a 128x128 scan on the order of $1\mu m^2$ is quite reasonable). When scanning small areas looking for atomic resolution it can be necessary to scan very quickly to minimize thermal drift. For small scan areas it is not that important to compensate for surface tilt or the parabolic motion of the piezo scan tube as the angular variation of the piezo tube is minimal. To optimize small area scanning, another scan program was developed.

'Scan Executioner 2.0' found in the STM2_lib.llb library was developed for small area fast scans. The user interface for this program is shown in Figure A.5 Examining the user interface for the Scan Executioner program a few differences will stand out. First is the 'Rate' control which sets the speed with which scan channels are up-dated. The value 1000 is the maximum setting for this control and corresponds to

151
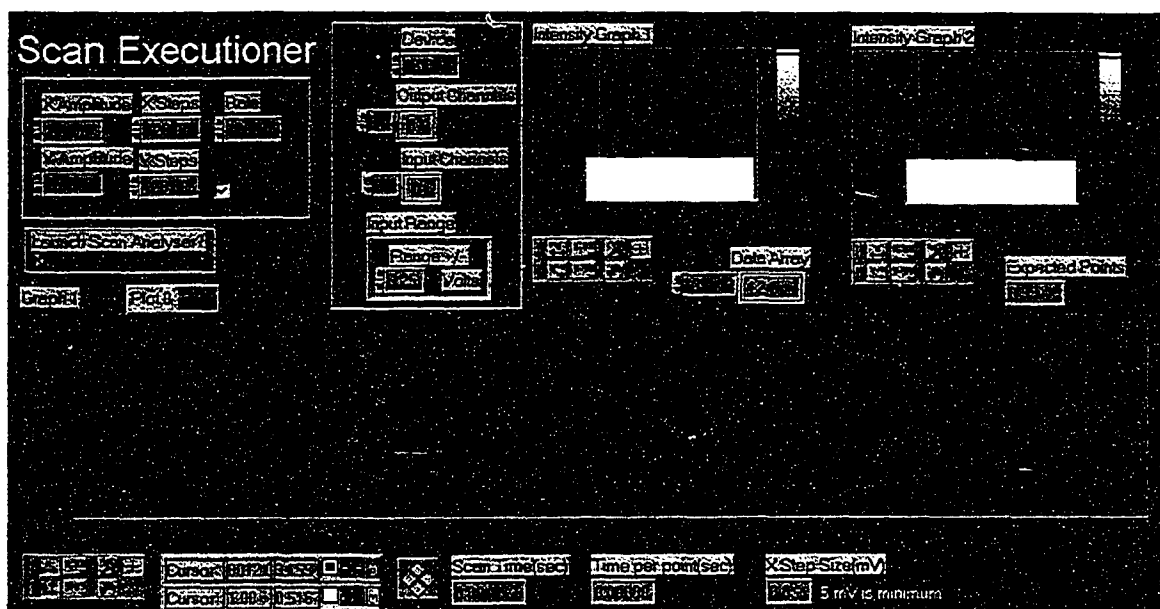
Figure A.5: User interface for the program 'Scan Executioner 2.0' used for small fast STM scans.

1000 updates per seconds[2] giving 128x128 scan times of about 30 seconds. The way Scan Executioner works is in fact quite different from the previously discussed STM scan program. First the user input the desired scan range and scan steps, then the Scan Executioner passes these values to a subroutine called Scan Matrix Generator. This program generates the entire matrix of voltages to be scanned over and passes them back to the Scan Executioner. The matrix is then passed to the Scan Initiator subroutine. This subroutine loads the matrix into memory(through DMA) on the DAQ and programs the DAQ to output matrix values while concurrently taking input values at the desired 'Rate'. The DAQ then begins executing at a rate independent of operating system interrupts and other OS functions. In this way the DAQ acquires data in real time. Once the input data has been gathered it is passed back to the PC(via DMA) and into the scan executioner program where it is displayed in Graph 1. When the data is displayed it is wise to check the length of the data array versus the 'Expected Points' indicator just to check that all the data got through . The scanner scans forward and backward each line in x before it increments y. All the raw data is shown in Graph 1 and simultaneously parsed into Intensity Graph 1 and Intensity Graph 2[3].

---

[2]since 2 channels are being updated for every point in the scan this corresponds to about 2 ms per point.

[3]The Data in Intensity Graph 2 has been reversed so that the positive x direction in both intensity graphs is the same.

152

Another feature in this scanning program which aids in scanning small features is the variable gain control over analog input. Input gain is adjusted by changing the input range from ±10 V to ±50 mV. Unfortunately there is no such gain control for output voltages and one must take care to ensure the voltage step size being output is not too small. The maximum output range of the 12 bit DAC(digital to analog converter) is ±10 V, which gives a minimum output voltage increment of 4.8ᵃ mV. It is always a good idea to check the value of the 'X Step Size(mV)' indicator, since it should ideally be an integral multiple of 4.88 mV so that the x voltage increments the same amount with every scan point. Under special circumstances it might be desirable to scan without the feedback on so there is a control on the front panel to allow this. If saving data, curve fitting or other types of analysis are desired one can enable the 'Launch Scan Analyzer?' button which will pass the acquired data to the next important scanning program.

'Scan Analyzer 2.0' can be found in the STM2_lib.llb library and is shown in Figure A.6 Scan Analyzer allows a few useful data fitting choices, line by line fitting where the slope of each line of data is adjusted to zero is useful for small scans at room temperature where constant thermal drift can mask out small topographic variations such as atomic corrugations. Line by line fitting will occur if the 'Line by Line fit' button is depressed. Polynomial surface subtraction of any order(order is set by the 'Degree of Polynomial Fit' button) can also be performed simply by pressing the 'Poly Subtract' button for the appropriate data channel. If neither button is pressed then the raw data will appear in the 'Forward Fit Data' graph. The raw data as taken from the Scan Executioner program is shown in the 'Data Array' graph and a Fourier transform of this data is shown in the 'Fourier Transform of Data Array' graph. It should be noted that this Fourier transform will include the scan rate frequency and all its Fourier component. The Fourier transform will often aid in eliminating noise sources from the STM signal[4]. In addition to surface topographic scans STMs can probe sample LDOS through current voltage spectroscopy. They can also probe surface contamination through current gap height spectroscopy.

A.4 STM I/V and I/Z spectroscopic scanning

The primary controlling program used for these scan types is 'I / (V or Z) Curve 3.1' found in the STM2_lib.llb library and shown in FigureA.7. This program operates in

---

[4]The LabView program Spectrum_Analyzer_3_0.vi can be used to get real time Fourier analysis of the STM current or any other signal of interest

153
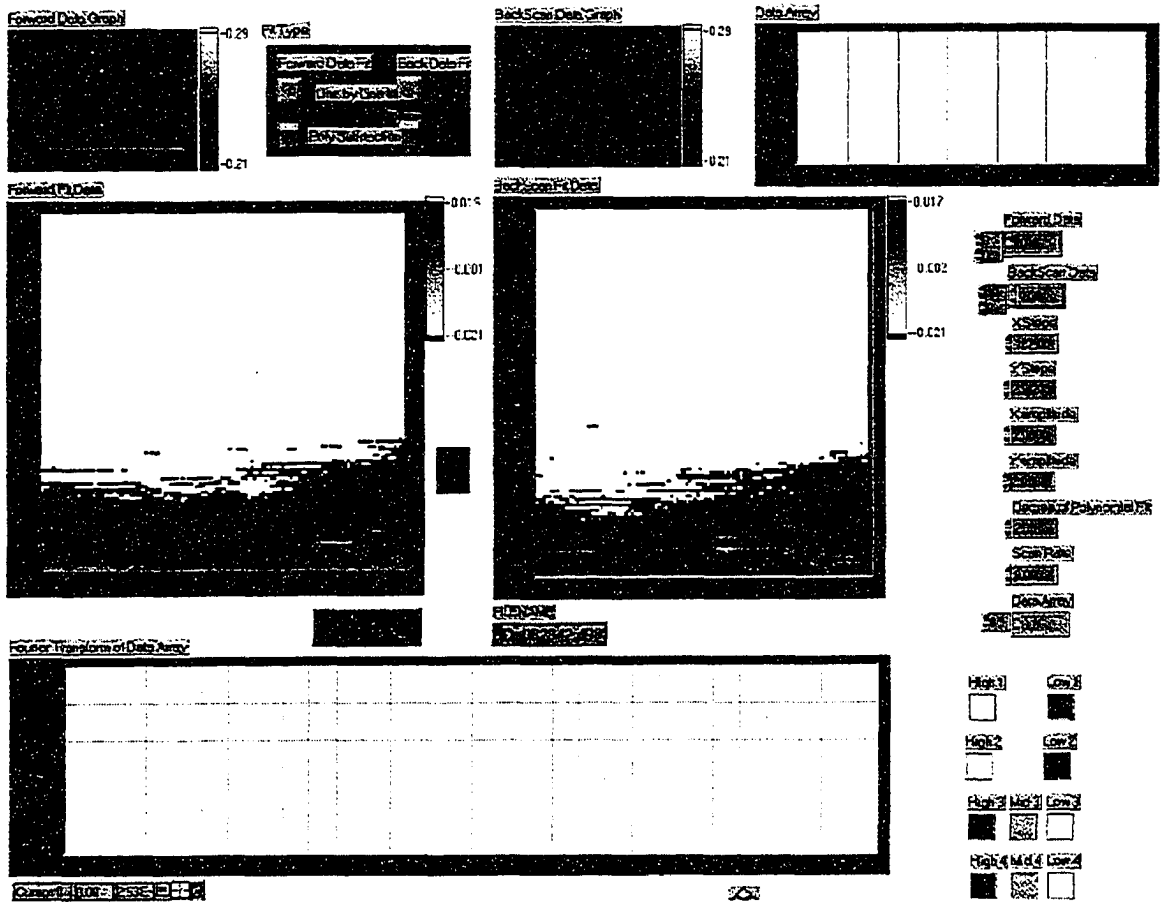
Figure A.6: User interface for the program 'Scan Analyzer 2.0' used to save and fit data acquired through 'Scan Executioner 2.0'.

154
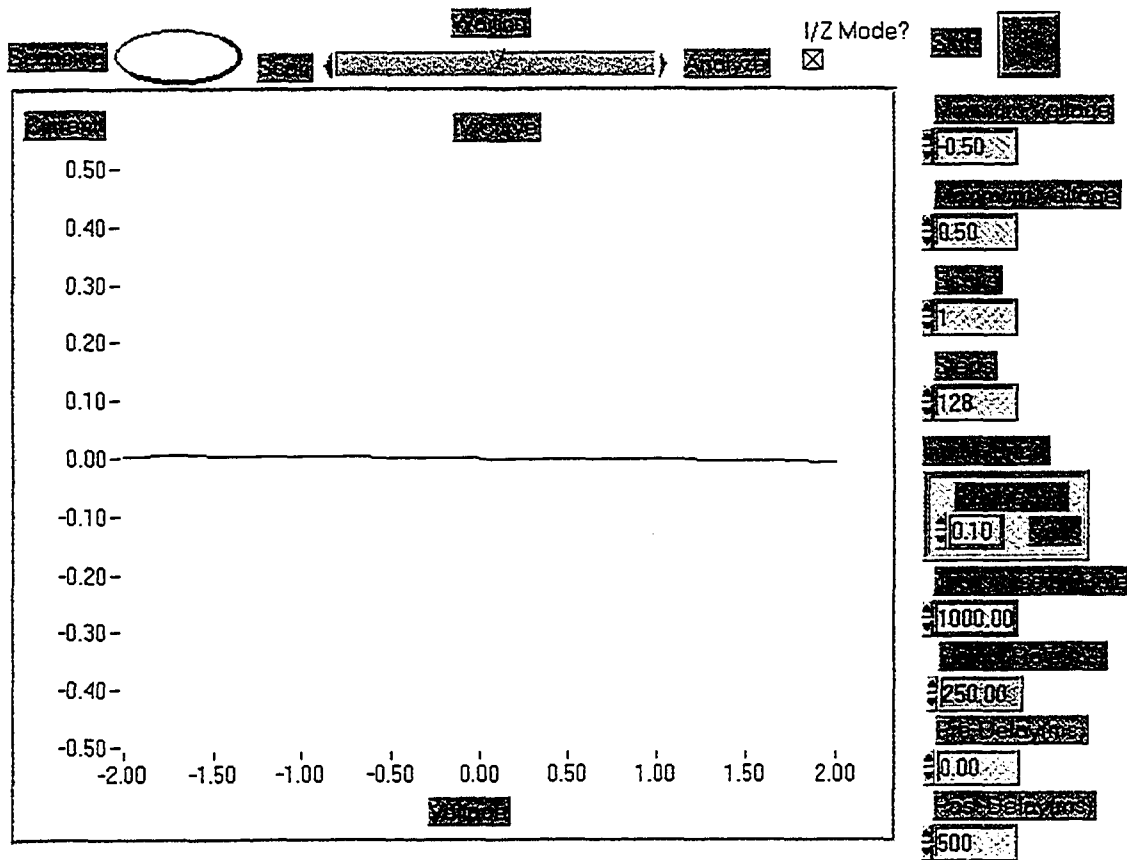
Figure A.7: User interface for the program 'I / (V or Z) Curve 3.1' used to acquire I/V or I/Z spectroscopy curves.

155

the same manner as the Scan Executioner program. A scan matrix is set using the 'Minimum Voltage' and 'Maximum Voltage' controls, and the 'Steps' control. Input gain can be adjusted using the 'Input Range' selector. Scan rate can be set for both the forward and backward scanning directions, using the 'Transmission Rate' and 'Return Rate' controls. This program is capable of performing individual scan but if more scans are required(due to signal noise) multiple scans can be taken and are averaged automatically. While these scans are being taken the STM feedback system is disabled through a TTL digital I/O line. If 'I/Z Mode' is selected the feedback system will be enabled after the I/Z scan has withdrawn the tip. The tip will then be returned to its initial position with the feedback active, to avoid tip crashes due to thermal drift. After a good scan has been captured, clicking on the 'Analyze' slider will cause the program 'I / (V or Z) Analyzer 2.0' found to be launched.

Shown in Figure A.8 'I / (V or Z) Analyzer 2.0' is capable of fitting curves with linear, polynomial or exponential curves in order to analyze sample electrical properties and tunneling conditions such as the effective tunneling work function. This program also allows I/V or I/Z data to be saved. Operation of this program is quite simple, one simply selects the desired polynomial order or exponential polarity(whether the current values are positive or negative) and then click on the 'Polynomial' or 'Exponential' slide bar positions. Once a fit is suitable click on the 'On'/off switch to stop the program, prompting the user to save the data. The program can always be restarted to re-fit the data. The range of data to be fit can also be adjusted through the 'Fit Range' control.

A.5 Optical delay line scanning

The last piece of STM control software to be discussed is the program which controls the laser pulse delay in a time-resolved STM(TR-STM) experiment. In TR-STM experiments an STM image will be acquired which typically includes topographic information, STM current over the scan, and the time-resolved STM signal as detected by the lock-in amplifier. All this data will be taken for a given delay time(or retroreflector position) which will then be incremented to build a time-resolved movie. The program which controls the movement of the optical delay line can be found in the library STM2_lib.llb and is called 'Motor Control 2.0' shown in Figure A.9. Inputs for this program are given in terms of stepper motor increments and the delay time between increments. It is often more convenient to think in terms of delay times, so a little program called 'Scan Calculator' is run in conjunction with the motor con-

156
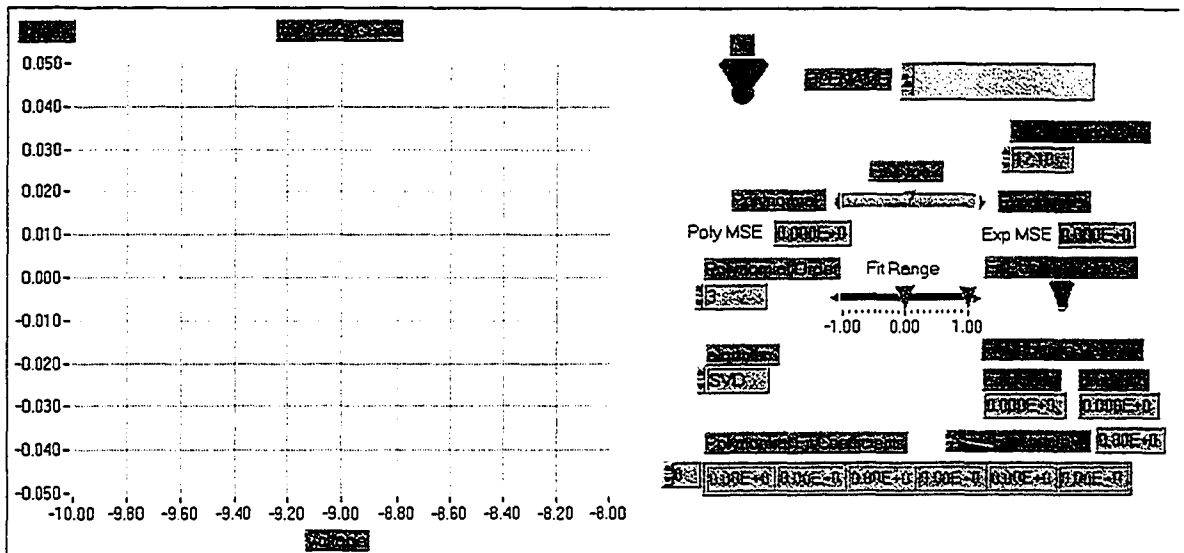
Figure A.8: User interface for the program 'I / (V or Z) Analyzer 2.0' used to fit I/V or I/Z spectroscopy curves.

trol program. 'Scan Calculator' also shown in Figure A.9 allows one to simply input the start and stop delay times for the scan, it then calculates the appropriate motor starting point in steps, and the increment interval. It was found that this program yields the best results if all scans are taken in the same direction. In order to compensate for any mechanical backlash, the 'Roll Back' control can be set to pretension the delay line translation stage to minimize slop between scans. 'Motor Control 2.0' uses a simple data file called

c:\motor.dat

to keep track of the position of the stepper motor. Care must be taken to ensure that the stepper motor is never asked to move the retroreflector past its mechanical limits. There are currently no safeguards to prevent this. There are three modes which this program runs in. The modes, set in the 'Increment Options' control are:

- Take Data Point

- Take Data Point and Pause

- Pause

These options control what the program does after moving the retro one set of increments. If the program is caused to pause, a subroutine is launched which waits for user intervention to continue. This is so that an STM scan could be performed while the delay is held fixed. The 'Scan Info' section on the user interface is simply a

157
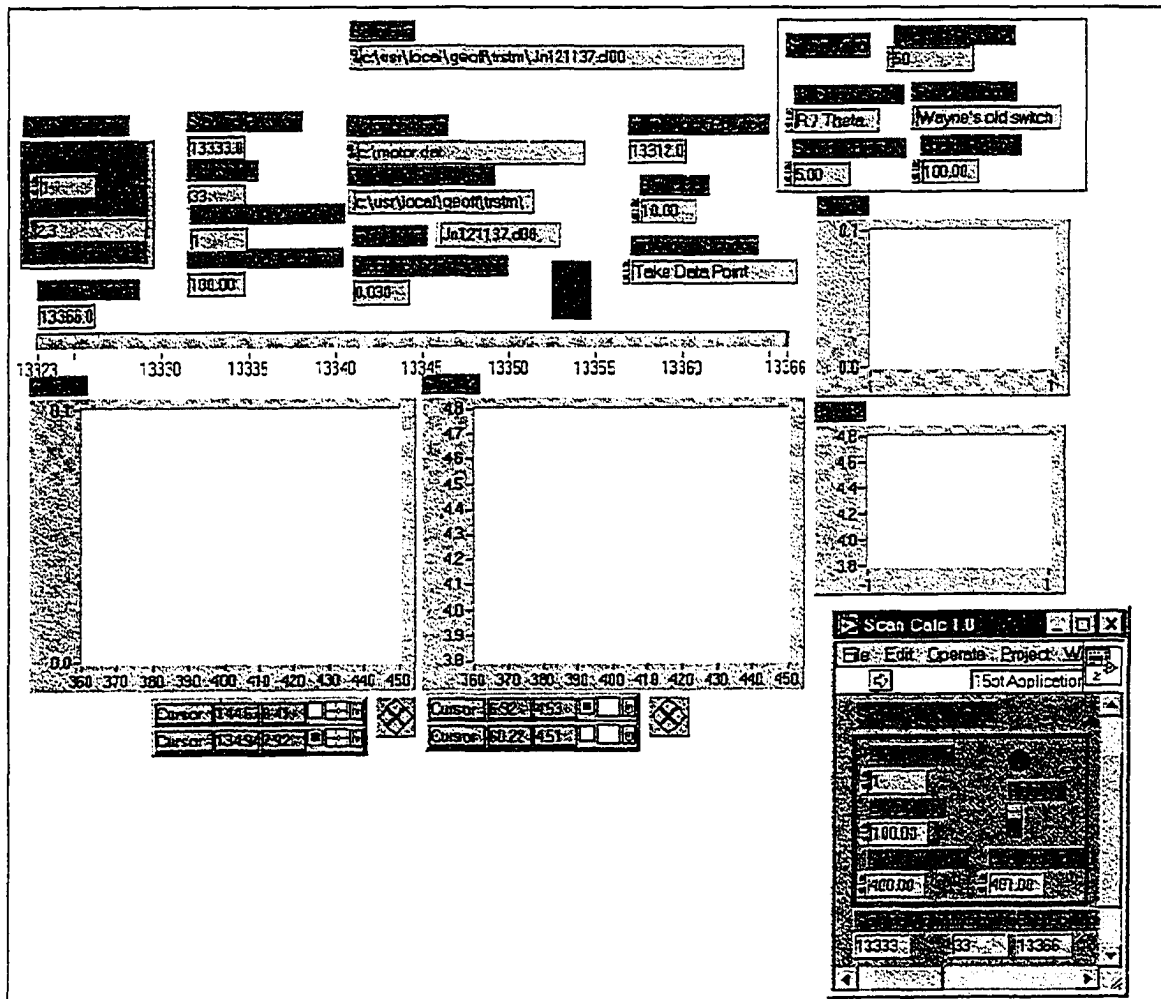
Figure A.9: User interface for the program 'Motor Control 2.0' used to acquire time resolved data and control the delay time between pump and probe optical pulses. The interface for 'Scan Calculator' is also shown.

158

convenient way for the user to input details about the time resolved scan which will be printed along with the scan results. It serves no functional purpose.

159

Appendix B

Junction Mixing STM Optical Systems

B.1 The Ti/Sapphire Laser

In order to time-resolve the operation of a scanning tunneling microscope, optical pump probe techniques were used. These techniques relied on fast(60 femtosecond) laser pulses delivered at 87.7 MHz to electro-optic switches. In order to produce these laser pulses a Titanium doped Sapphire(Ti/Sapph) laser was constructed. Optical component layout, alignment and performance diagnostics will be detailed in the following sections. Trouble shooting symptoms and known cures will also be outlined.

The pulsed output of a Ti/Sapph laser is a remarkable phenomena. Pumping a Ti/Sapph laser with continuous green laser light can produce continuous lasing or a single pulse propagating within the cavity. Even more remarkable is that the transformation from continuous to pulsed operation can be accomplished with the flick of a finger. Before it was first discovered there was general agreement that Ti/Sapphire lasers could not self mode-lock. However the serendipitous discovery of what was to be called "magic" mode-locking was published in 1991 [1]. After this discovery, the group of Salin, Squire and Piche developed the theory of Kerr induced self focusing [2]. To learn the physics of this feat, I would refer the reader to the subject of Kerr lens mode locking or to texts such as "Ultrashort Laser Pulse Phenomena" by Diels and Rudolph [3]. Here we will gloss over the physics with a simplified model. The Ti/Sapph crystal can emit a broad range of wavelengths anywhere from 680 ⇒ 1100 nm. The wavelengths which satisfy the condition that an integer number of half-waves fit into the cavity form the longitudinal modes of the cavity. In CW mode a fairly narrow set of longitudinal cavity modes dominate the lasing, typically a band of modes a few nm wide centered around 800 nm. When an

optical power spike is introduced into the cavity something remarkable can happen. When this noise spike passes through the Ti/Sapph crystal the strong electric field interacts non-linearly with the crystal, modifying its index of refraction. This is Kerr lensing or self focusing, and will increase the overlap of the lasing area with the pump beam. This will increasing the stimulated emission of the crystal as the noise spike passes through, increasing the amplitude of the spike. With every pass in the cavity the amplitude of the noise spike will build as the self focusing effect channels more energy into a small volume in the crystal. Soon this effect will completely deplete the population inversion in the most active volume of the crystal. This leads to the formation of a short pulse in the cavity and can decrease or eliminate the CW power in the cavity. CW power can still propagate in the cavity if there are many transverse CW modes so that the self focused spot on the crystal does not completely overlap with the CW spot. Using an adjustable slit within the cavity allows one to kill any remaining CW component in the pulsed Ti/Sapph beam.

The Ti/Sapph laser described here was built based on the design paper by Kapteyn and Murnane [4] [1]. Lasing is accomplished by creating a population inversion in the Ti/Sapph crystal by optically pumping it with another laser. In this case a 5 Watt, Spectra Physics Millennia(at 532 nm wavelength) is used at 4.5 W power in the TEM_{00} mode for normal operation. Note that the polarization of the Millennia must be rotated from vertical to horizontal so that it will be oriented properly with respect to the orientation of the Ti/Sapph crystal. Our efforts using argon-ion lasers were never successful in producing a stable pulse Ti/Sapph output since there was insufficient power in the TEM_{00} mode. Pumping at 5 W the Ti/Sapph gives an output power of 800 mW continuous wave(CW) power(not pulsed). Mode locked, one should be able to get from 400 $\rightarrow$ 500 mW pumping at 5W. Normal operation has the pump power at 4.5 W and the Ti/Sapph pulsed output power at about 400 mW. Apart from the Ti/Sapph crystal and the slit the only other important parts of the Ti/Sapph cavity are the end mirrors and a pair of prisms which are used to compensate for group velocity dispersion within the cavity. A schematic of the cavity used in the present experiment is shown in Figure B.1.

Alignment of the Ti/Sapph cavity was performed as outlined in reference [4]. The speed with which one can align the laser from scratch is simply a matter of experience. With experience one should be able to completely align the laser within the course of

---

[1]In this paper the authors welcome people to contact them for updates of the document. Since they now sell these lasers commercially it is unclear if this policy still holds.
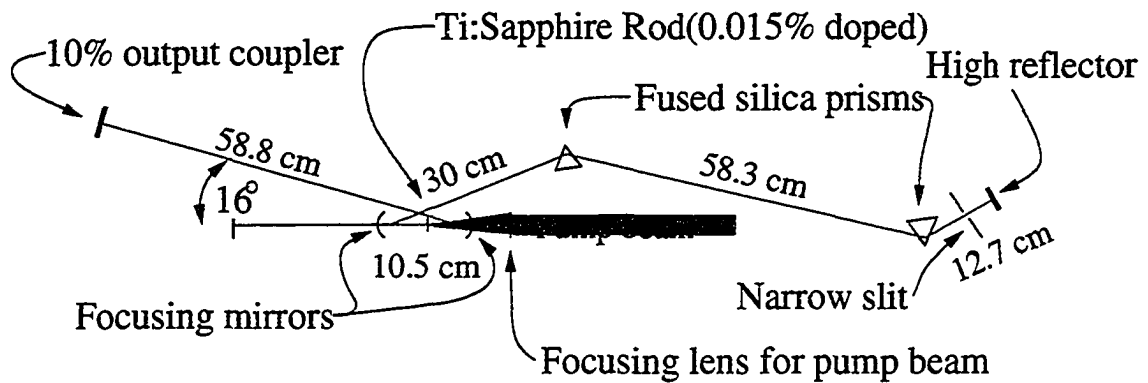
Figure B.1: A schematic of the Ti/Sapph Cavity

a day. Emphasis should be placed on the first few steps of the alignment process since these will be the most difficult to correct. Ensuring that the pump beam correctly passes through the center of the cavity optics is of great importance. Also ensuring that cavity optics translate parallel to the beam path is of great import. Take great care with the pump focusing lens, the Ti/Sapph rod and the two focusing lenses. Once the cavity is properly aligned mode-locking can be achieved by tapping the output coupler, while translating the left most focusing mirror. A great help in this process is an extra-cavity diffraction grating projecting the diffracted laser output onto a phosphor screen. While translating the left focusing mirror the diffracted beam will change shape and hop frequencies. Often when the beam is in this meta-stable state hopping between 2 frequencies, a simple tap will lock the cavity modes, producing a thin horizontal line in the diffraction pattern. Another great help is a relatively fast photo-diode placed behind the high reflector(a small amount of laser light will escape the cavity through the high reflector). Using this photo-diode and a fast oscilloscope one can often see small pulses developing when the optics are close to a mode-locked configuration, these pulses are shown in panel a) of Figure B.2. At this point, a tap on the output coupler should initiate mode-locked operation, seen with a photo-diode as panel b) in Figure B.2. When attempting to mode-lock the laser it will probably be necessary to open up the intra-cavity slit and increase pump power to 5 or 5.5 Watts. Once mode-locked operation has been initiated, try to optimize power and pulsed stability by adjusting the pointing of the output coupler, the high reflector, both focusing mirrors(position and pointing), the focus of the pump beam the position of the Ti/Sapph crystal, the amount of prism glass in the cavity(for each prism), the center position of the slit and the size of the slit.

162
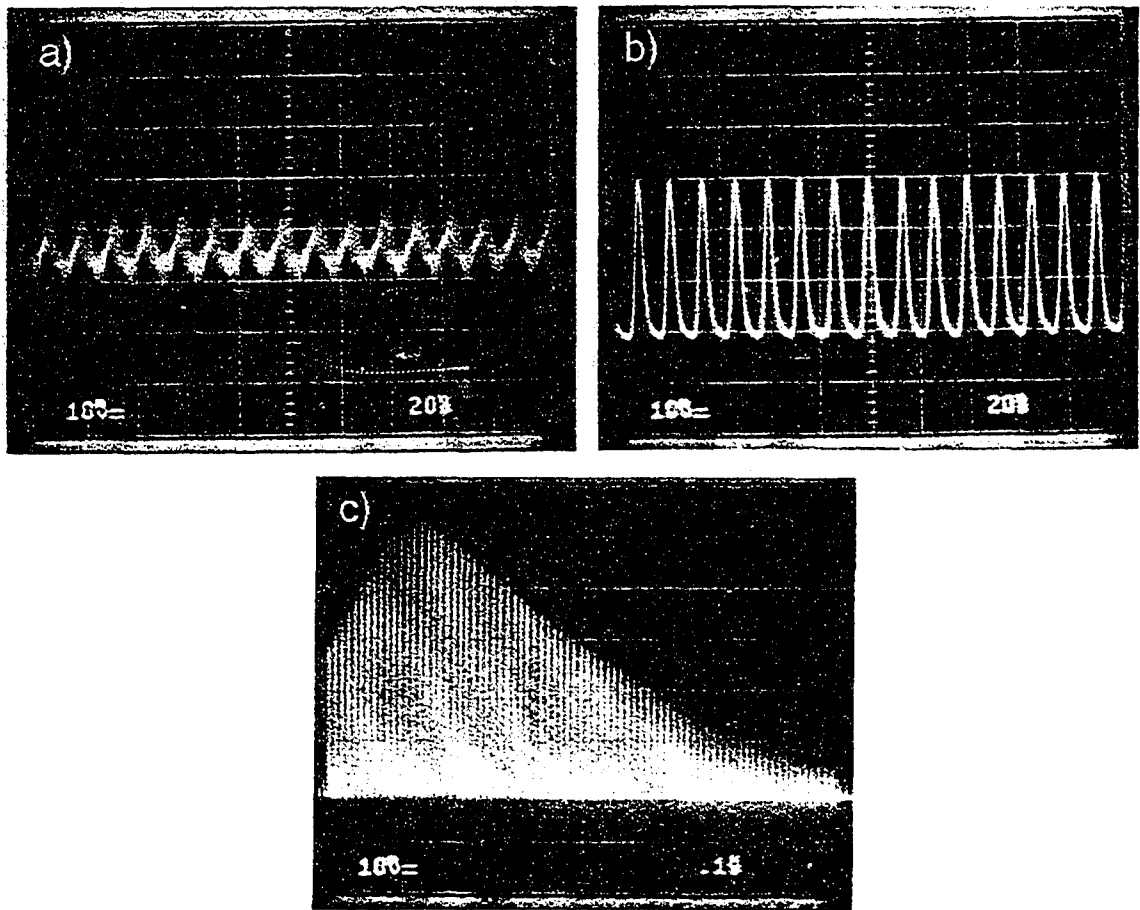
Figure B.2: Ti/Sapph pulses as measured with a fast photo-diode: a) Pre-mode locked diode signal b) Mode-locked diode signal c) Slow modulation of improperly mode-locked signal

163

Once the Ti/Sapph is mode-locked there are a number of diagnostics which must be performed to ensure the laser is working properly. The first and simplest thing to check is the photo-diode signal. One should see strong and constant amplitude pulses on the oscilloscope spaced by the duty cycle of the laser(13.1 ns). Sometimes one will see additional pulses within the 13.1 ns cycle, or a pulse train spaced at 13.1 ns consisting of alternating amplitude pulses. Another interesting observation with the photo-diode is the 13.1 ns spaced pulse train enveloped in an oscillatory wave μs in duration, modulating the pulse intensity by as much as a factor of 10 shown in panel c) of Figure B.2. These strange behaviors can often be corrected by adjusting slit width or the dispersion compensation (by changing the amount of glass from each prism in the cavity). If everything looks good coming out of the photo-diode, another necessary diagnostic step is to examine the pulses using an auto-correlator. An auto-correlator will allow us to measure the pulse width and determine whether any additional pulses are propagating in the cavity nearly coincident in time with the main pulse. These additional pulses can often be eliminated by reducing the pump power in to the cavity. Figure B.3 shows the output of a fast photo-diode in the panes on the left, and the auto-correlator signal in panes on the right. Examining these traces we see that the diode signal in all three pulse modes look nearly identical (panel a), c) and e)) while the autocorrelated signals show stark contrast. Only panels e and f correspond to what looks like normal Ti/Sapph pulsed operation.

The last standard diagnostic is the use of the Reiss spectrum analyzer. This tool provides another way to measure the pulse width through calculations on the band width of the pulses. The Reiss allows us to see whether CW components are present in the mode-locked beam. This problem can normally be corrected by reducing pump power or by adjusting the slit position or reducing slit width, and if this does not work, translating the crystal towards the pump beam has been effective. The Reiss has also allowed us to determine whether two mode-locked pulses are present in the cavity at different wavelengths. Together these three diagnostic tools have allowed us to ensure the correct operation of the mode-locked Ti/Sapph laser system. One missing component in this analysis is a tool to measure the chirp of the mode-locked pulse, though since we are not concerned with performance faster than hundreds of femtoseconds this should not be a concern.

B.2   The 8× Pulser

For some applications, it was determined that there was excess pulse power coming from the laser. Rather than attenuating this power we endevoured to beam-split these

Figure B.3: Photo-diode and auto-correlator pulse traces for 3 modes of Ti/Sapph output configurations(one mode is shown for each horizontal pair of traces. Only e) and f) show the correct photo-diode and auto-correlator behavior.

165

Mirrors
50/50 Beamsplitters   Output Beam
Half waveplate
Polarizing Beamsplitter

Input Beam

Figure B.4: Schematic of the 8× pulser.

laser pulses and offset them by differing time intervals to increase the laser repetition rate. Thus the 8 × Pulser was developed, which splits an incoming laser pulse into 8 mini-pulses which are delayed evenly across the original laser duty cycle(increasing the laser repetition rate to 8 × 87.7 = 701.6 MHz). The design and layout of the 8 × Pulser is shown in Figure B.4.

The input pulse train, coming from the left hits a beam splitter and half the beam moves up and right to a mirror which directs the half pulse train towards the next beam splitter. The other half of the beam moves down and to the right, onto a mirror 4.5" past the vertical one. It is then reflected towards a large 2" diameter mirror at almost normal incident angle. From there it reflects back tracing a slightly modified path which intersects with the vertical mirror directing the half pulse train towards the second beam splitter. 2 pulse trains will intersect with the second beam splitter. One from above, with no relative delay and the second from below with a $\frac{1}{8}$ duty cycle delay [2]. The second beam splitter will break these pulse trains into 4, and introduce additional delays to 2 of the 4 pulse trains. Incident at the third beam splitter from above will be trains with 0 and $\frac{1}{8}$ duty cycle delays. Incident from below will be trains with $\frac{2}{8}$ and $\frac{3}{8}$ duty cycle delays. Following the the third beam splitter additional delays are added to 4 of the 8 beams introducing beams with delays of $\frac{4}{8}$, $\frac{5}{8}$, $\frac{6}{8}$ and $\frac{7}{8}$ of the duty cycle. In order to recombine all the pulse trains, a half wave plate is used on the final arm of the 8 × pulser to rotate the polarization of 4 of the 8

[2]Figure B.4 is configured for a 13.1 ns duty cycle

166

pulse trains. A polarizing beam splitter is then used for recombination. To aid in the design of the system a simple mathematica notebook was created to try out various values for the dimensions of the 8 × Pulser. Two of the design considerations which were used in the current version were to make the unit as small as possible and to use one optic to reflect all three beams in the delay arm to reduce the system cost. The notebook is shown in Figure B.5.

The current design for the 8 × Pulser has every optic mounted on a gimbaled mirror mount which can be tilted in two planes. With this configuration it is possible to align the system such that the output beam is a collinear superposition of all 8 pulse trains. The precise timing of each pulse train was not determined, and with the current optical setup this could not be easily adjusted. To facilitate the time alignment of this system the single retro mirror should be replaced with three smaller retro mirrors, each mounted on its own translation stage. This should allow each delay stage to be accurately set to the correct delay time. In order to analyze the output of the 8 × Pulser one could use a cross-correlator with a long delay line to scan a pulse from the original Ti/Sapph output across the pulse train. A better approach would be to use a fast photo-diode and fast oscilloscope to directly image the pulse train(Unfortunately this approach will not give precise information on the pulse separations).

References

[1] D. E. Spence, P. N. Kean, and W. Sibbett. *Opt. Lett.*, 16:42, 1991.

[2] Francois Salin, Jeff Squier, and Michel Piche. *Opt. Lett.*, 16:1674, 1991.

[3] Jean-Claude Diels and Wolfgang Rudolph. *Ultrashort Laser Pulse Phenomena.* Academic Press, San Diego, 1993.

[4] Margaret M. Murnane, Henry C. Kapteyn, Chung-Po Huang, and Melanie T. Asaki. Mode-Locked Ti:Sapphire Laser Rev 1.7. Technical report, Washington State University, 1994.

```
In[63]:= (* dutycycle = First specify the duty cycle,
          the program outputs the corresponding optical delay in inches *)

          dutycycle = 13.1; delayininches = dutycycle * 10^(-9) * 3 * 10^(8) * 100 / 2.54

Out[64]= 154.724
```

```
(* base = Now specify the base unit of displacement (inches), ie. to move from one beamsplitter to
   another move 2 * side in the x direction.  To move from the first beam splitter to the first vertical
   mirror move 1 * side in the x direction and 1 * side in the negative y direction.  *)
(* m =
   the horizontal distance between the vertical mirror and the large retro mirror (inches).  If the retro-
   mirror is to the left of the vertical mirror then m is positive.  *)
```

```
In[81]:= base = 6.1; m = 2;
```

```
(* x is the lenght of each side,
   ie. distance from the first beam splitter to the first vertical mirror *)
```

```
In[68]:= x = Sqrt[2 * base * base]

Out[68]= 8.6267
```

```
(* delayn = these delays are the lengths
   (inches) necessary for the beam path segment going from the vertical mirror,
   off the small redirection mirrors toward the retro mirror, and to the point from which m is measured *)
```

```
In[70]:= delay1 = delayininches / 8 - 2 m
          delay2 = delayininches * 2 / 8 - 2 m - 2 Sqrt[2] x
          delay3 = delayininches * 4 / 8 - 2 m - (2 + 4 Sqrt[2]) x

Out[70]= 15.3406

Out[71]= 10.2811

Out[72]= 7.3088
```

```
In[73]:= (* distn = these are the distances from the vertical mirrors to the small redirection
          mirrors (along the 45 degree beam path *)
```

```
In[74]:= dist1 = delay1 / (2 + Sqrt[2])
          dist2 = delay2 / (2 + Sqrt[2])
          dist3 = delay3 / (2 + Sqrt[2])

Out[74]= 4.49314

Out[75]= 3.01127

Out[76]= 2.1407
```

```
(* mirror_separationn = these are the vertical
   separations between the spots where each pulse train will arrive on the retro mirror,
   we want the 3 beams to be evenly separated *)
```

```
In[78]:= mirror_separation1 = (dist1 - dist2) * Sin[45]
          mirror_separation2 = (dist3 - dist1) * Sin[45]
          mirror_separation3 = (dist3 - dist2) * Sin[45]

Out[78]= 1.26094

Out[79]= -2.0017

Out[80]= -0.740769
```

Printed by Mathematica for Students

Figure B.5: Mathematica notebook for calculating the geometry of the 8 × Pulser.

168

Appendix C

Modifications to the Junction Mixing Model

C.1 Modified Model

The transmission line model used in the calculations of Chapter 4 was simplified to a single resistive element Z, between the voltage source V(t) and the tunnel junction. For low frequency voltage pulses this model is reasonable. At low frequencies the resistance of the tunnel junction is on the order of 10^6 times larger than the impedance Z so that the voltage at the tunnel junction is identically V(t). At high frequencies however, the impedance between the tip and sample becomes comparable to the impedance Z of the transmission line due to capacitive coupling. For example a 3.5 picosecond, 100 GHz electrical pulse sees the 30 fF tip sample capacitance as a 53 Ω impedance. The original model crudely accounts for the "loading" of the transmission line by the tip through the presence of Z. As a next step towards a more realistic model of the transmission line we will introduce another element of impedance. Instead of a single impedance Z between the voltage source and the tunnel junction, the transmission line will be modeled as 2 impedances each with value Z/2 (eventually to be replace by L, R and C per unit length elements). One impedance before the tunnel junction as before but with half its value, and a second after the tunnel junction which terminates the transmission line at a ground. This configuration is shown in Figure C.1.

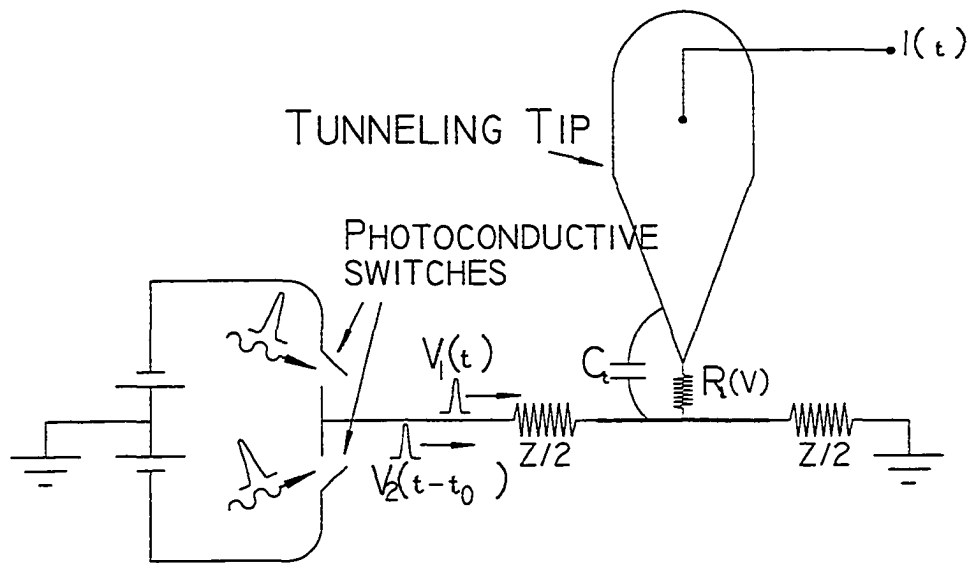A more conventional view of this circuit is shown in Figure C.2. Looking at the

169

Figure C.1: Modified transmission line model, where Figure 4.2 has been changed so that the impedance before the tunnel junction is Z/2 and an additional impedance Z/2 appears after the tunnel junction.
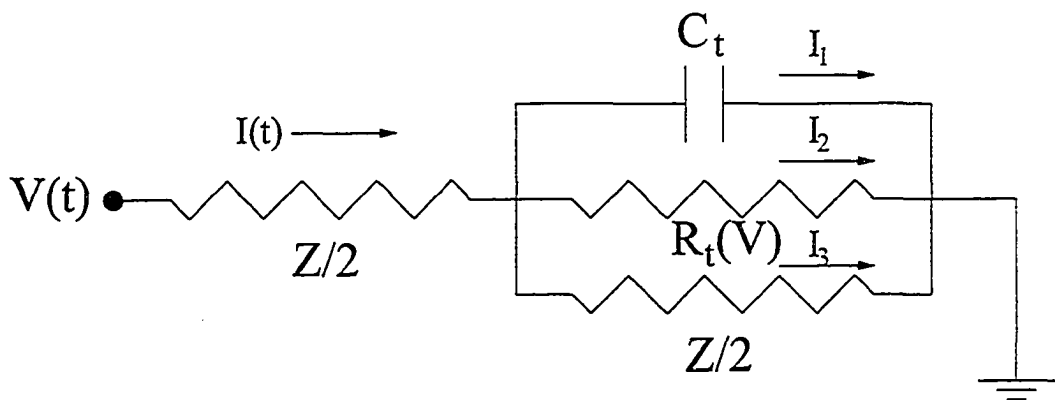

Figure C.2: Simplified circuit diagram for JM-STM model.

170

current through each part of this circuit we write:

$$\frac{dV}{dt} - \frac{dI}{dt}\frac{Z}{2} - \frac{I_1}{C_t} = 0 \qquad (C.1)$$

$$V - I\frac{Z}{2} - I_2 R_t = 0 \qquad (C.2)$$

$$V - I\frac{Z}{2} - I_3\frac{Z}{2} = 0 \qquad (C.3)$$

Where $I = I_1 + I_2 + I_3$ is the total current flowing. Combining these equations to establish a differential equation for $I(t)$ we get:

$$\frac{dI(t)}{dt} = \frac{2}{Z}\frac{dV(t)}{dt} - I(t)\left(\frac{4}{ZC_t} + \frac{1}{R_tC_t}\right) + V(t)\left(\frac{2}{R_tZC_t} + \frac{4}{Z^2C_t}\right) \qquad (C.4)$$

Just as in Chapter 4, we must solve this equation and find $I(t)$ for a given set of electrical pulses given by $V(t)$. Once we have solved for $I(t)$ me must substitute our values into Equation C.2. Since only the current $I_2(t)$ will be detected by the STM. As in Chapter 4, this current must be integrated for every delay time t_0 between pump and probe pulse (in V(t)) to map out the measured time-resolved current signal.

Solutions for the integrated current($\int_{-\infty}^{\infty} I_2(t)dt$) can be found using the original computer code used to solve for the integral of $I(t)$ in Chapter 4. The only modifications necessary, are to use different values for some of the input parameters. The values from the Chapter 4 model, V_0, Z and C_t have to be replaced with $V_0/2$, $Z/2$ and $C_t/2$ in the Appendix C model.

Comparisons between the Chapter 4 model and the model presented here in Appendix C are shown in Figures C.3 and C.4. These figures are comparisons between the calculated fits shown in Figure 4.4 and the new fits produced by the Appendix C model. The only major difference is in the amplitude of the time-resolved current. There are small differences in the pulse shape which will become more significant as the excitation pulses shortened. By nearly doubling the amplitude of the input voltage pulse in the Appendix C model we find good agreement with calculations from the Chapter 4 model.

C.2   Model Code

Bob Teshima's source code for solving for the integrated time-resolved current is published below. The main program of interest is *rbchvhyp.f* which relies on the integration subroutine *intsubs.f* which cannot be published due to copy right regulations. To compile the code use the command:
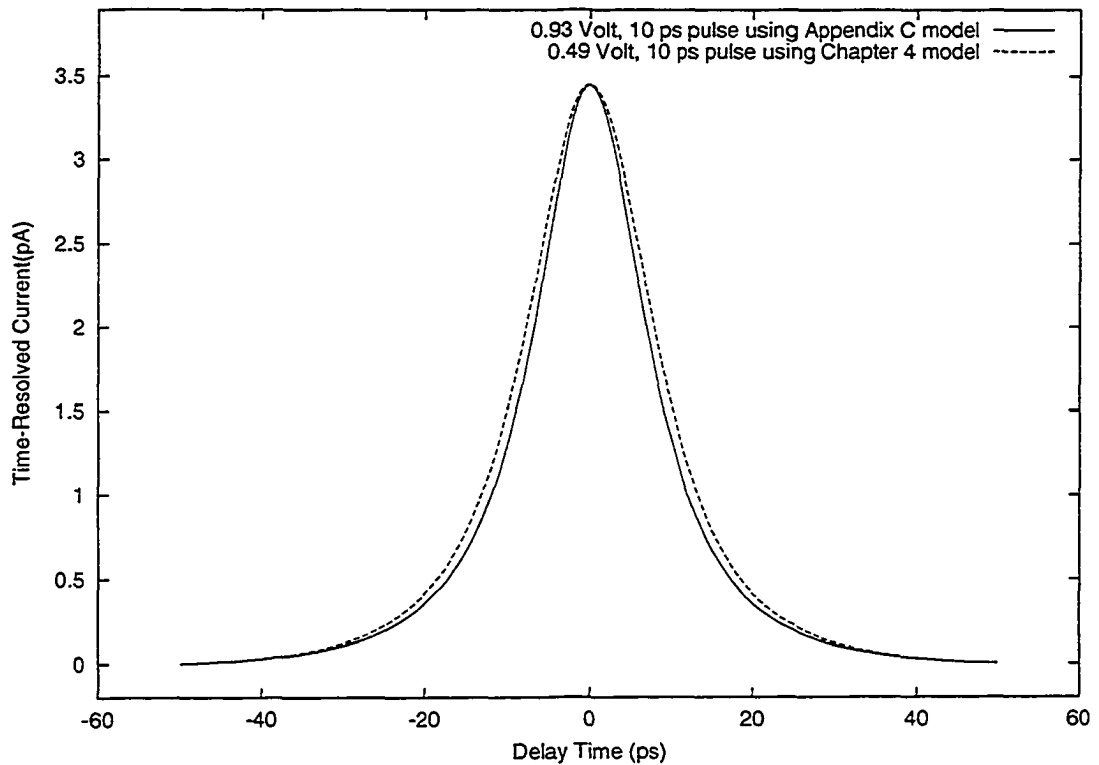
171

Figure C.3: 10 ps pulse model comparison. Input parameters were: Z=68 Ω, C_t = 33 fF, β=5.1 nS, γ=0.75 V^{-2}, t_p=2.8 ps and t_c=10 ps.

```
g77 rbchvhyp.f intsubs.f
```

This will produce an a.out file. A input file is required with the following information on each line:

Line 1: Z (ohms), C (pico Farads), β (Siemens), γ (V^{-2}),

Line 2: V_0 (in Volts), $t_p/2$ (ps) [1], t_c (ps), RERR (relative error)

Line 3: t_0 (ps), increment (ps), # increments,

The input file to generate the 4 ps Chapter 4 pulse shown in Figure C.4 is shown here:

```
68,33e-3,23e-9,1.3,
0.561,1.4,4.5,1e-8,
-50,.5,201,
```

The input file to generate the 4 ps Appendix C pulse shown in Figure C.4 is shown here:

```
34,16.5e-3,23e-9,1.3,
```

---

[1]Note that for t_p = 2.8 ps we would have to enter a value of 1.4 ps into the program. This is because, for historical reasons, there is a factor of 2 in the program multiplying t_p.
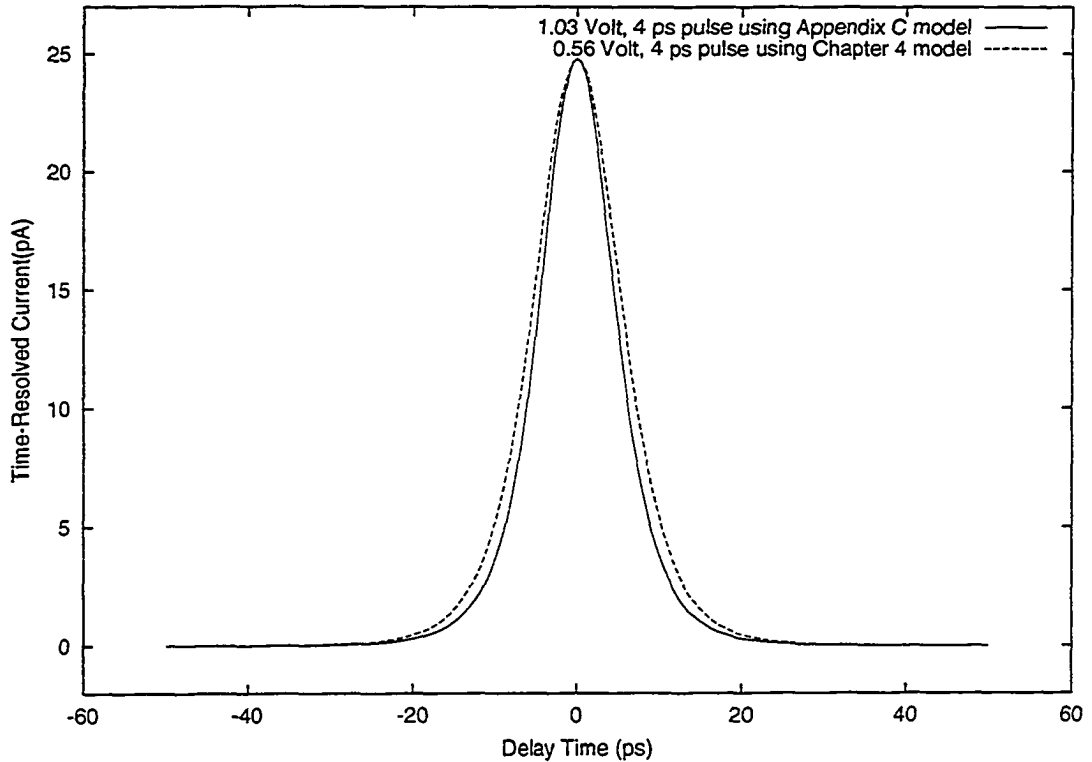
172

Figure C.4: 4 ps pulse model comparison. Input parameters were: Z=68 Ω, C_t = 33 fF, β=23 nS, γ=1.3 V^{-2}, t_p=2.8 ps and t_c=4.5 ps.

```
.515,1.4,4.5,1e-8,
-50,.5,201,
```

to create a data file use the following syntax:

```
a.out < inputfile > outputfile
```

Once an output file has been generated it will need to be rescaled, if one wishes to compare results with experimental data. The current values from the model calculation will need to be averaged over the duty cycle of the laser. In the case of the results shown in Figures C.3 and C.4 the output files were rescaled by dividing by $\frac{13.1ns}{2.8ps} \approx 4679$, the rep-rate of the laser divided by the pulse width. Also note that the DC background was subtracted from the tunneling current, since the STM feedback electronics would do this automatically.

C.2.1 rbchvhyp.f

```
IMPLICIT REAL*8(A-H,O-Z)
COMMON/COMINT/ALF,DMU,DA
EXTERNAL FCTINT
```

173

```fortran
        CALL UERSET(1,LEVOLD)
1       READ(5,*,END=90)Z,C,BETA,GAM
        WRITE(6,200)Z,C,BETA,GAM
200     FORMAT('#',5G15.7)
        READ(5,*,END=90)VO,W1,W2,RERR
        WRITE(6,200)VO,W1,W2,RERR
        ALF=W1/(C*Z)
        DMU=W1/W2
        CALL FVPEAK(DMU,TM,VM,IER)
        VCON=VO/VM
C         VLI=8.DO*VCON*W2
        FACI=VCON**3*(ALF/(ALF-DMU))**2*W1*GAM
        XLIM1=DLOG(0.1DO*RERR)
        XLIM2=-XLIM1/DMIN1(DMU,1.DO)
5       READ(5,*,END=1)DST,DEL,ND
        IF(ND.LT.1)GO TO 1
        DO 20 ID=1,ND
        D=(ID-1)*DEL+DST
        DA=DABS(D)/W1
        CH=DCADRE(FCTINT,XLIM1,XLIM2+DA,0.DO,RERR,ERR,IER)
C         CH=(CH*FACI+VLI)*BETA
        CH=CH*FACI*BETA
        WRITE(6,215)D,CH,IER
215     FORMAT(1X,G15.7,G18.10,I5)
20      CONTINUE
        GO TO 5
90      STOP
        END
        FUNCTION FCTINT(T)
        IMPLICIT REAL*8(A-H,O-Z)
        COMMON/COMINT/ALF,DMU,DA
        VP=VPULSE(T,DMU)+VPULSE(T-DA,DMU)
        FO=VPULSE(T,ALF)+VPULSE(T-DA,ALF)-VP
        FCTINT=FO*FO*VP
        RETURN
        END
        FUNCTION VPULSE(T,DMU)
```

174

```fortran
      IMPLICIT REAL*8(A-H,O-Z)
      DATA PI/3.1415926535897932D0/
      IF(T.LE.0.D0)THEN
      CV=1.D0+DMU
      FN=DEXP(T)
      R=FN/(FN+1.D0)
      FN=FN/((0.5D0*FN+0.5D0)**2*(DMU+1.D0))
      SUMP=FN
      ELSE
      CV=1.D0-DMU
      FN=DEXP(-T)
      R=FN/(FN+1.D0)
      FN=FN/((0.5D0*FN+0.5D0)**2*(DMU-1.D0))
      SUMP=FN+4.D0*PI*DMU/DSIN(PI*DMU)*DEXP(-DMU*T)
      ENDIF
      DO 20 N=1,100
      FN=(N+1)*R*FN/(CV+N)
      SUM=SUMP+FN
      IF(SUM.EQ.SUMP)GO TO 30
20    SUMP=SUM
      WRITE(6,*)' VPULSE DID NOT CONVERGE'
30    VPULSE=SUM
      RETURN
      END
      SUBROUTINE FVPEAK(DMU,T,VM,IER)
      IMPLICIT REAL*8(A-H,O-Z)
      DATA PI/3.1415926535897932D0/
      IF(DMU.LE.0.D0)THEN
      WRITE(6,*)'  VOLTAGE NOT DEFINED'
      RETURN
      ENDIF
      IF(DMU.GT.0.61096148D0)THEN
      W=1.D0/DMU
      F=W*W
      T=(W*(781386480.D0+F*(11881642080.D0+17855925901.D0*F)))/
     1 (781386480.D0+F*(12402566400.D0+24209906625.D0*F))
      ELSE
```

```fortran
      IF(DMU.GT.0.1918343D0)THEN
      T=DLOG(DMU)/(DMU-1.D0)
      ELSE
      T=DLOG(DMU+DMU*DMU)/(DMU-1.D0)
      ENDIF
      ENDIF
      IF(DMU.LT.0.95D0)GO TO 25
      CV=1.D0+DMU
      DO 20 IT=1,25
      IER=IT
      R=1.D0/(DEXP(-T)+1.D0)
      FN=DMU/(DMU+1.D0)
      SUMP=FN
      DO 10 N=1,200
      FN=(N+1)*R*FN/(CV+N)
      SUM=SUMP+FN
      IF(SUM.EQ.SUMP)GO TO 15
10    SUMP=SUM
      WRITE(6,*)' SUM DID NOT CONVERGE'
15    FN=1.D0-SUM
      W=DTANH(0.5D0*T)
      FN=FN/(W+(0.5D0*DMU+0.25D0/W-.75D0*W)*FN)
      T=T+FN
      IF(T.LE.0.D0)T=DABS(T-FN)*0.5D0
      IF(DABS(FN).LE.1.D-10*T)GO TO 50
20    CONTINUE
      IER=-1
      GO TO 45
25    CON=PI*DMU/DSIN(PI*DMU)*DMU
      CV=1.D0-DMU
      DO 40 IT=1,25
      IER=IT
      W=DEXP(-T)
      R=W/(W+1.D0)
      FN=-DMU*(1.D0+W)**(DMU+1.D0)
      SUMP=CON*DEXP(CV*T)*(1.D0+W)**2+FN/CV
      DO 30 N=1,200
```

176

```
        FN=(N-1-DMU)*R*FN/N
        SUM=SUMP+FN/(N+CV)
        IF(SUM.EQ.SUMP)GO TO 35
30      SUMP=SUM
        WRITE(6,*)' SUM DID NOT CONVERGE'
35      FN=1.DO-SUM
        W=DTANH(0.5DO*T)
        FN=FN/(W+(0.5DO*DMU+0.25DO/W-.75DO*W)*FN)
        T=T+FN
        IF(T.LE.0.DO)T=DABS(T-FN)*0.5DO
        IF(DABS(FN).LE.1.D-10*T)GO TO 50
40      CONTINUE
        IER=-1
45      WRITE(6,*)' FVPEAK DID NOT CONVERGE'
50      VM=1.DO/(DCOSH(0.5DO*T)**2*DMU)
        RETURN
        END
```

177